Development of a Microcantilever Based MEMS Device for Biosensor Application

by

Shakib Morshed

A dissertation submitted to the Graduate Faculty of
Auburn University
in partial fulfillment of the
requirements for the Degree of
Doctor of Philosophy

Auburn, Alabama
December 13, 2010

Keywords: microcantilever, microelectromechanical systems (MEMS), biosensor, resonant
frequency, finite element analysis (FEA)

Approved by

Barton C. Prorok, Chair, Associate Professor of Materials Engineering
Dong-Joo Kim, Associate Professor of Materials Engineering
Robert Dean, Assistant Professor of Electrical and Computer Engineering
Pradeep Lall, Professor of Mechanical Engineering
Ruel A. Overfelt, Professor of Materials Engineering

Abstract

In this project a microcantilever based MEMS device for biosensing application had been developed. The geometrical aspects of the cantilever beam structure had been studied for increasing the sensitivity of the sensor devices. Finite Element Analyses of different geometrical shapes were performed to compare the mass sensitivity of different shapes of microcantilever beam structures. Microcantilever beam structures of the promising geometries were fabricated, and their resonant frequencies were measured optically for comparison. Both the FEA results and the optical measurement results agreed that the trends of triangular and the modified shape geometries compared to the regular rectangular shape geometry, in terms of frequency shift performances of those geometries. The triangular shaped geometry showed, approximately, an order of magnitude, and the modified shaped geometry showed more than three times the performance of the regular rectangular shape.

Damping effects on these geometries were investigated by testing them in air at different pressure levels, ranging from the atmospheric pressure of 10^5 Pa to 10^{-2} Pa. The resulting responses of these geometries followed the same trend as the analytical plot for the rectangular shape structure. As the relative resonant frequency of the structure is proportional to the intrinsic resonant frequency, measured at the lowest pressure levels achieved by the AFM system, different shapes showed different amount of responses as a function of pressure. As the intrinsic

resonant frequency of the triangular shape was the highest, its relative resonant frequency was the highest; the modified geometry showed intermediate responses among the three geometries.

MEMS devices based on piezoresistive sensing element were designed and fabricated that included regular rectangular, triangular, and the modified geometrical shapes, based on their performances in terms of the mass sensitivities. Piezoresistive measurements of these MEMS devices were performed to characterize the devices, which matched the optical measurement data of those structures. Thus, this project showed the performances of the microcantilever MEMS devices can be improved in terms of sensitivity, by modifying the geometrical shapes of the regular rectangular shaped geometries. Also, the modified shaped geometry showed lesser effect on their resonant frequency response due to damping effect than the triangular shaped geometry. Thus, by using these geometries, part of the reduction in performances of the microcantilever MEMS devices can be recovered.

Acknowledgements

The author would like to thank his adviser Dr. Barton C. Prorok for his guidance throughout the project; without whose constant guidance and encouragements, this project would not have been completed. Thus, the author is eternally grateful for the accomplishment of this degree, to him. The author would, also, like to extend his gratitude towards the Auburn University Detection & Food Safety (AUDFS) Center for funding the project, which could not have been performed without the necessary funds. Next, the thanks are due to the committee members Dr. Ruel A. Overfelt, Dr. Pradeep Lall, Dr. Robert Dean and Dr. Dong-Joo Kim for providing occasional guidance, and equipment necessary for the completion of this project.

Special thanks are due to the Microelectronics Fabrication Laboratory of the Alabama Microelectronics Science & Technology Center (AMSTC), especially Charles Ellis for his constant support and advice. Thanks are also due to William Baugh, Kieth Warren, Drew Sellers, Roger Lugo, Joe Haggerty and Mike Palmer for their help at different phases of the project. Thanks are, also, due to LC Mathison, Levar Odum, Roy Howard, Dave Lindahl and Steve Moore for their technical assistances throughout this project. Thanks are due to Shirley Liles and Alison Mitchell for their administrative helps. Thanks are due to numerous colleagues and group members; without their helps this project would not have been completed. Among them Bo Zhou, Cai Liang, Nikhil Mehta, Madhumida Ramaswamy, Nicole Odum, Dong Liu, Kevin

iv

Table of Contents

List of Figures

List of Tables

List of Charts

CHAPTER 1

INTRODUCTION

In recent years, Microcantilever based sensors have been applied to detect different physical quantities, such as acceleration of automobiles to deploy airbags, and different chemical [1-8] and biological species [8-17] present in different environments. Sensors consist of two elements: sensing and transduction elements. The sensing element measures the measurand, which can be a physical quantity, property or a certain condition, from the input signal that can be magnetic, chemical, electromagnetic, mechanical, thermal etc. Microcantilever based sensors use two types of detection schemes, one of them involves deflection of the cantilever beam structure due to the mass loading on the beam in static condition, while the other one involves the change in the resonant frequency of the cantilever beam structure due to the mass loading on the beam in dynamic condition. In this study, the second kind of detection scheme had been employed, which is illustrated in figure 1. In case of the frequency based detection scheme, the sensing element of the microcantilever based sensor is the cantilever beam structure with specific natural frequencies. These sensors work on the principle of resonant frequency. That is, resonance occurs when an imposed frequency of vibration matches the natural frequency of vibration of the structure. This translates into the fact that the deflection of the beam structure tends to become infinite, compared to the normal conditions. The transduction element

transduces the sensed signal into an output signal, preferably electrical, which is a quantity depending on the applied measurand. In this experimental study, piezoresistive element was used as the transduction element. Piezoresistive materials change their resistivity depending on the applied strain. As the cantilever beam structure vibrates, it bends up and down or sideways. This translates into the straining of the piezoresistive sensing element, which is integrated into the beam structure. This result into change in the resistivity of the material; thus, changes the total resistance (ΔR) of the piezoresistive element. This change in resistance can be detected through the change in the measured voltage drop (ΔV) across these elements. To amplify this output, usually, a Wheatstone bridge configuration is used.

Biosensors usually use acoustic wave based sensing devices for detection. They use elastic waves at frequencies well above the human audible range propagating through the sensing structures. Microcantilever based sensor devices fall into this category. Datskos et al. [18], Oden [19] and Stern et al. [20] have compiled and compared performances of acoustic wave based sensors. Table 1 lists the mass sensitivity, which can be expressed by the equation 1, and the minimum detectable surface mass density for this type of devices.

$$S^m = \frac{1}{f} \cdot \frac{\Delta f}{\Delta m_s^{\min}} \qquad (1)$$

Here, f: resonant frequency,

Δf: resonant frequency shift

and, $\Delta m_s^{\min}$: Minimum detectable surface mass density.
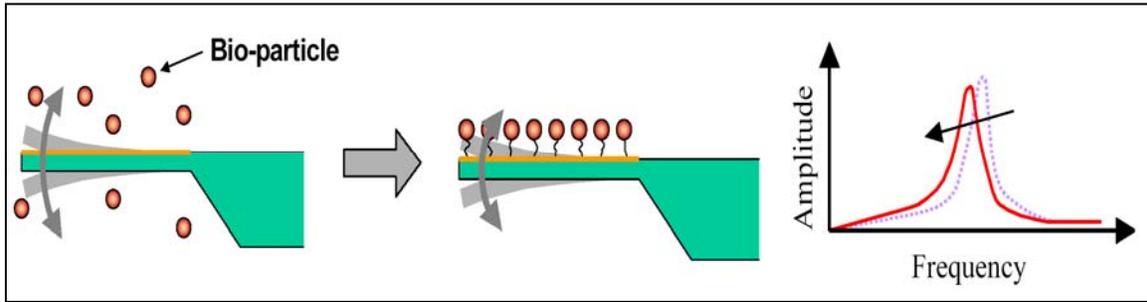
Figure 1: Resonant frequency based detection scheme of microcantilever based biosensors.

Table 1: Comparison of Acoustic Wave based sensors

Sensor type	Resonant frequency, f (MHz)	Mass sensitivity, S^m (cm^2/gm)	Δm_s^{min}(ng/cm^2)
Microcantilever	0.005-5	991-1363	0.069-13.8
Flexural Plate Wave (FPW)	2-7	951	0.4
Surface Acoustic Wave (SAW)	30-300	151	1.2
Acoustic Plate Mode (APM)	25-200	65	1.0
Quartz Crystal Microbalance (QCM)	5	14	10

It shows that, by employing microcantilever based sensing device, the smallest amount of mass can be detected. In recent years, researchers at the Cornell University have demonstrated attogram ($x10^{-18}$ gm) level mass sensitivity [21]. However, they have employed AFM (atomic force microscopy) system for detection, which employs optical detection scheme. Thus, the detection mechanism is bulky and expensive, and cannot be employed in liquid mediums.

In order to apply a sensor device as a biosensor, it has to be compatible with the biological agent that needs to be detected. Also, it has to be of low cost and easily operable, and has to have high specificity and selectivity to eliminate false signals. To achieve the biocompatibility of the sensor, the sensing surface is coated with gold pads, which can be functionalized to capture a specific bacteria or other biological agent that needs to be detected. As the biosensors are required to be operated at remote and numerous locations, such as in the food chains of humans and animals alike, it needs to be inexpensive and easily operable. On-chip MEMS devices allow us to achieve this goal. As the MEMS devices are fabricated using the microelectronic fabrication processes, it enables us to fabricate the devices in batches, which lowers the fabrication cost. Conventional microcantilever based sensors are operated using optical based sensing scheme to detect the shift in the resonant frequency due to the attachment of mass on the sensor surface, which is costly and not easily operable. On the other hand, MEMS devices give electrical output signals that can be easily operated and inexpensively processed; thus, driving downs the cost of the operation and minimizing the expertise of the operator. For biosensor applications, the sensor needs to operate in liquid media, as most pathogens are present in liquid based solutions. Optical sensing schemes are not suitable for liquid media. Thus, the MEMS devices with proper passivation layers can be effectively used in liquid based media. Figure 2 shows both of these sensing schemes. As the resonant frequency

of a structure depends on the mass and the stiffness of the structure, the sensitivity of the structure depends on the geometry of the microcantilever structures. In recent years, different researchers are investigating effects of sizes and shapes of the microcantilevers to increase the sensitivity of the sensors. In this study, the geometrical aspects of the microcantilever structures were investigated to increase the sensitivity. To perform that task, finite element analyses (FEA) of different geometrical shapes were performed using ANSYS software to calculate the frequency shift for a small mass attached on the tip of the geometries, and then compared to the basic rectangular shapes. Some of the promising geometrical shapes of microcantilever structures, found from the numerical analysis, had been designed and fabricated for MEMS based sensors. In this experimental study, these geometrical shapes were studied, along with the basic rectangular shaped cantilever structures, and performance of those experimental results were compared with the numerical ones. For initial evaluation, microcantilever beam structures were made of in the range of 100 μm length of different geometrical shapes along with regular rectangular shape. Also, the damping effects on these geometries were studied. The other aspect of this study was to increase the mass sensitivity by reducing the length of the piezoresistive microcantilevers. So far, researchers have reported piezoresistive microcantilever sensors in the dimensions of 100s of μm length. In this project, piezoresistive microcantilevers of 50, 150 and 250 μm lengths were fabricated; thus, increasing the mass sensitivity of the devices.
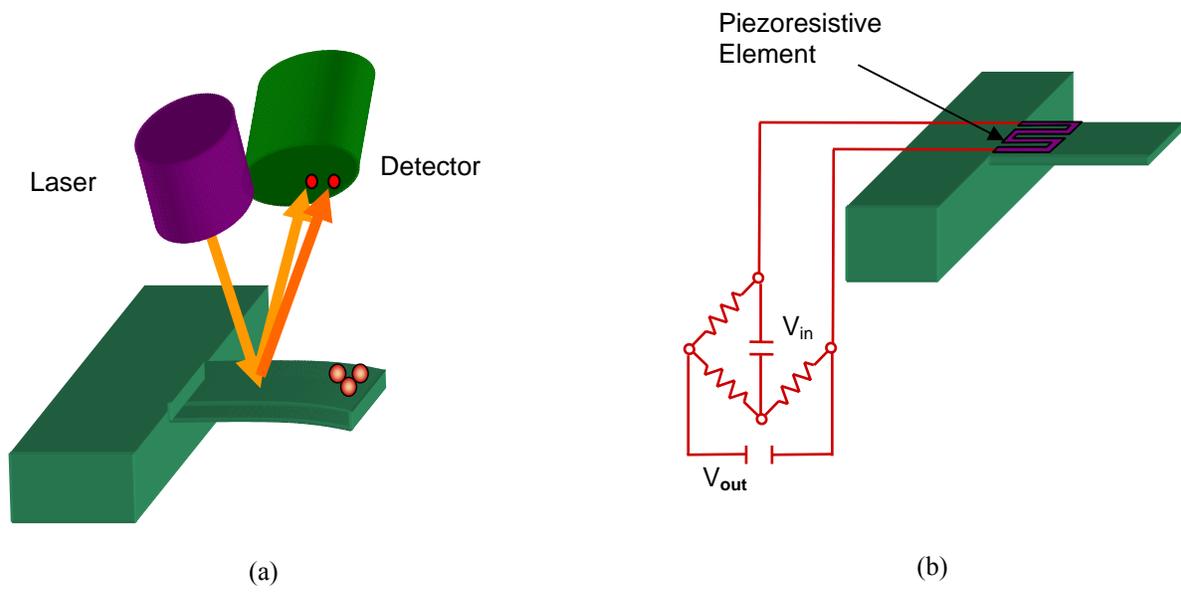
Figure 2: (a) conventional optical based frequency sensing scheme, and (b) MEMS based sensor.

CHAPTER 2

THEORETICAL BACKGROUND

Microcantilever based sensors are usually operated on the basis of shift in the resonant frequency of the structure due to the attachment of mass to the target element on the beam. The resonant frequency of undamped cantilever beam structure of a uniform rectangular cross section can be obtained from the solution of an undamped simple harmonic oscillator [22]. For a cantilever beam with a uniform rectangular cross section, and a negligible thickness compared to the other parameters, the natural frequency of vibration can be approximated from the following equation:

$$f_i = \frac{\lambda_i^2}{2\pi} \cdot \frac{t}{l^2} \sqrt{\frac{E}{12d}}$$

(2)

where, t: thickness of the beam,

     l: length of the beam,

     d: density of the material

     E: elastic modulus,

and, λ_i: i-th root of the frequency equation; $\cos \lambda \cosh \lambda + 1 = 0$, which depends on the boundary conditions of the cantilever beam structure.

These roots represent the consecutive mode shapes of the natural frequency of vibrations of the beam structure. The first few roots for the cantilever beam structure are [23]: $\lambda_1 = 1.87510407$, $\lambda_2 = 4.69409113$, $\lambda_3 = 7.85475744$, $\lambda_4 = 10.99554073$, $\lambda_5 = 14.92256510$ etc. Now the following Figures 3 through 7, show the first five mode shapes that are numerically calculated for a simple cantilever beam, using the ANSYS software for finite element analysis (FEA). Here, it can be seen that the base of the cantilever, which is fixed on the extreme left side on each figure, is uniformly stressed only in the first mode of natural frequency of vibration. As piezoresistive material had been used to detect the change in frequency through the voltage measurements, the transduction element of the sensor should be uniformly stressed during the measurements for reliable signal output. So, in this project the sensor devices were designed for the application based on the 1st mode shape of the natural frequency of vibration.

Now, by using the equation (2) for the 1st mode shape of vibration, the natural frequency of a regular shaped cantilever beam can be calculated as a function of both thickness and length. Figure 8 shows a three dimensional plot of natural frequency of vibration for the 1st mode shape. From this plot, it is clear that the natural frequency of vibration of cantilever beam structure increases significantly at around 50 μm of lengths. Although, the natural frequency increases even further more for lengths below 50 μm, the most important limitation for any MEMS device is imposed by the fabrication facilities that are available. In this case, it is the Microelectronics fabrication Lab in Auburn University at the Alabama Microelectronics Science and Technology Center (AMSTC), where these MEMS devices were fabricated. In addition to this, as the dimensions get smaller, the cost of fabricating them becomes higher.
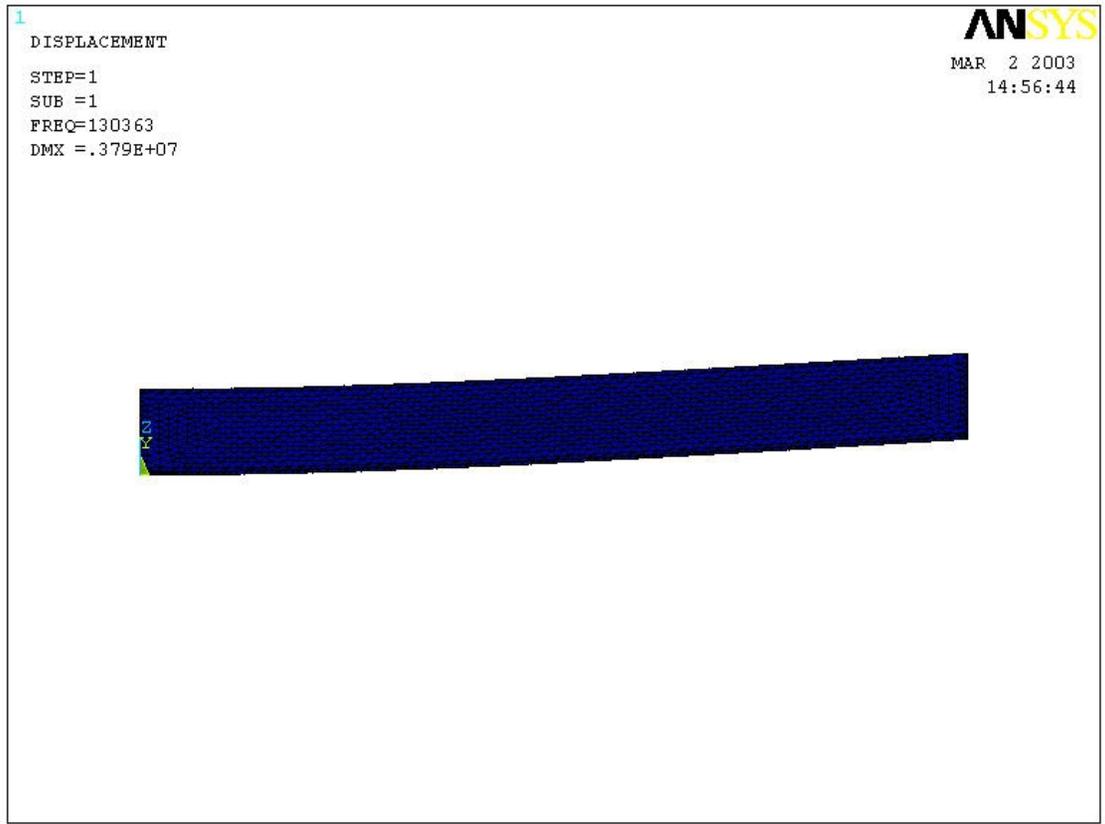
Figure 3: 1st mode shape of natural frequency of vibration of a cantilever beam of

l = 50μm, w = 10μm & t = 200nm.
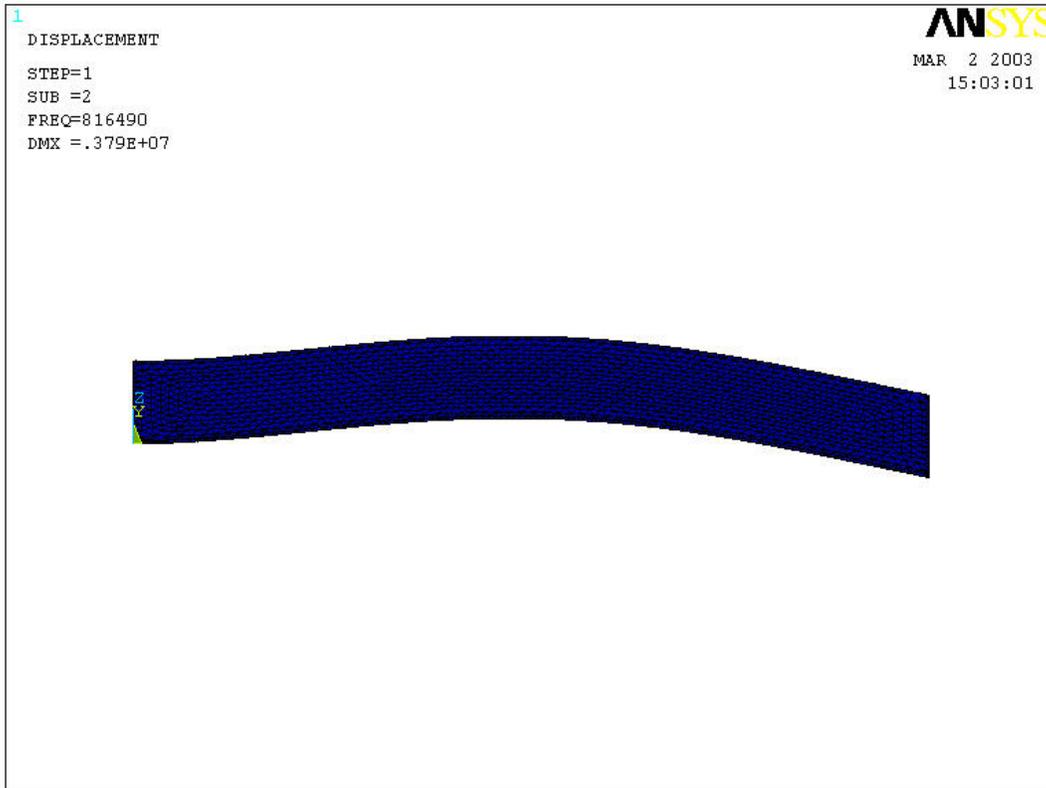
Figure 4: 2nd mode shape of natural frequency of vibration of a cantilever beam of

l = 50μm, w = 10μm & t = 200nm.
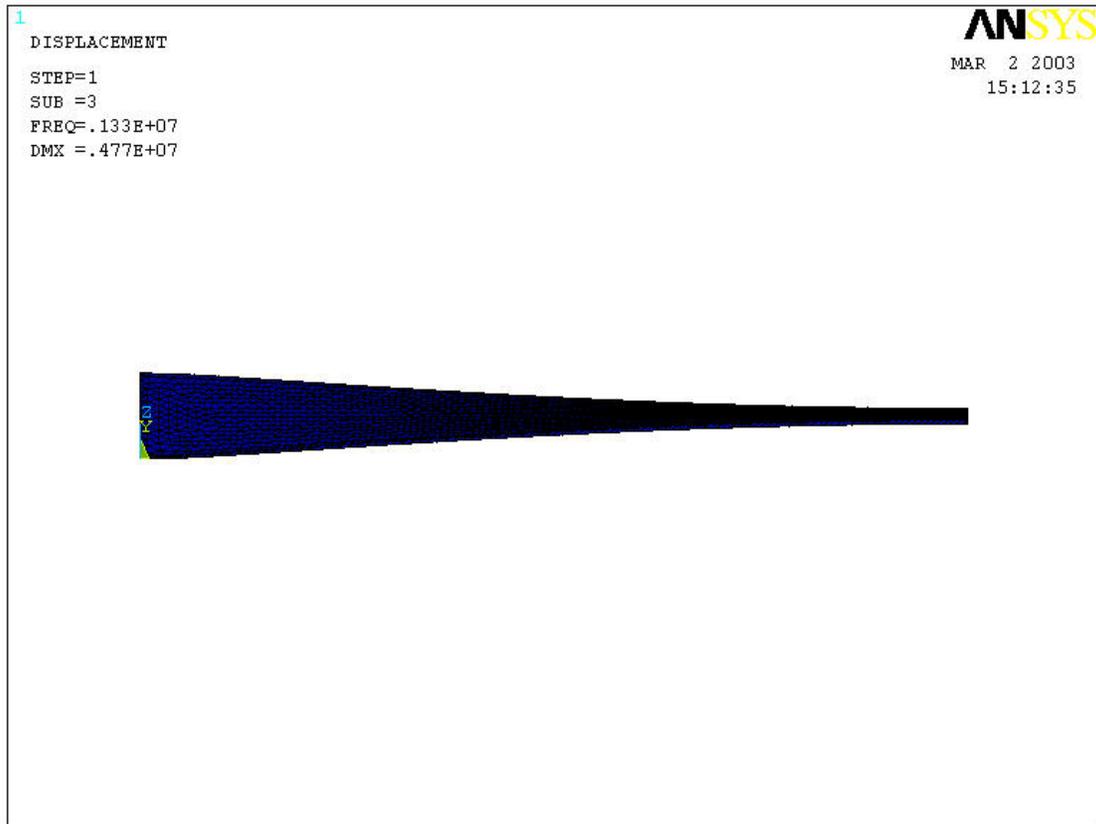
Figure 5: 3rd mode shape of natural frequency of vibration of a cantilever beam of

l = 50μm, w = 10μm & t = 200nm.
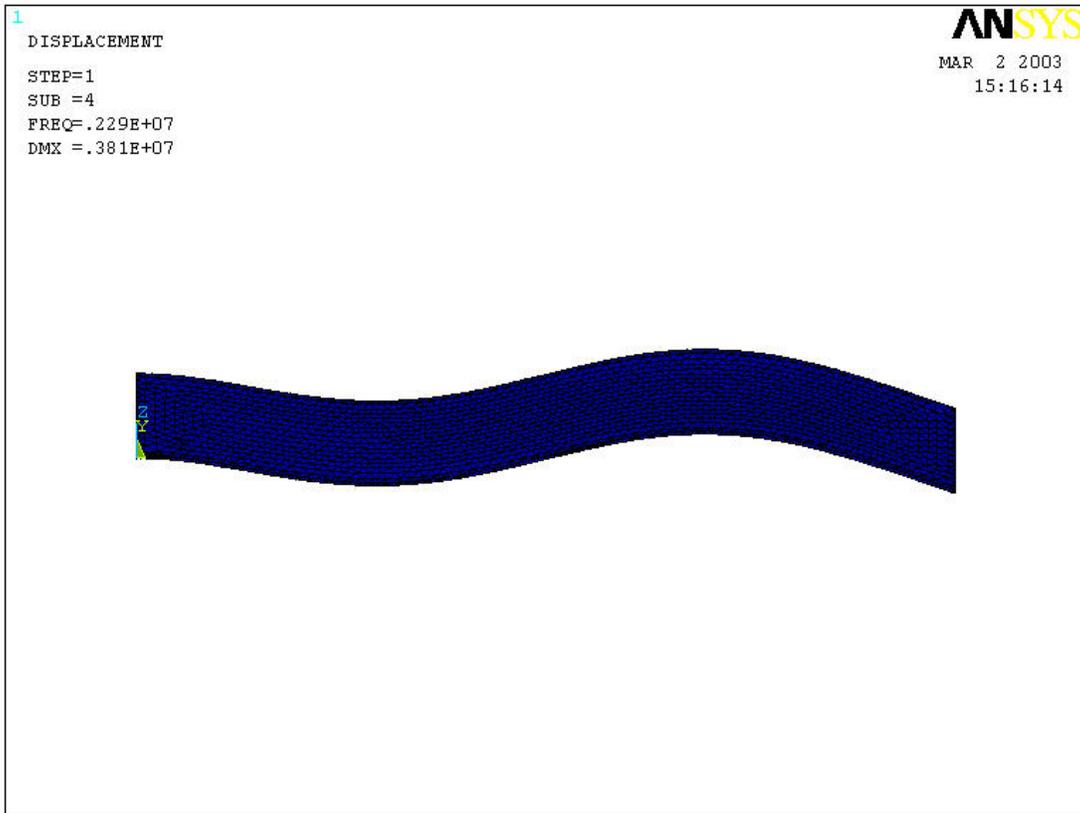
Figure 6: 4th mode shape of natural frequency of vibration of a cantilever beam of

l = 50μm, w = 10μm & t = 200nm.
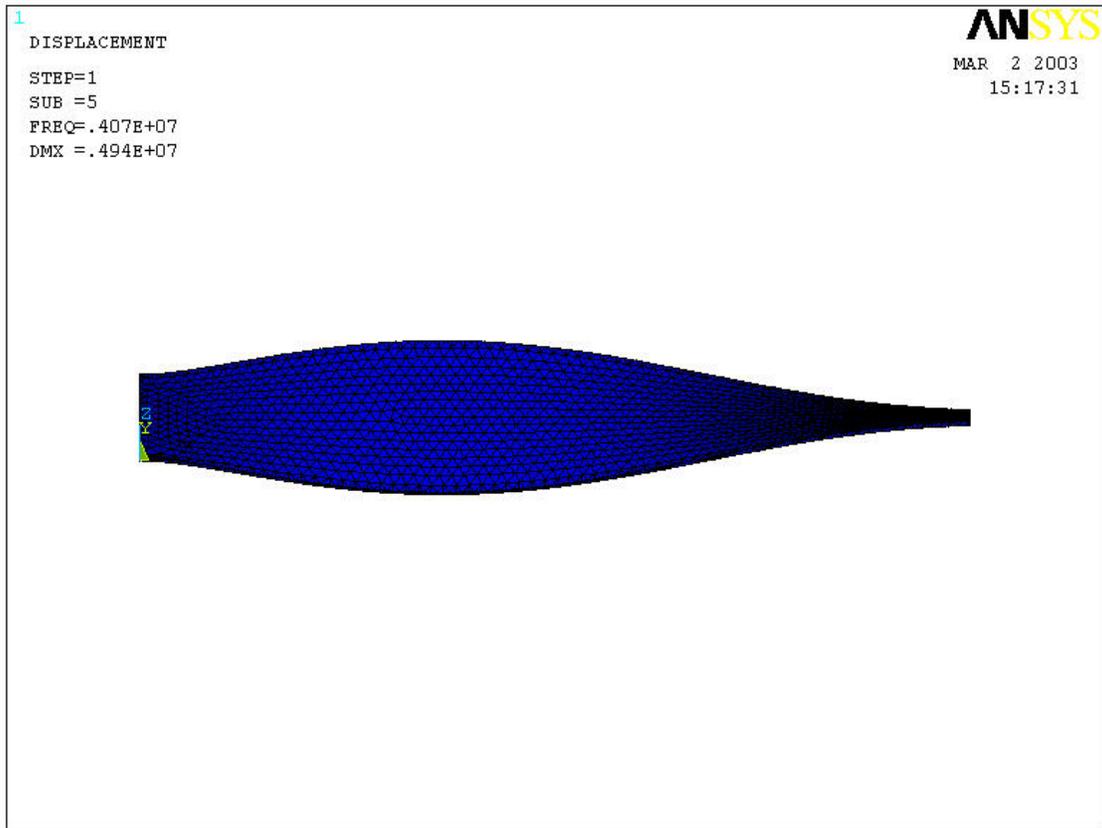
Figure 7: 5th mode shape of natural frequency of vibration of a cantilever beam of

l = 50μm, w = 10μm & t = 200nm
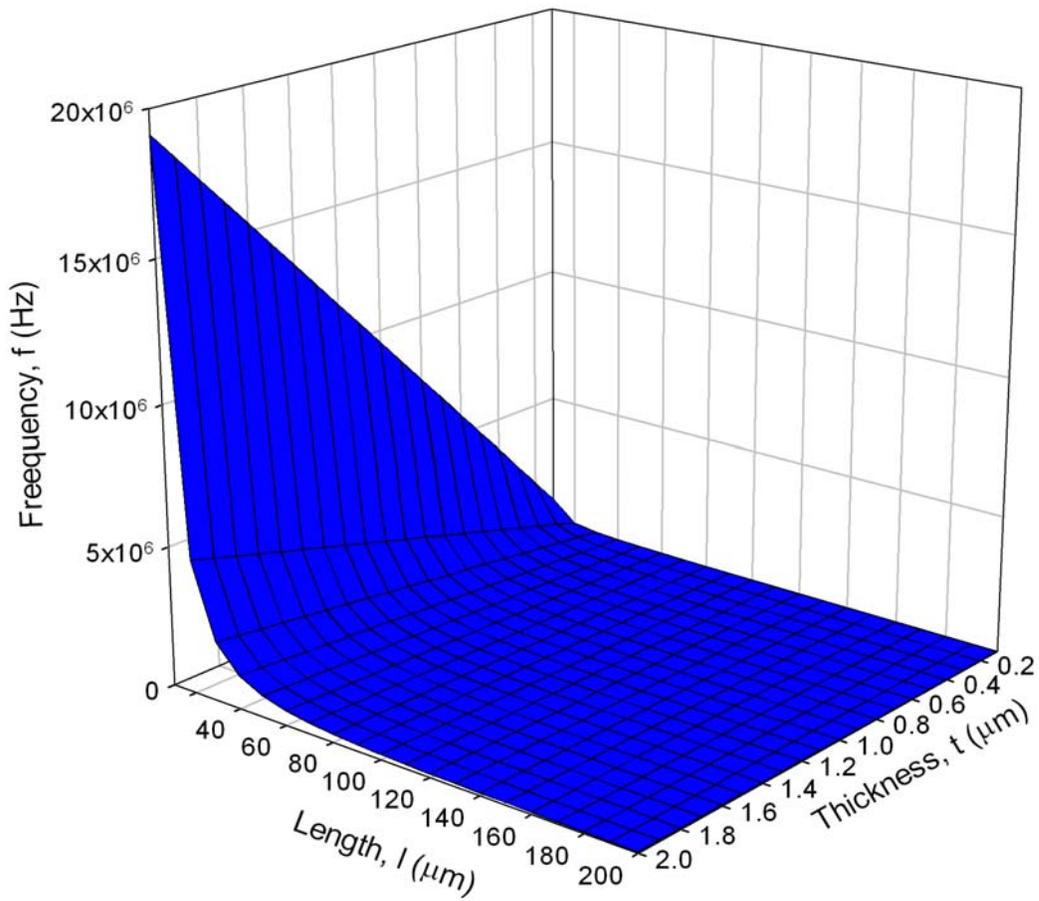
Figure 8: 3D plot of natural frequency of vibration (1st mode shape) of microcantilever beam as a function of length & thickness.

Although equation (2) holds quite well for a narrow cantilever beam structure for all the practical purposes, it neglects to take account the Poisson's effect for wider beam structures, which were evident from the finite element analysis results. As the width to length ratio of the beam structure increases, they start to behave more and more like a plate. Thus, Yahiaoui et al. [24] have introduced a correction factor for the uniaxial elastic modulus to take account for the Poisson's effect. They have modified the equation (2), by using the effective elastic modulus Y_{eff}, instead of the uniaxial elastic modulus E, which can be related by the following expression:

$$Y_{eff} = E \left[1 + \alpha \left(\frac{1}{1 - v^2} - 1 \right) \right]$$

(3)

where, v: Poisson's ratio,

and α: correction factor, depending upon the width to length ratio of the beam structure. This correction factor can be calculated numerically by using finite element analysis for different width to length ratio of cantilever beam structures. Thus, the equation (2) takes the following form [24]:

$$f_i = \frac{\lambda_i^2}{2\pi} \cdot \frac{t}{l^2} \sqrt{\frac{Y_{eff}}{12d}}$$

(4)

The equation (2) can be, alternatively, expressed as follows [25, 26]:

$$f_i = \frac{1}{2\pi} \sqrt{\frac{k}{m_i^{eq}}}$$

(5)

where, k: flexural stiffness of the cantilever beam, which is the proportionality constant between

the applied load and the resulting deflection,

and, m_i^{eq} : the equivalent mass acting on the beam structure for the i-th mode shape.

In the equation (5), the stiffness of the beam remains unchanged due to the attachment of

the analytes on the surface of the cantilever beam while the equivalent mass changes. Now, the

change in resonant frequency of the cantilever beam can be approximated from the following

expression [25]:

$$\Delta f_i \approx \frac{f_i}{2} \cdot \frac{\Delta k}{k} - \frac{f_i}{2} \cdot \frac{\Delta m_i^{eq}}{m_i^{eq}} \approx -\frac{f_i}{2} \cdot \frac{\Delta m_i^{eq}}{m_i^{eq}} \tag{6}$$

Thus, from the equation (4) it can be observed that the sensitivity of the microcantilever

based sensor device is proportional to the natural frequency of the cantilever beam structure, and

inversely proportional to the effective mass acting on the structure. Also, from the equation (5),

it is clear that the natural frequency of vibration is inversely proportional to the effective mass of

the structure itself. Thus, in this experimental study, different geometrical shapes of the

cantilever beam structures were investigated to increase the sensitivity through increasing the

natural frequency of vibrations of the structures, while keeping the length of the cantilever

structure at the range of 50-150 μm due to the limitations that were discussed earlier.

Now, let us discuss the piezoresistive phenomenon, through which this sensor devices

transduce the input measurand signal into the electrical output signal. Piezoresistive material

changes its resistivity when it experiences stress, according to the following expression [27]:

$$\Delta \rho = \pi \cdot \sigma \cdot \rho \tag{7}$$

where, ρ: resistivity of the material,

σ: applied stress,

and, π: the piezoresistive coefficient that depends upon the doping type, n-type or p-type, and the doping level of the single crystal silicon or polycrystalline silicon material. In this case, polysilicon were used for transduction. Also, it depends on the crystallographic orientation of the silicon and in case of polysilicon it takes up an average value of the directional coefficents. The total resistance change of the piezoresistive element can be expressed by the following expression for the gage factor [27]:

$$G = \frac{\Delta R/R}{\varepsilon} = 1 + 2\upsilon + (\pi_l \varepsilon_l + \pi_t \varepsilon_t) \cdot \frac{E}{\varepsilon} \qquad (8)$$

where, ν: the Poisson's ratio,

ε: strain applied on the element,

R: resistance of the piezoresistor,

ΔR: change in resistance,

and, the subscript l and t: denotes the lateral and the transverse directions respectively. In case of operating in the 1st mode shape, ε_t becomes negligible. Thus, the piezoresistive sensing elements in these sensors operate similarly as a strain gage. Although, single crystal silicon of certain orientation gives higher gage factor [27] and better performances against certain noises present in the system, the temperature effect on the resistivity of the piezoresistive material is greater in single crystal silicon than that of the polycrystalline silicon. The piezoresistive elements that had been used for these sensors are of high concentration ($\sim 10^{19}$-10^{20}/cm^3) of phosphorous doped polysilicon thin film of approximately 100nm thickness, and deposited in the Low Pressure

Chemical Vapor Deposition (LPCVD) system. After depositing the polysilicon film, it was doped with phosphorous by drive-in technique performed at 1000°C. These processes will be discussed further in details in the later chapter discussing the microfabrication process.

As the changes in resistance of the piezoresistive element, due to small strain, and to compensate for the temperature effect on the resistivity of the piezoresistances, the strain gages are usually operated in a Wheatstone bridge configuration as shown in figure 9. Here, the output voltage across the bridge can be calculated using the following expression [27]:

$$V_{out} = \left[\frac{R_4}{R_2 + R_4} - \frac{R_3}{R_1 + R_3} \right] \cdot V_{in} \qquad (9)$$

As in the most cases, including this one, the resistances $R_1 = R_2 = R_3 = R_4 = R$. In the above expression and for a small change in resistance, $\Delta R << R$; it reduces to:

$$V_{out} \approx \frac{1}{4} \cdot \frac{\Delta R}{R} \cdot V_{in} \qquad (10)$$

Here, the change in the resistance of the piezoresistive poly silicon strain gage of length l_{gage} on a microcantilever beam with length l, width w and thickness t, which is deflected by a static force of F, can be expressed as follows [27]:

$$\frac{\Delta R}{R} = \frac{6\pi \left(l - {l_{gage}}/{2} \right) \cdot F}{wt^2} \qquad (11)$$

18
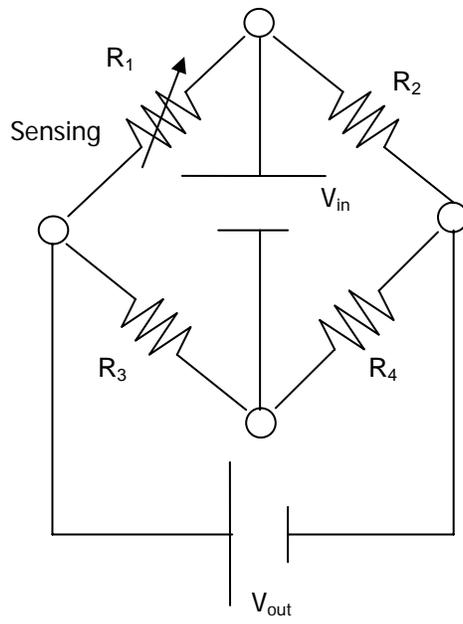
Figure 9: Wheatstone bridge configuration.

Figure 10 shows a representative 3D plot of equation (11). From figures 8 and 10, it can be seen that the frequency of the beam increases with decrease in the length, while the fractional change in resistance; thus, the gage factor for the piezoresistor decreases. Also, the frequency of the beam increases with the thickness, while the fractional change in resistance decreases. These conflicting characteristics of the piezoresistor and the cantilever beam show a trade off between higher cantilever beam sensitivity and higher piezoresistive sensitivity. As the cantilever beam becomes shorter and thicker, the frequency of the beam increases and it becomes stiffer; thus, reducing the detectable change in resistance of the piezoresistive element. Therefore, a balance has to be established between theses two phenomena. In this project, the cantilever beam structure dimensions were chosen to be of 50-150 μm length and thickness of approximately 1 μm. These parameters are limited by the fabrication processes that are available in the facilities at Auburn University.

The main problem with the piezoresistive sensing scheme arises from the thermal drift of the material, which introduces Johnson noise in the frequency measurements. To take account for this phenomenon, reference cantilever beam had been introduced in the novel design of this experimental study. These reference beams would be operating in the same environment as the sensing cantilevers. This Johnson noise is the fundamental limitation of any piezoresistor application set by the thermal energy of the system. This noise is independent of the frequency and depends upon the temperature and the resistance of the piezoresistors, which is a function of the geometry of the piezoresistive polysilicon element and its doping concentration [28-29]. The voltage noise power density (Volt^2/Hz) can be calculated for the application range of frequency, Δf by using the following expression:

$$S_J = 4k_B \cdot T \cdot R \cdot \Delta f \tag{12}$$
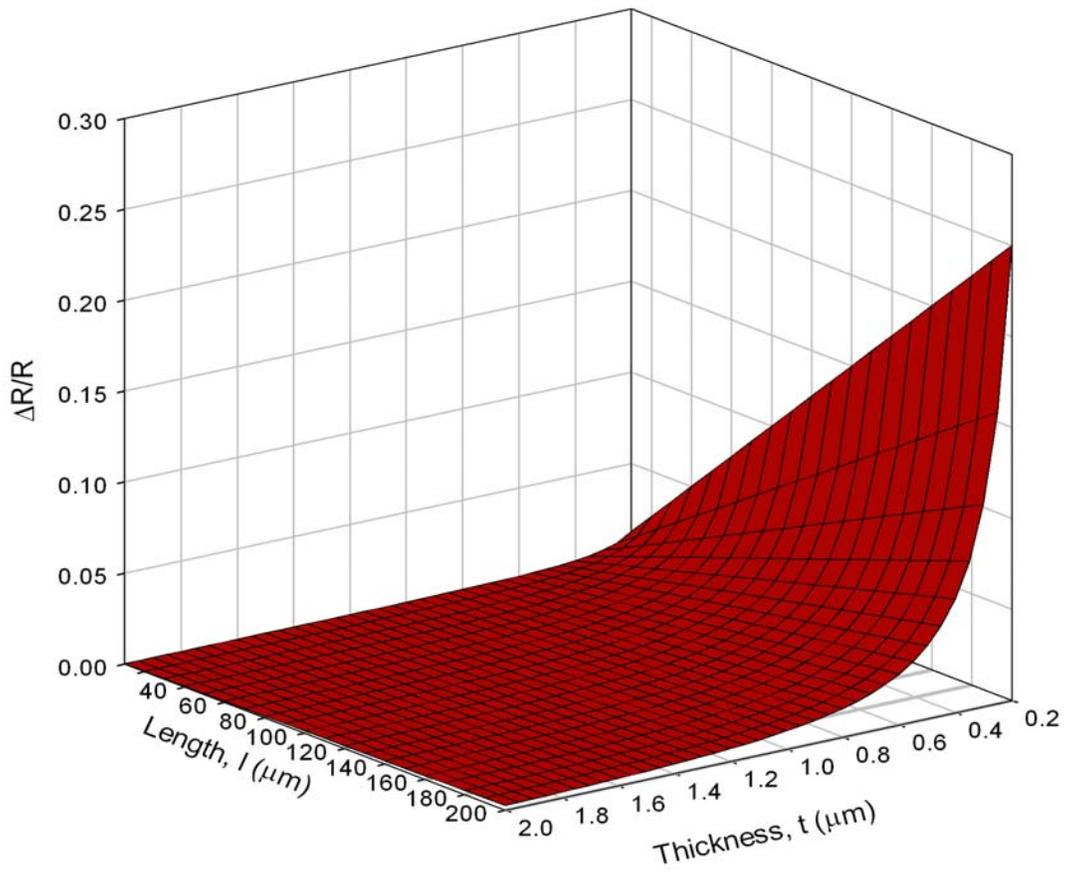
Figure 10: 3D plot of fractional change in piezoresistance on microcantilever beam as a function of length & thickness.

where, k_B: Boltzman's constant,

and, T: temperature of the piezoresistor (K).

As the reference cantilever is introduced with the sensing one, and both of them are operated in the same environment (i.e. temperature and external noise), it will facilitate to monitor and compare their responses during their applications. Figure 7 shows schematic arrangement of a device with both the sensing and the reference cantilever beam structures integrated in a Wheatstone bridge configuration. As the cantilever beams are right across each other in the figure, there is a possibility of harmonic waves, generated due to their vibration, which may interfere with each others response during their operations. In this experimental study, to investigate this phenomenon, reference cantilevers are being fabricated right across the sensing cantilevers, at an offset distance from each other. In addition to that, the piezoresistors integrated in the reference cantilever beam, can be either included as one of the resistances of the Wheatstone bridge configuration that consist of the piezoresistances integrated in the sensor cantilever beam, or can be fabricated as a part of another Wheatstone bridge configuration separate from the sensing side. In this project both of these configurations are being investigated for better performances. One plausible advantage of the 1st type is that depending upon their arrangements, the sensitivity of the device can be increased; while the advantage of the 2nd type is that their responses can be monitored at the same time, making it possible to read the frequency shift directly from their responses, provided that both of their basic frequencies are the same, eliminating the need for the base line frequency establishment. To make sure both the sensing and the reference side cantilevers have the same basic frequencies, a mass balancing had to be performed for their designs. In the sensing side of the device, the sensing pads are required to be exposed to capture the biological analytes that need to be detected, while in the reference

side of the device the metal pads need to be covered by the passivation layer, so that none of the analytes get captured on that side. Therefore, to balance the extra amount of passivation layer material on the reference side, a mass balance needs to be performed, and the same amount of mass from the metal layer was removed from the middle of the designed pads on the tip of the cantilever beam structures.
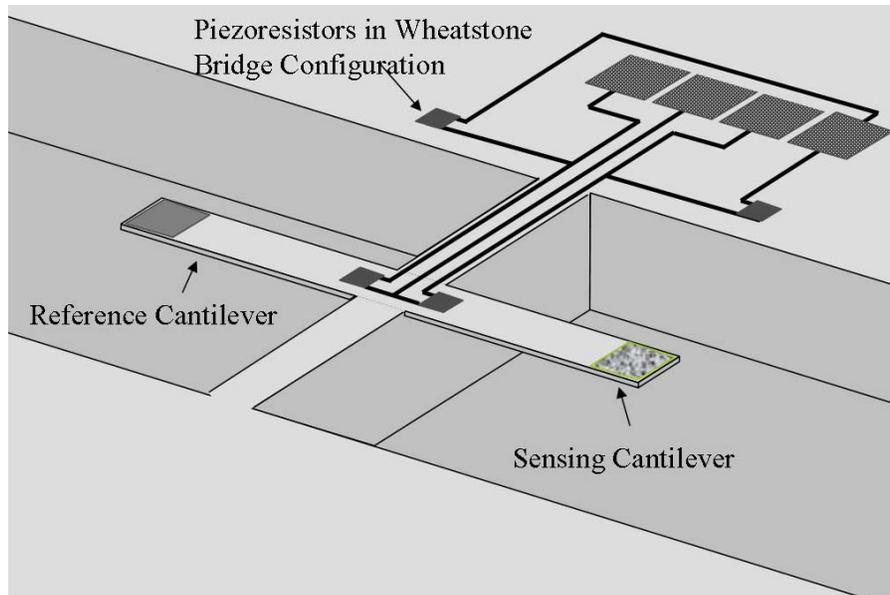
Figure 11: Schematic arrangement showing the sensing & the reference cantilevers of the MEMS device.

CHAPTER 3

NUMERICAL ANALYSIS OF GEOMETRIES

As previously discussed, the different geometrical configurations of microcantilever beam structures are being analyzed to increase the sensitivity of the microcantilever based MEMS devices. ANSYS software was used to perform finite element analysis (FEA) on different shapes of cantilever beam structures to calculate the natural frequency of vibrations. Any vibrating structure can be assumed as a system consisting of components that possess distributed energy storage and dissipative characteristics. In a vibrating structure, such as a cantilever beam, the inertial property or the effective mass of the beam, stiffness of the beam and the damping parameters vary with time and with respect to their spatial locations. These parameters, spatial coordinates and time, can be represented by partial differential equations, which can be solved to represent their vibration responses. In finite element method a vibrating system can be approximated by a set of properly interconnected lumped masses using discrete linear spring and linear viscous damping elements, which enable the system to be represented by ordinary differential equations. These systems can be solved by using mode-frequency analysis or modal analysis [30], which is based on the assumption that these structural models have preferred frequencies or natural frequencies of vibration and geometric configurations or natural mode shapes. This modal analysis provides an important tool to design the cantilever beam structures for the MEMS devices. The resonant frequency of the designed structures, their mode

shapes and their response to the addition of mass, which needs to be detected, can be calculated by performing modal analysis of those structures. As it was described before, to get a uniform and reliable response from the piezoresistive transducers, only the first mode shape of vibration of the beam structures are of concern for this project.

In modal analysis for a linear system, the free vibration of a mechanical structure can be represented by the following matrix equation [31]:

$$\left[[K] - \omega_i^2 [M]\right]\{\phi\}_i = 0 \tag{13}$$

This represents an eigenvalue problem that can be solved for n number of circular natural frequency of vibration ω from ω_i^2 and n number of corresponding eigenvectors $\{\phi\}_i$. These circular natural frequencies are converted into the natural frequency of vibration for the outputs, by using the following expression:

$$f_i = \frac{\omega_i}{2\pi} \tag{14}$$

To compare sensitivity of different geometrical shapes of cantilever beam structures, modal analysis on a number of different shapes of cantilever beams were performed with the same thickness and length. Also, to compare the frequency shift due to the same amount of mass attached at the tip of the cantilever beams, modal analysis of those cantilever beam structures with an addition of a mass of sub picogram level were performed. In this study, the length of the cantilever beams was chosen to be of 50μ and the thickness of 0.5μm, and modal analyses were

performed to calculate the natural frequencies of the beam structures. To compare the frequency shift, a small element of 1μm X 1μm X 0.1μm dimensions was chosen and attached on the top of the cantilever beam structures near the tip, and their modal analyses were performed to calculate the frequency of the changed structural masses. Then, the new frequency was subtracted from the previous one, which provided the frequency shift for the corresponding geometrical shapes. The material properties, chosen for the attached mass are the same as that of the main cantilever beam structure, which contain the material properties of silicon rich-silicon nitride deposited in the LPCVD system. The elastic modulus of the LPCVD nitride was conservatively chosen to be 100 GPa, the density of the material was assumed 2850 kg/m³, and the Poisson's ratio of 0.24 [32]. To calculate the frequency shift due to the attachment of the mass, the small mass element was attached 5μm from the tip of the cantilever to simulate the realistic events for these sensor devices, as the sensing pads on these devices are not at the very tip of the cantilever beam structures due to the limitations imposed by the fabrication processes. Figure 12 shows the arrangement of the small mass attachment on a rectangular shaped cantilever. The resulting frequencies of the structures and their corresponding frequency shifts are tabulated in the Table A.1, for comparison.

In Table A.1, the first three geometries included are for simple rectangular shaped microcantilevers with different widths. Although, in the equation (2), which is only an approximation by itself, the width parameter is not represented, the simulation results show a little variations from the theoretical values calculated from the equation. The FEA results for these widths are within 0.85% for the 10 μm to 1.82% for the 30 μm widths. This small discrepancy between the theoretical and numerical results arose from the fact that the analytical solution does not take account for the Poisson's effect. Even though this equation approximates

27
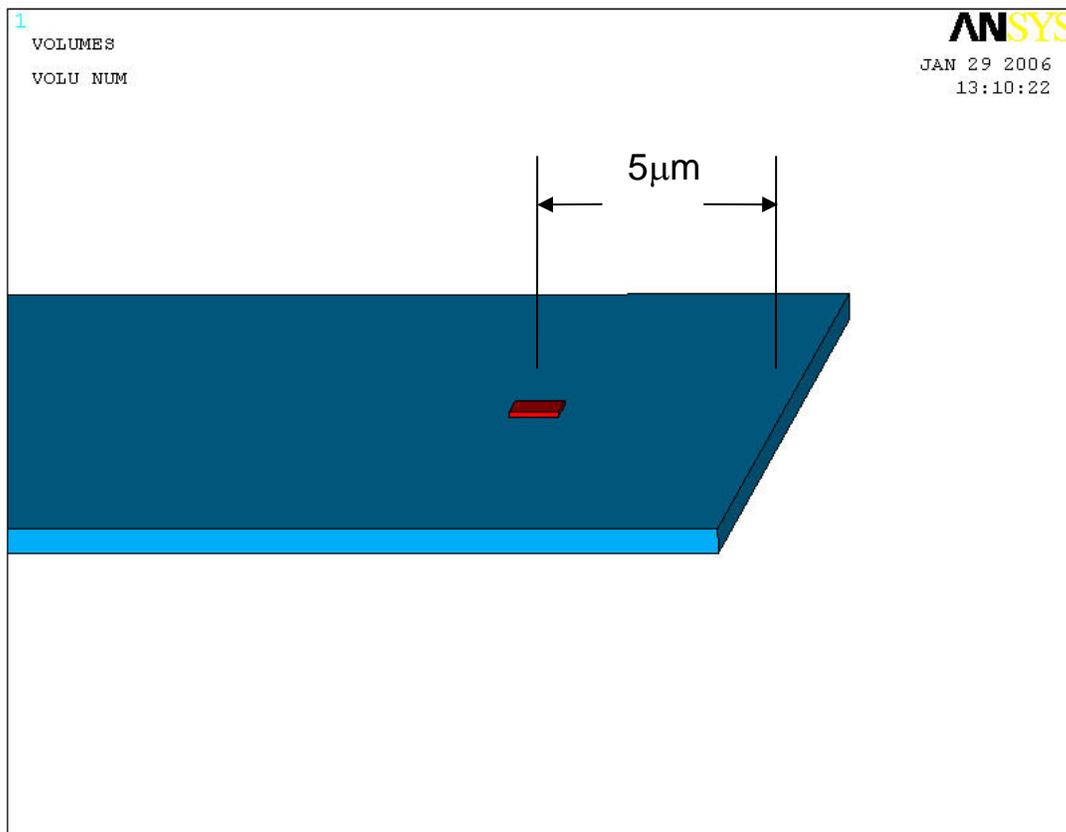
Figure 12: Arrangement showing the small mass attachment in the FEA simulations.

quite well for all practical purposes, finite element results for different width to length ratios were investigated. The FEA results of the natural frequency of vibrations and their corresponding frequency shifts for the attached small mass, as described earlier, are tabulated in the following Table 2. The corresponding correction factors were calculated by combining equations (3) and (4), and tabulated in the Table 2 with their corresponding width to length ratios.

Figure 13 shows the plot of the correction factor as a function of width to length ratio. The curve was fitted by using the following expression:

$$\alpha = a\left(1 - \exp^{-b\left[\frac{w}{l}\right]}\right) \tag{15}$$

where, the curve fitting parameters a = 0.8662 and b = 1.9547 with the standard error estimate of 0.005. Figure 14 shows the plot of the frequency shift for the attached mass of 0.285 picogram as a function of the width to length ratio. The curve was fitted by the 1st order inverse polynomial as follows:

$$\left|\Delta f\right| = a + \frac{b}{\left[\frac{w}{l}\right]} \tag{16}$$

where, the curve fitting parameters a = 6.2806 and b = 22.4322 with the standard error estimate of 5.5477.

Table 2: Correction factors for different width to length ratios

Width, w (μm)	Width to length ratio, w/l	Frequency, f (Hz)	Frequency shift, Δf (Hz)	Correction factor, α
1	0.02	191,517	1,127	0.0242
5	0.1	192,248	234	0.1495
10	0.2	192,997	125	0.2785
20	0.4	194,124	53	0.4733
30	0.6	194,858	46	0.6009
40	0.8	195,336	32	0.6842
50	1.0	195,666	29	0.7418
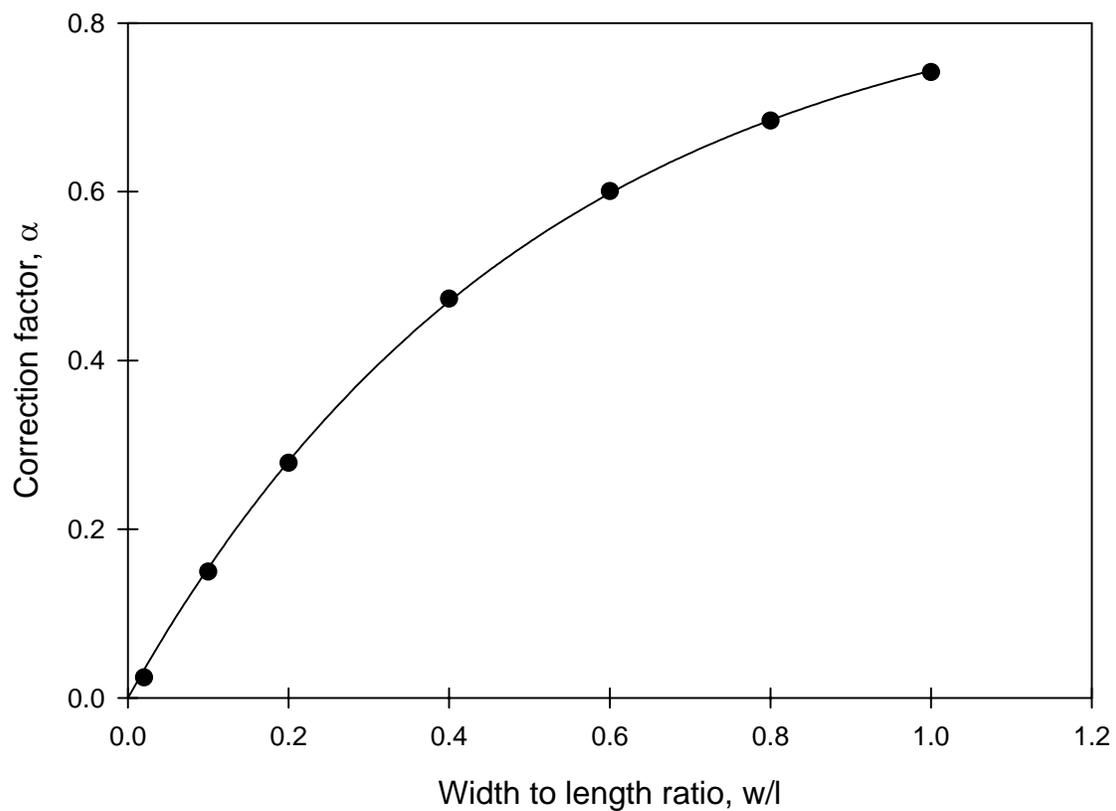
Figure 13: Plot showing numerically calculated correction factor as a function of the width to

length ratio of 50 μm long rectangular shaped cantilever beams.
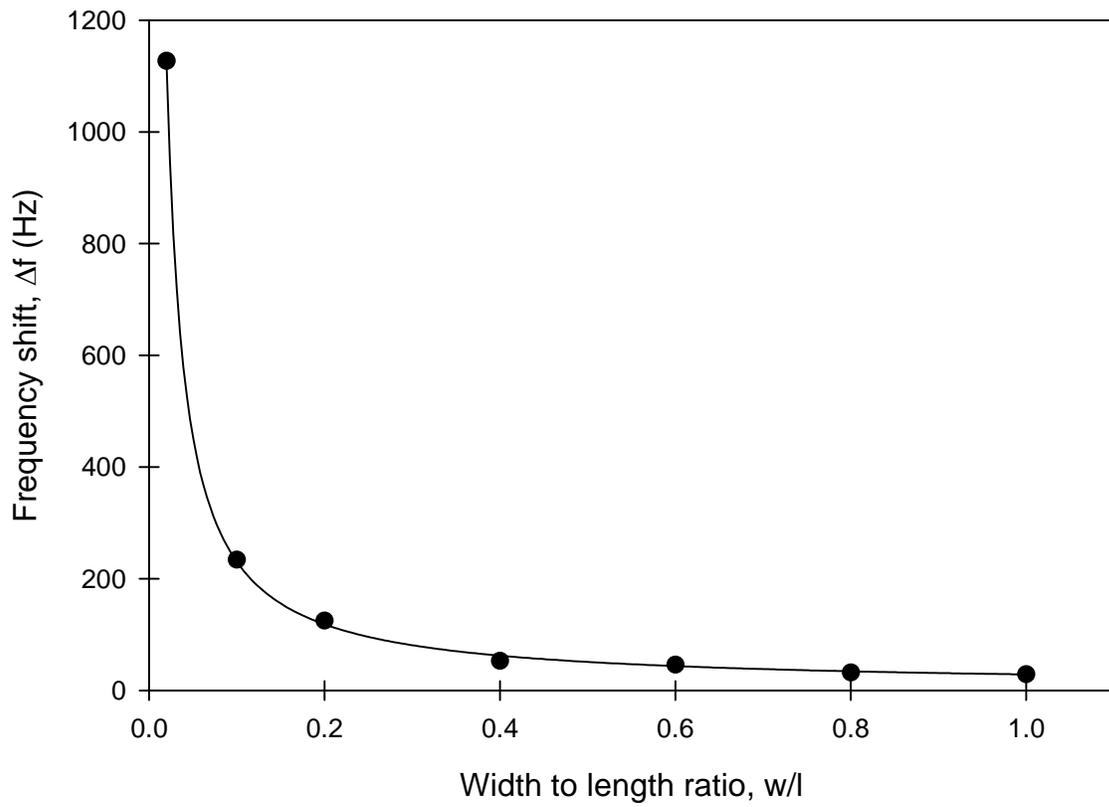
Figure 14: Plot showing numerically calculated frequency shift vs. the width to length ratio of 50 μm long rectangular shaped cantilever beams.

From Figure 14 it can be seen that as the width of the beam decreases, the sensitivity of the device increases rapidly below 10 μm width. As the MEMS based sensor devices require some type of transduction element on the beam structures for detection, such as piezoresistive elements, and these geometries do not offer enough area to define those features, researchers are investigating other kind of geometrical shapes, such as the triangular shaped ones. The triangular shaped geometries increase the stiffness, while reducing the effective mass acting on the original beam structures. Thus, it improves the resonant frequency of the structure which is evident from the equation (5).

As the accuracy of the FEA results are strongly dependent on the type and number of elements that are used in the analysis. In these simulations, SOLID187 element had been used which is supported by the ANSYS software. It is a higher order 3 dimensional tetrahedral structural element with 10 nodes. These elements, as shown in the Figure 15, have 3 degrees of translational degrees freedom at each node in x, y and z directions. It is well suited for meshing irregular geometrical shapes, such as in these cases. One disadvantage of using this element is that the size of these elements cannot be controlled manually; ANSYS software automatically generates mesh but it can be set to generate finer or coarser mesh size by using 1 to 10 scale. In all of these simulations, the scale was set to 1, which is the finest mesh size. One way to achieve finer meshes with a certain level of mesh size is by defining the thickness smaller. This is due to the fact that SOLID187 element has a certain limit for maximum allowable aspect ratios. This is why in these simulations, cantilever beam structure thicknesses were chosen to be 0.5μm, though, in reality the fabricated cantilever beam structures are approximately 1μm thick.
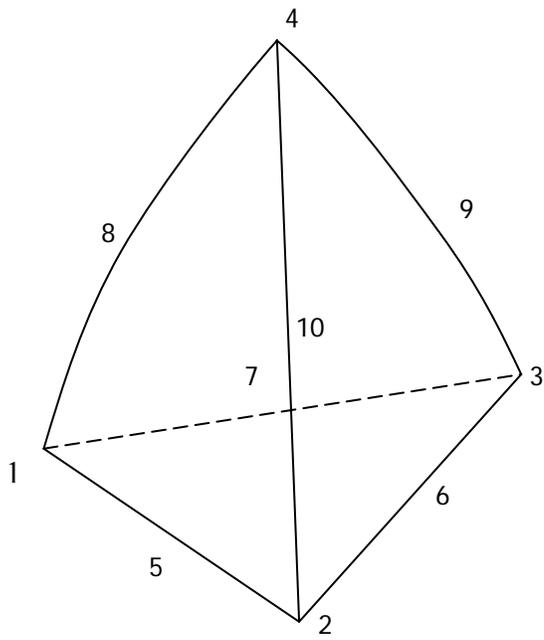
Figure 15: Tetrahedral structural element SOLID187 with 10 nodes, each with 3 translational DOF.

The initial FEA results are listed in the Table A.1 in the APPENDIX A section of this document. From equations (5), it is clear that the frequencies of a certain beam structure, increases with the stiffness of the beam and decreases with the effective mass acting on it, while from equation (6) it is observed that the frequency shift is proportional to the ratio of the measurand mass to the effective mass acting on it. Thus, for a constant measurand or the attached mass in the FEA simulations, the frequency shift should increase with lesser mass of the original beam structure, unless the stiffness is reduced, which is represented in the simulation results for the shapes 4 through 10 of Table A.1. In the case of the triangular shapes, as the mass of the beam structure is reduced, while increasing the stiffness of them, it translates into higher frequencies and higher frequency shifts for the attached mass. The main disadvantages with this type of geometries are that, due to the smaller areas near the tip of the beams, there is not much room available for fabricating the sensing pads to catch the measurands, such as bacteria, virus or DNA for biosensors. Thus, triangular geometries with an added square or rectangular area at the tip of the beam structures, as shown in the cases for shapes 27 to 30 in the Table A.1, were investigated.

From the initial numerical results listed in the Appendix A section, it is clear that the resonant frequency of the geometries are dominated by 2 dominating parameters: the clamping width at the fixed end and the effective mass acting upon the cantilever beam structure at the free end. As the minimum clamping width is limited by the geometry of the transduction element of the MEMS based sensing devices and the resolution of the microfabrication facilities available, in this case the minimum width is approximately 20-25 μm. So, to further investigate these dominating parameters, modal analysis were performed on some of the geometrical shapes, and compared with the regular rectangular shaped one. Table 3 lists these geometries that have the

same length of 50 μm and 0.5 μm thicknesses as before, and a fixed clamped width of 25 μm for comparison. It lists the resonant frequency, their corresponding frequency shifts due to the attachment of a 0.285 picogram of mass on the tip of the beam structure, and their corresponding mass sensitivity of the geometries. From the results listed in Table 3, it can be seen that the mass sensitivity of the triangular shape F shows an order of magnitude improvement than the regular rectangular shaped one. But, as it was mentioned before that the triangular shape does not offer enough area at the tip of the beam structure to capture the analytes, other geometries were also investigated. The shape I, which provides enough area to fabricate sensing pads, shows more than 3 fold improvement in mass sensitivity over the regular rectangular shape.

Table 3: Comparison of numerical performances of different geometrical shapes
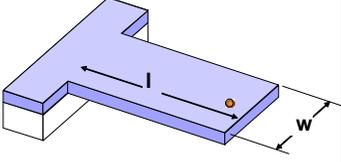
Shape ID	Shape geometry	Shape Parameters (μm)	Resonant frequency, f (Hz)	Frequency shift, Δf (Hz)	Mass sensitivity, Δf/Δm (Hz/pico-gm)
A		$l = 50,$ $w = 25$	194,532	49	171.93
B		$l = 50,$ $w = 25,$ $w_1 = 30,$ $l_1 = 20$	179,588	41	143.86
C		$l = 50,$ $w = 25,$ $w_1 = 20,$ $l_1 = 20$	213,575	69	242.11
D		$l = 50,$ $w = 25,$ $w_1 = 15,$ $l_1 = 20$	125,295	36	126.32
E		$l = 50,$ $w = 25,$ $w_1 = 15,$ $l_1 = 20$	126,070	31	108.77
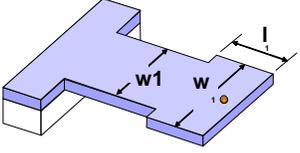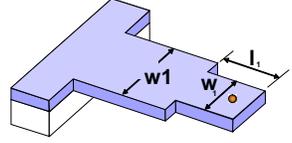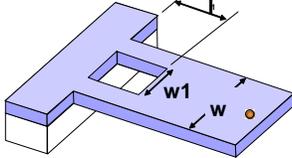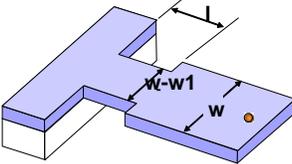
Table 3: Comparison of numerical performances of different geometrical shapes

Shape ID	Shape geometry	Shape Parameters (μm)	Resonant frequency, f (Hz)	Frequency shift, Δf (Hz)	Mass sensitivity, Δf/Δm (Hz/pico-gm)
F		$l = 50$, $w = 25$	390,387	506	1775.44
G		$l = 50$, $w = 25$, $w_1 = 10$	371,707	464	1628.07
H		$l = 50$, $w = 25$, $w_1 = 10$	251,691	123	431.58
I		$l = 50$, $w = 25$, $w_1 = 10$, $l_1 = 10$	262,729	162	568.42
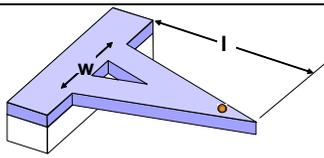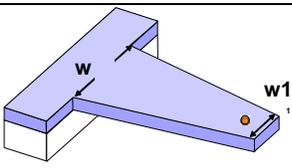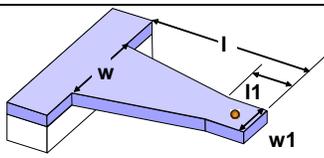
CHAPTER 4

VERIFICATION OF THE FEA RESULTS

In this section, the FEA results obtained from the previous chapter were verified by measuring the resonant frequency and their corresponding shifts due to the attachment of a known mass in the AFM system. A simplistic experimental approach to simulate the same type of effect due to the addition of a known mass on the tip of the different geometrical shapes of cantilever beam structures, as used for the modal analyses of the geometries, was employed. Different shapes of cantilever beam structures had been fabricated using SOI (silicon-on-insulator) wafer. As the length of the AFM tip cantilever beam structures of the AFM system available in our facilities are of 125 μm in length, the microcantilever beam structures of different geometries were fabricated of the same length of 125 μm, and width and other geometrical parameters were similarly designed 2.5 times larger of the geometrical shape parameters investigated in the previous chapter. The resonant frequencies of the beams were measured in the JEOL SPM 5200 (AFM) system. Then polystyrene beads of 10 micron diameter were attached on the surface of the tip to simulate the mass addition, and the corresponding change in their resonant frequencies were measured in the AFM system; thus, calculating the resonant frequency shift of the corresponding cantilever beam structures.

A SOI (silicon-on-insulator) wafer of 4 inch diameter was used to fabricate different shapes of cantilever beams, by etching silicon in the Inductively Coupled Plasma (ICP) based Advanced Silicon Etcher (ASE) system from the Surface Technology Systems (STS). The SOI wafers used in this process have a thin layer of silicon-oxide, called BOX layer, or buried oxide layer. This oxide layer is of approximately 1 micron thickness in between the thinner device layer of silicon of approximately 4 microns and the thicker bulk handle layer of silicon of approximately 450 microns. This oxide layer acted as an etch stop for the deep reactive ion etching (DRIE) process in the ASE system. The microfabrication process flow chart is attached below in the Flow chart 4.1. The three geometries; shape A, F and I that are listed in Table 3, were investigated by fabricating AFM tip microcantilevers. The resonant frequency and their corresponding frequency shifts were measured and compared. Figures 16 through 18 show these three geometries with poly-beads attached on their tips. Figure 19 through 21 show sample responses of those geometries in the AFM system at three different pressure levels that were measured.

Flow Chart 4.1: Microfabrication process flow chart for the AFM tip microcantilevers

Step 1: Bare double side polished SOI wafer

Step 2: Spin coat top surface with AZ5214E photoresist

Step 3: Expose with UV light using the top side mask & develop in AZ400K developer

Step 4: Etch device layer Si in ASE

Step 5: Strip off photoresist

Step 6: Spin coat photoresist to protect the top surface

Step 7: Spin coat bottom surface with AZ4620

Step 8: Expose with UV light using the bottom side mask & develop in AZ400K develop

Step 9: Etch bulk substrate layer Si in ASE

Step 10: Strip off photoresist

Step 11: Etch silicon oxide in 10 : 1 HF solution to release free standing structure

Figure 16: SEM images showing fabricated AFM tip microcantilever of shape A.
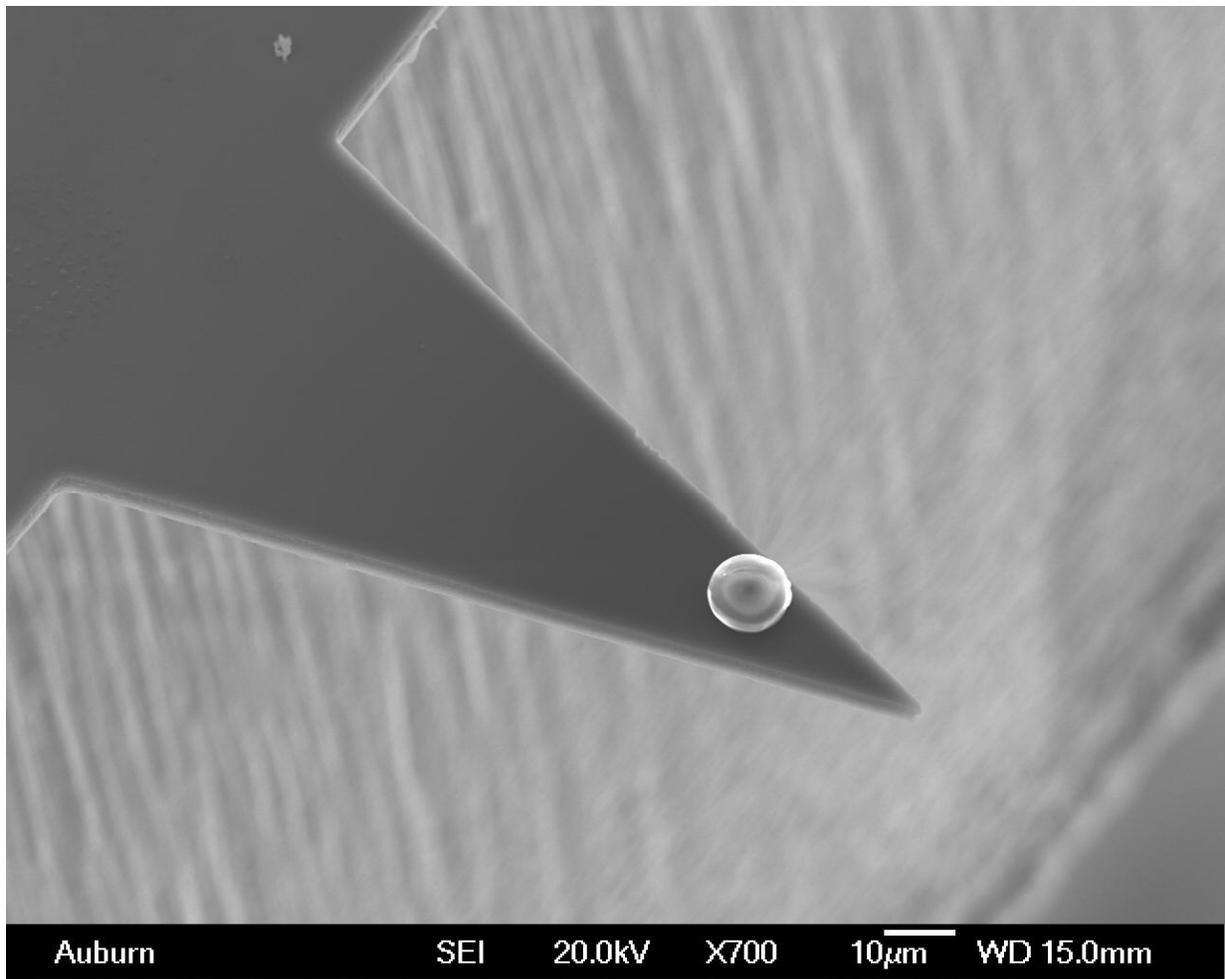
Figure 17: SEM images showing fabricated AFM tip microcantilever of shape F.
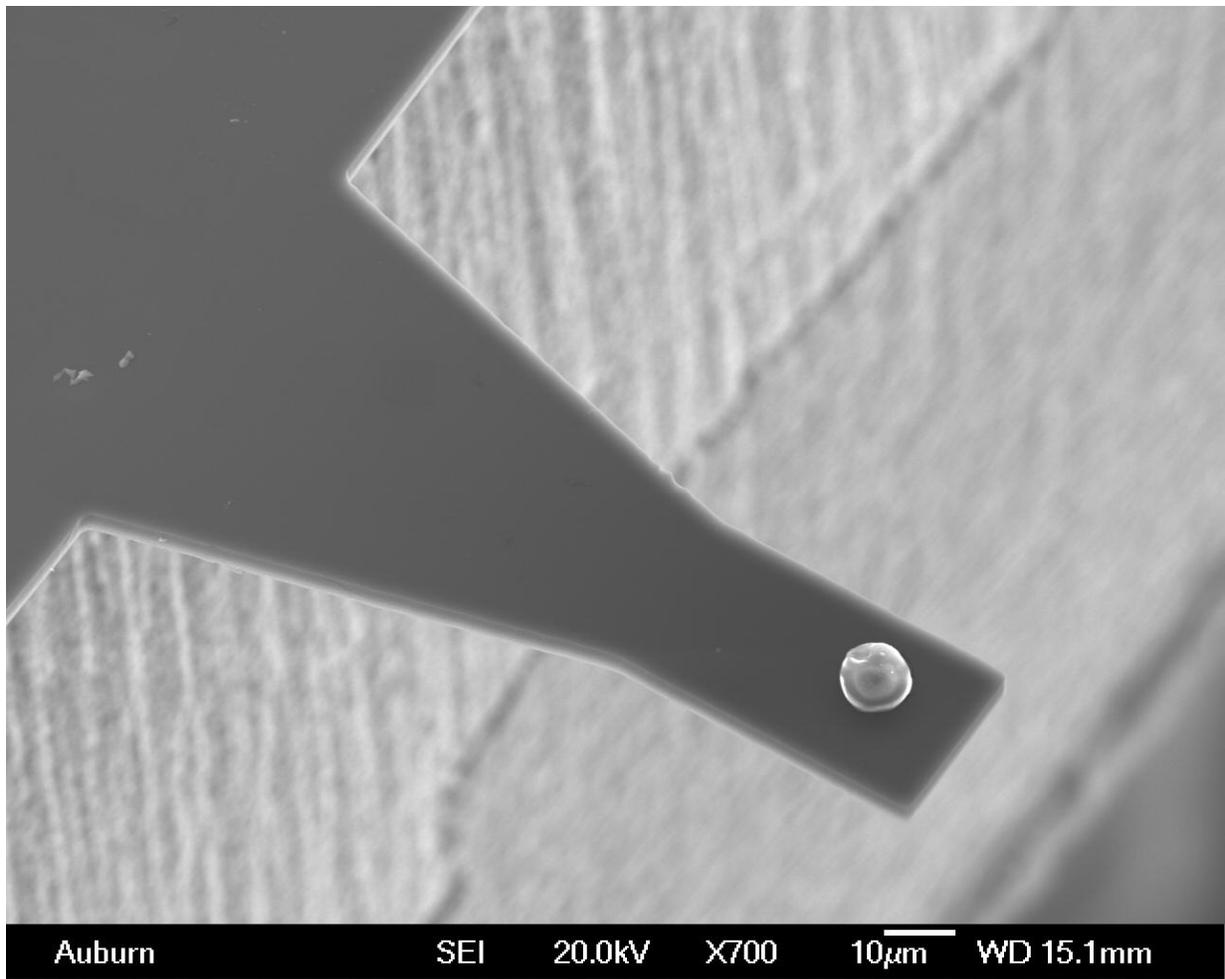
Figure 18: SEM images showing fabricated AFM tip microcantilever of shape I.

Shape A (in ambient pressure)
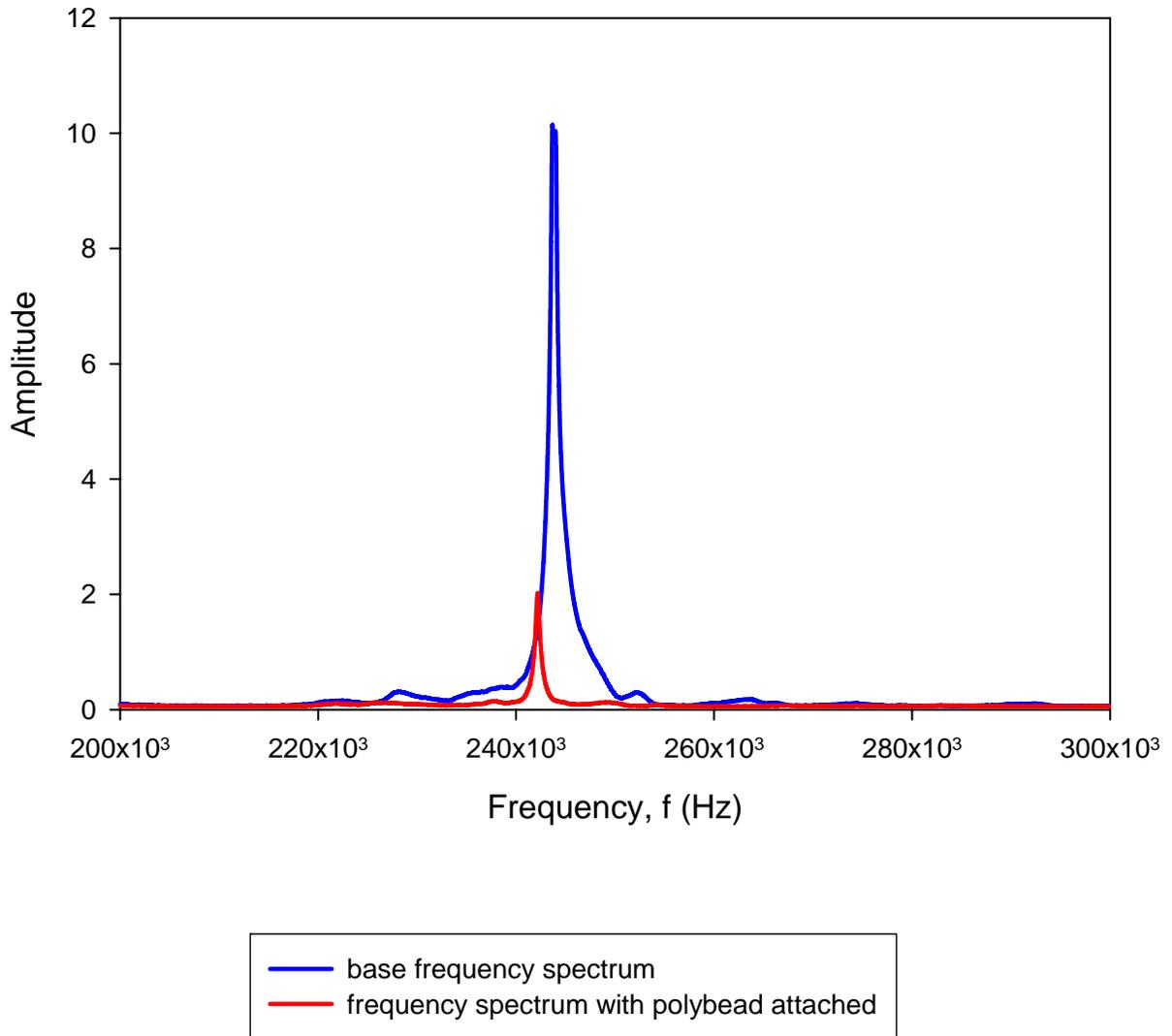
Figure 19: Frequency spectrums obtained by the AFM system of shape A; with & without

attaching poly-bead at ambient pressure.

Shape F (in 75 mTorr)
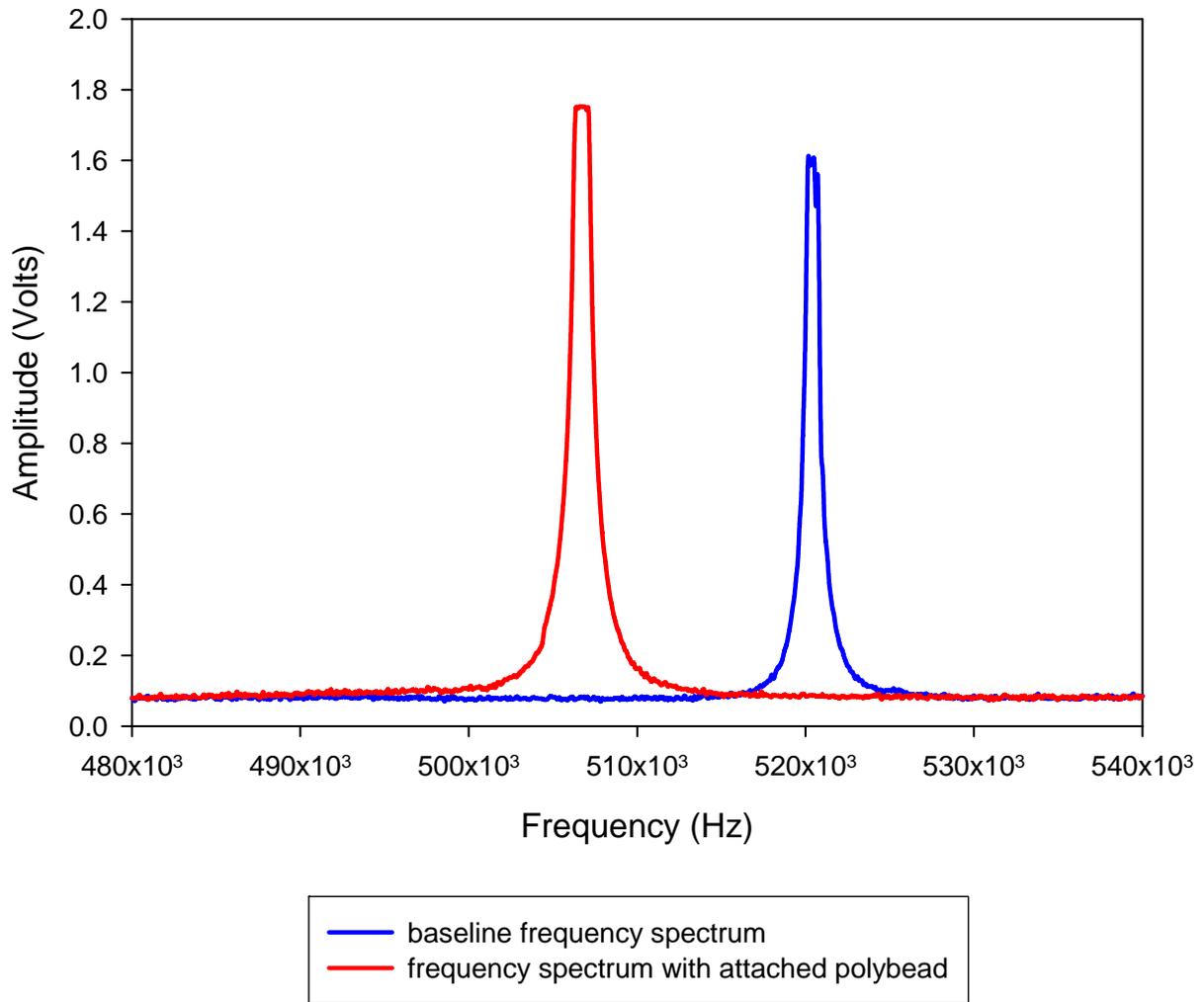
Figure 20: Frequency spectrums obtained by AFM of shape F; with & without attaching poly-

bead at 75 mtorr pressure.
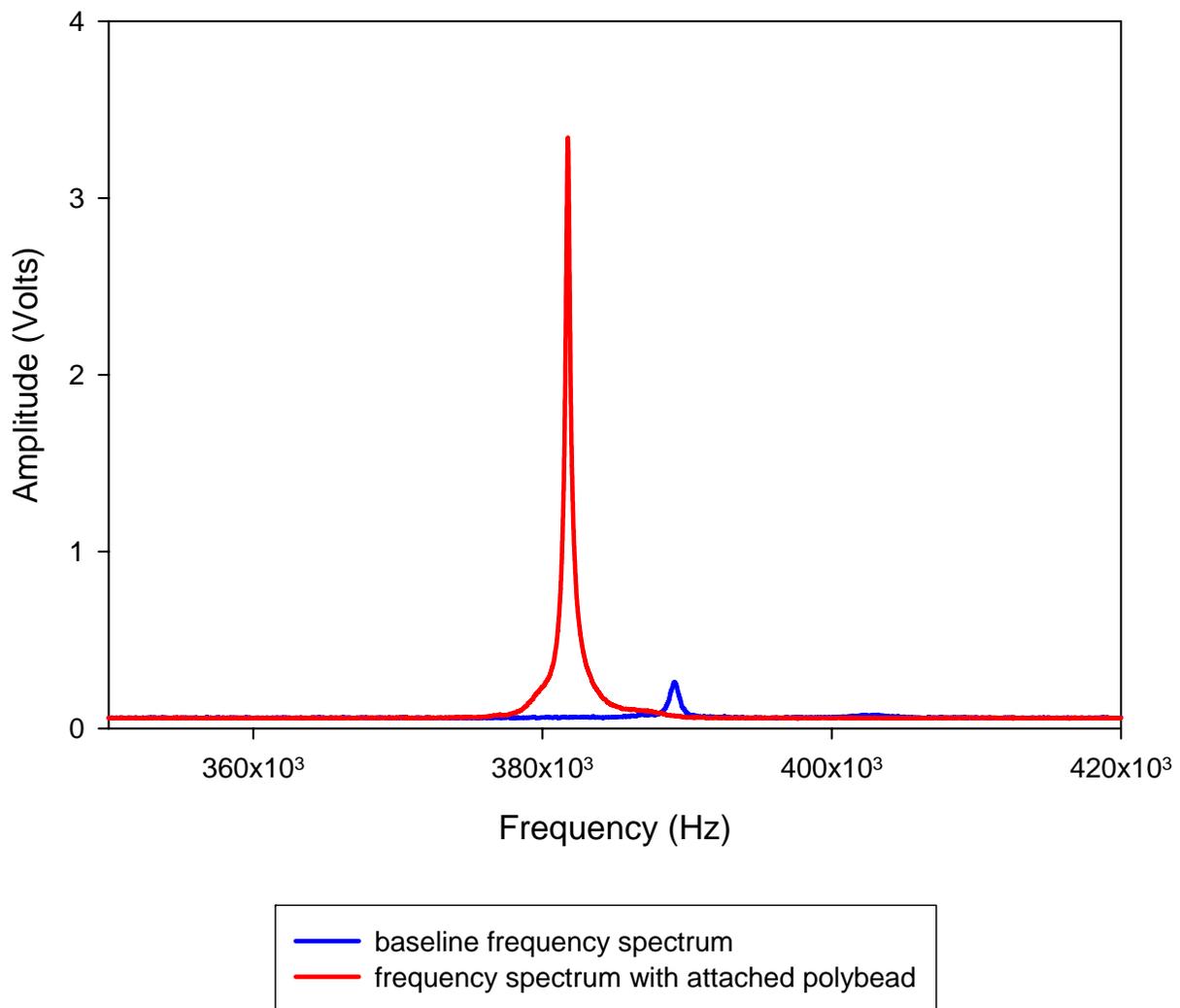
Figure 21: Frequency spectrums obtained by AFM of shape I; with & without attaching poly-

bead at 30 mtorr pressure.

Table 4 lists the resonant frequency, frequency shift and mass sensitivity of the best performing geometries of shape F and I, along with the regular rectangular shape A, tested in different ambient pressures. From these results, it can be seen that the performance of the shapes in terms of the mass sensitivity are almost the same as the ones obtained by the modal analysis results listed in Table 3. Shape F has a mass sensitivity of an order of magnitude higher than the regular rectangular shape A, while shape I has a mass sensitivity of more than 3 times higher than the shape A. These experimental results agreed quite well as the ones predicted by the FEA results. Although, the baseline frequency spectrum of these structures should have higher q-factor than the ones with the attached mass, but in some cases it showed otherwise. This was due to the fact that more optical signal got reflected off of the poly beads than the surface of the cantilever tip and was detected by the laser detector. This also made the q-factor data of the frequency spectrum listed on Table 4 unreliable.

Table 4: Comparison of experimental performances of different geometrical shapes

Shape ID	Ambient Pressure (Torr)	Resonant Frequency, f (kHz)	Q factor	Frequency Shift, Δf (kHz)	Mass Sensitivity, Δf/Δm (Hz/pico-gm)
A	760	243.750	356.571	1.562	3.04
	$7.5X10^{-4}$	244.336	250.200	1.465	2.85
	$3X10^{-4}$	244.238	227.364	1.367	2.66
F	760	519.358	759.743	13.694	26.67
	$7.5X10^{-4}$	520.630	592.133	13.989	27.24
	$3X10^{-4}$	520.430	592.133	13.887	27.04
I	760	388.086	331.167	7.109	13.84
	$7.5X10^{-4}$	389.160	664.167	7.402	14.41
	$3X10^{-4}$	389.160	664.167	7.402	14.41

CHAPTER 5

DAMPING EFFECT ON GEOMETRIES

To investigate the damping effect on these geometries and their performances, same A, F and I shaped cantilevers, described in the previous two chapters, were tested in the same manner. The resonant frequency of these geometries was measured in air at different pressure levels, starting from atmospheric pressure to the lowest vacuum pressure attainable by the AFM system. Theoretically, since the triangular shape offers less area at the free end of the structure, it should show the least effect of damping on the structure, while rectangular shape should show the maximum damping effect among these three geometries. As the modified geometry offers intermediate area between the rectangular and the triangular shapes, it should show an effect in the intermediate range between the other two geometries. To investigate this phenomenon, this experiment was set up. During the thought process behind this experiment, the results were expected to show the changes in resonant frequency for different geometries as a function of pressure as shown in the schematic plots attached in Figure 22.

The resonant frequency of the cantilever beam structures of these geometrical shapes were measured at different pressure levels from the atmospheric pressure of 10^5 pascal to 10^{-2} pascal that can be achieved by the vacuum pumps of the JEOL SPM 5200 (AFM) system. This range of pressures has been divided into three separate regions [33-38]. At low pressure levels
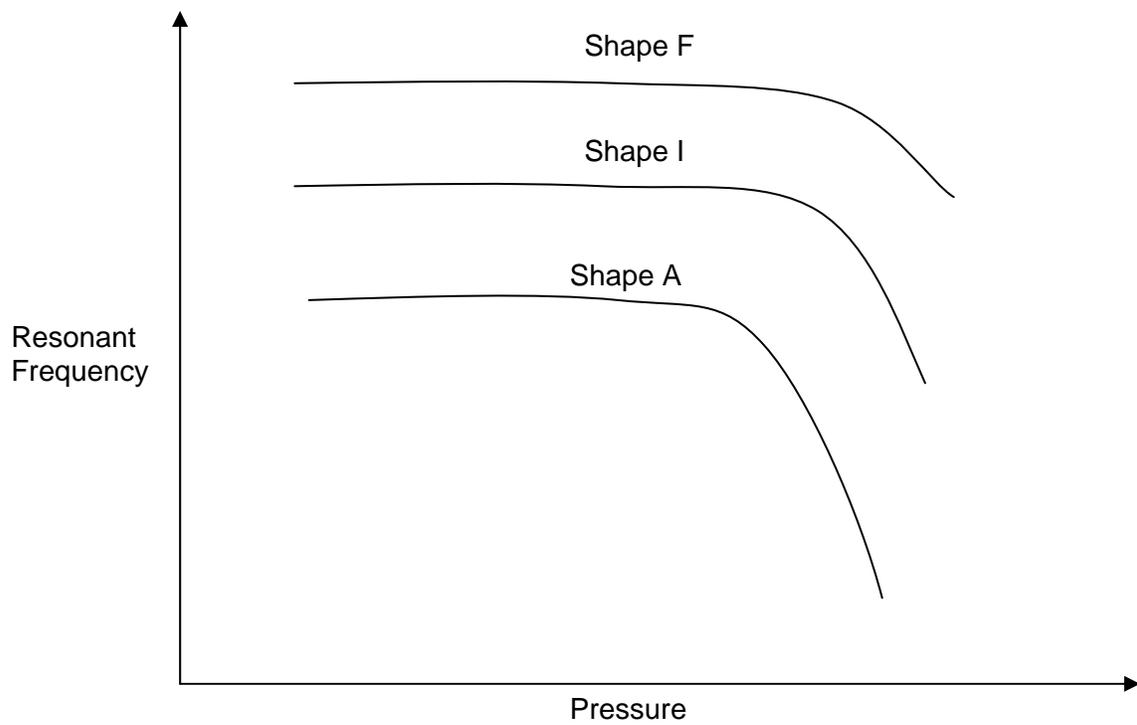
Figure 22: Schematic figure showing expected pressure dependence on different geometrical

shapes.

the vibrating cantilever beam structure loses energy due to internal damping, known as the intrinsic regime. At this pressure level air molecules can be considered non-interacting with the vibrating structure. Thus, the damping effect due to the medium can be neglected. At higher pressure levels, near the atmospheric pressure, the damping effect is dominated by the external effect imposed by the molecules present in the medium. This region of external damping is referred to as the viscous regime. In between these two regimes, there is a transition regime where both the internal and the external damping effects play roles.

In this experiment, fabricated cantilever beam structures were tested in the AFM system available in the laboratory facilities at Auburn University. Those test samples were put in the AFM tip holder and actuated by the system, while the chamber was pumped down by using the vacuum pumps of the system. The JEOL SPM 52OO system has a roughing pump and a turbo pump connected in series to pump down the chamber in the range of 10^{-2} Pa. To record intermediate pressure level data, the automatic control of the roughing pump and the turbo pumps were disabled. This kept the system at two different pressure levels, namely 10^{-2} Pa and 10^4 Pa, by independently controlling those two pumps. From the literatures [33-38], it was found that the transition regime starts around 10^4 Pa and the viscous regime continues through the atmospheric pressure level. Since the goal of this experiment was to investigate damping effect on the geometries due to the presence of air, data points at these pressure levels were required. So, to achieve that goal two leaks were introduced in the vacuum line of the AFM system. One bigger, open and shut, valve with another micro-valve attached in series, were introduced into the vacuum line. The micro-valve was adjusted manually to stabilize the pressure at certain levels, which was read from the pressure gage attached to the line near the valves. This made it possible to record data at the pressure range from 10^4 Pa to 10^5 Pa.

During the experiment, at each pressure level, the system was kept for a few minutes to stabilize at the pressure level, and then a frequency scan was performed to record the resonant frequency and the Q-factor data. Figures 23 through 25 show the typical responses of the shapes A, F and I consecutively. Although some of the spectrum curves show better and cleaner plots than the others, they clearly show the resonant frequencies of the structures. After measuring the resonant frequencies of the structures, 10 nm of Ti and 75 nm of Au layers were deposited to mimic the addition of mass on the structures. These layers were deposited in the E-beam system available in the microfabrication lab of Auburn University. After that the structures were tested again, and the corresponding resonant frequencies at each pressure levels were measured.

All these resonant frequency and the corresponding Q-factor data are listed in Tables 5 through 7 for the shape A, F and I respectively. Here, it can be seen that the Q-factor data for different samples did not follow a clear trend, except for increasing with the higher pressure level. This might be due to multiple factors; such as the noises introduced by the leaks that were incorporated to achieve intermediate pressure levels. Also, the samples had a small amount of undercuts, approximately 10 to 15 microns on the backside of the SOI wafer. This was due to the fact that when using the Bosch process in the ASE system to etch through 450 to 500 microns thickness of the wafer, it leaves approximately 10 to 15 microns of undercuts. Because of this, the fixed ends of the cantilever beam structures were not exactly clamped; they experienced small displacement during actuation. Thus, the Q-factor values were not exactly reliable for these experiments.

SHAPE A
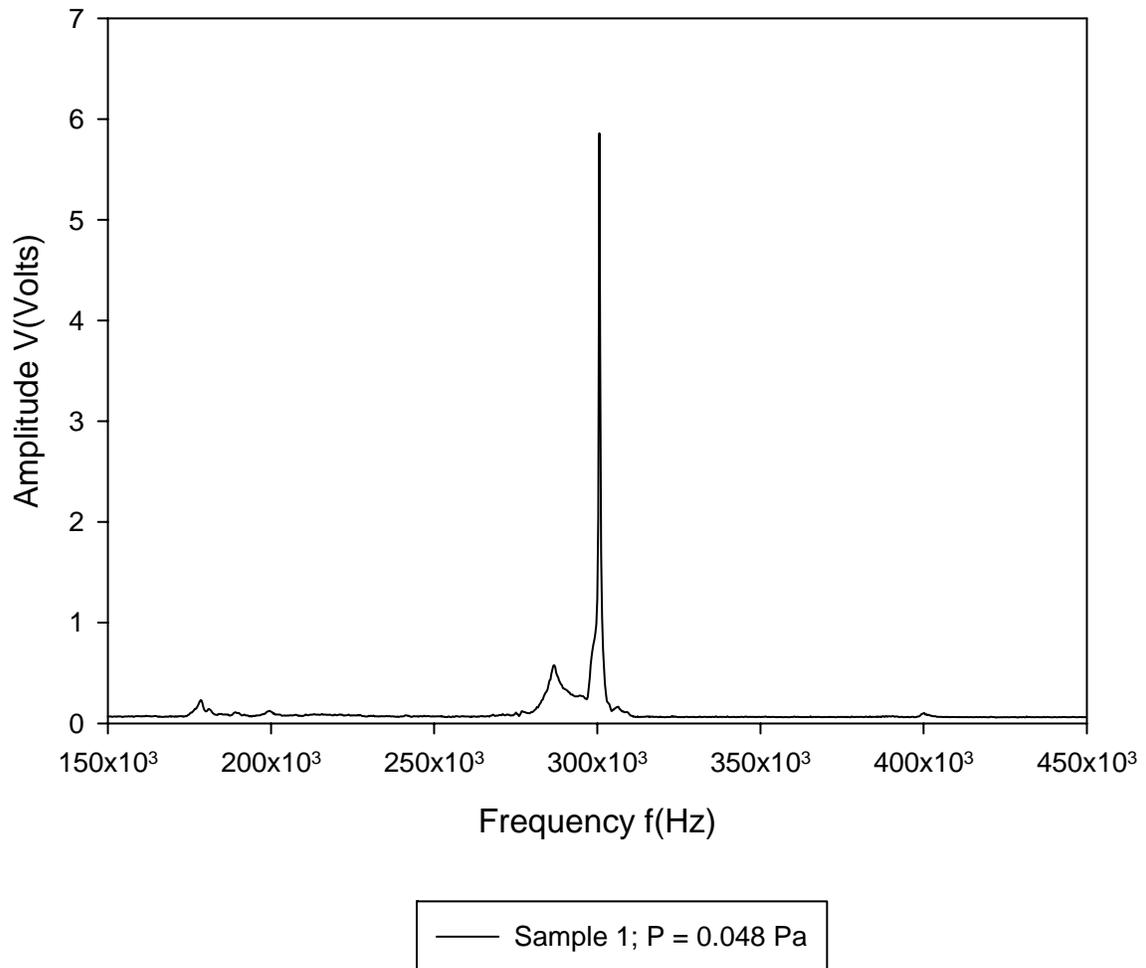
Figure 23: Frequency spectrum for the sample no. 1 of Shape A at 0.048 Pa pressure.

SHAPE F
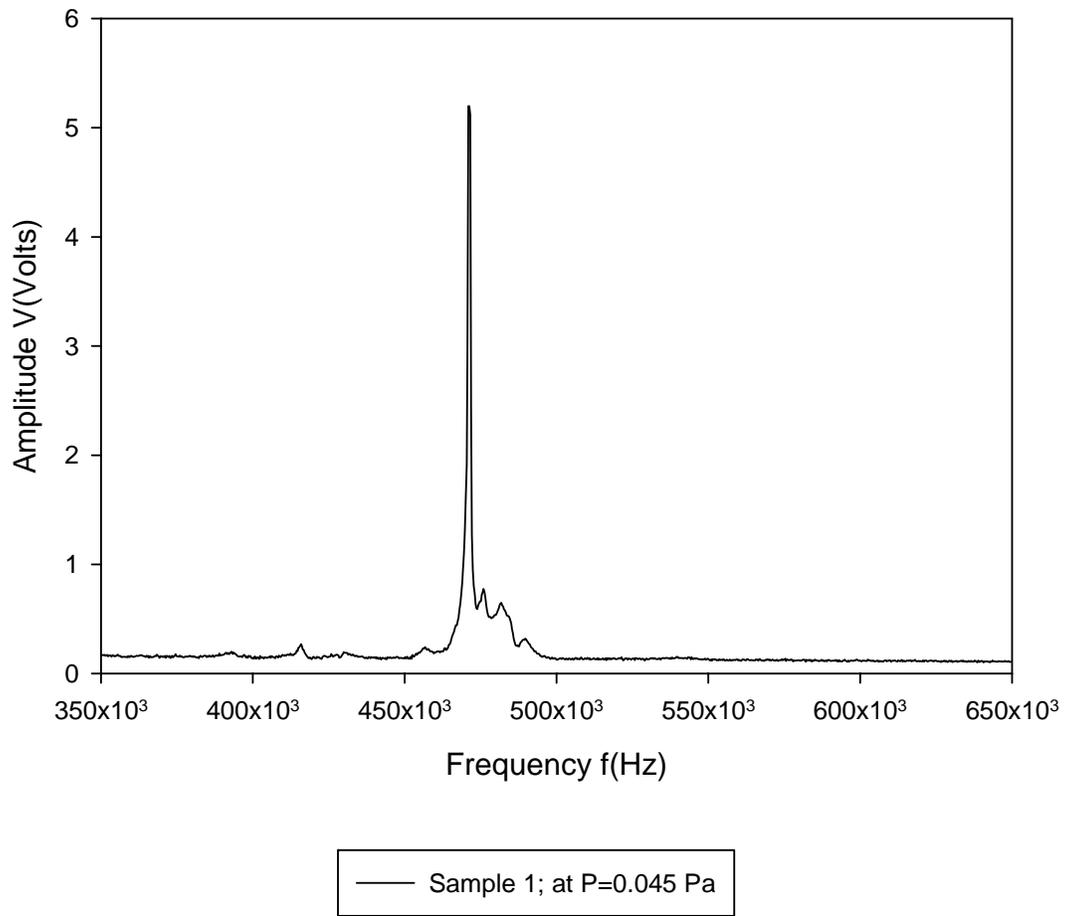
Figure 24: Frequency spectrum for the sample no. 1 of Shape F at 0.045 Pa pressure.

SHAPE I
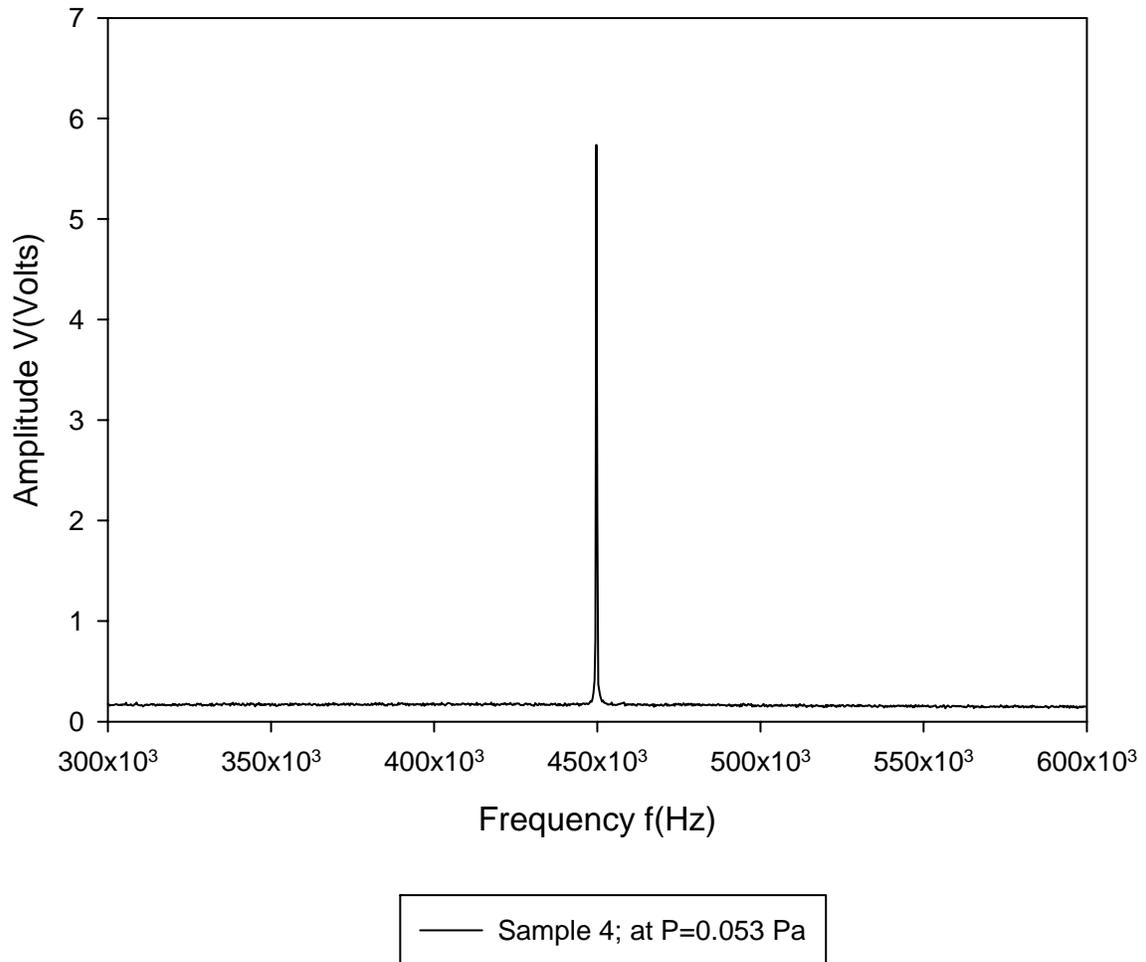
Figure 25: Frequency spectrum for the sample no. 4 of Shape I at 0.053 Pa pressure.

Table 5: Resonant frequency responses of shape A

Sample No.	Status	Pressure (Pa)	Frequency (kHz)	Q-factor
1	Before metal deposition	101324.7200	299.707	511.500
		79993.2000	300.000	512.000
		66661.0000	300.000	512.000
		57328.4600	300.000	512.000
		9999.1500	300.586	1026.000
		0.0480	300.586	1026.000
	After metal deposition	101324.7200	285.3520	487.000
		77326.7600	285.3520	487.000
		66661.0000	285.3520	487.000
		53328.8000	285.6450	487.500
		8665.9300	285.6450	487.500
		0.0480	285.6450	487.500
2	Before metal deposition	101324.7200	213.037	290.867
		79993.2000	213.281	291.200
		66661.0000	213.281	291.200
		57328.4600	213.525	291.533
		9999.1500	213.770	291.867
		0.0480	213.770	291.867
	After metal deposition	101324.7200	199.121	54.373
		78659.9800	199.121	58.257
		66661.0000	199.121	58.257
		55995.2400	199.365	58.329
		9332.5400	199.609	62.892
		0.0533	199.609	68.133
3	Before metal deposition	101324.7200	270.410	461.500
		79993.2000	270.703	462.000
		66661.0000	270.996	462.500
		58661.6800	270.996	925.000
		7999.3200	271.289	926.000
		0.0613	271.289	926.000
	After metal deposition	101324.7200	254.980	435.667
		78659.9800	255.273	435.667
		66661.0000	255.273	435.667
		53328.8000	255.273	871.333
		7999.3200	255.566	872.333
		0.0507	255.859	872.333

Table 6: Resonant frequency responses of shape F

Sample No.	Status	Pressure (Pa)	Frequency (kHz)	Q-factor
1	Before metal deposition	101324.7200	470.117	534.889
		81326.4200	470.410	535.222
		71993.8800	470.410	535.222
		61328.1200	470.410	535.222
		9332.5400	470.996	535.889
		0.0453	470.996	535.889
	After metal deposition	101324.7200	441.211	502.000
		78659.9800	441.504	502.333
		66661.0000	441.504	502.333
		55995.2400	441.504	502.333
		9999.1500	441.797	502.333
		0.0533	441.797	502.333
2	Before metal deposition	101324.7200	483.887	550.556
		75993.5400	484.180	550.889
		66661.0000	484.180	550.889
		53328.8000	484.180	826.333
		9332.5400	485.059	827.833
		0.0800	485.059	827.833
	After metal deposition	101324.7200	453.516	516.333
		75993.5400	453.809	516.333
		66661.0000	453.809	516.333
		50662.3600	453.809	516.667
		8665.9300	454.102	516.667
		0.0427	454.102	775.000
3	Before metal deposition	101324.7200	499.707	189.519
		75993.5400	499.707	213.208
		66661.0000	500.000	213.333
		53328.8000	500.000	213.333
		8665.9300	500.586	244.095
		0.0733	500.879	244.238
	After metal deposition	101324.7200	469.043	400.250
		75993.5400	469.336	400.500
		66661.0000	469.336	400.500
		55995.2400	469.336	400.500
		8665.9300	469.629	400.500
		0.0453	469.629	400.750
4	Before metal deposition	101324.7200	511.719	64.691
		75993.5400	512.012	64.728
		66661.0000	512.012	62.417
		53328.8000	512.012	62.417
		8665.9300	513.184	194.630
		0.0587	513.184	250.238
	After metal deposition	101324.7200	480.078	74.485
		75993.5400	480.371	74.530
		66661.0000	480.664	74.576
		51995.5800	480.664	78.127
		8665.9300	480.957	78.127
		0.0613	480.957	78.175

Table 7: Resonant frequency responses of shape I

Sample No.	Status	Pressure (Pa)	Frequency (kHz)	Q-factor
1	Before metal deposition	101324.7200	392.3830	669.667
		75993.5400	392.3830	669.667
		66661.0000	392.3830	669.667
		53328.8000	392.3830	669.667
		7999.3200	392.9690	1341.333
		0.0533	392.9690	1341.333
	After metal deposition	101324.7200	367.2850	626.833
		77326.7600	367.5780	627.333
		66661.0000	367.5780	1254.667
		55995.2400	367.5780	1254.667
		8665.9300	367.8710	1255.667
		0.0613	368.1640	1255.667
2	Before metal deposition	101324.7200	393.2620	671.167
		78659.9800	393.2620	671.167
		66661.0000	393.5550	671.167
		57328.4600	393.5550	671.167
		8665.9300	393.8480	1344.333
		0.0533	394.1410	1345.333
	After metal deposition	101324.7200	369.9220	420.889
		75993.5400	369.9220	631.333
		66661.0000	369.9220	631.333
		51995.5800	370.2150	631.833
		8665.9300	370.5080	631.833
		0.0427	370.8010	631.833
3	Before metal deposition	101324.7200	296.7770	202.600
		75993.5400	296.7770	253.250
		66661.0000	296.7770	253.250
		53328.8000	297.0700	253.250
		8665.9300	297.3630	253.750
		0.0613	297.6560	254.000
	After metal deposition	101324.7200	275.6840	313.667
		75993.5400	275.9770	471.000
		66661.0000	275.9770	471.000
		51995.5800	275.9770	471.000
		8665.9300	276.5630	944.000
		0.0453	276.5630	944.000
4	Before metal deposition	101324.7200	448.8280	766.000
		79993.2000	449.1210	766.500
		66661.0000	449.1210	766.500
		57328.4600	449.1210	766.500
		8665.9300	449.7070	1535.000
		0.0533	449.7070	1535.000
	After metal deposition	101324.7200	423.9260	723.500
		78659.9800	424.2190	724.000
		66661.0000	424.2190	724.000
		49329.1400	424.5120	724.500
		8665.9300	424.8050	1450.000
		0.0400	425.0980	1450.000

Sandberg et al. [38] had developed an analytical expression for pressure dependence of the resonant frequency of a regular rectangular shaped cantilever beam structure:

$$f = f_0\left(1 + \frac{\pi M w p}{4RT\rho h}\right)^{-\frac{1}{2}}$$
(17)

Here, f_0: intrinsic resonant frequency,

M: molar mass of the medium (in this case 28.97 gm/mol for air),

p: pressure,

R: gas constant (8.314 J/mol.K),

T: temperature (room temperature, approximated as 300 K),

ρ: density of the beam material (for Si it is 2.329 gm/cm^3),

& h: thickness of the beam.

From equation (17), the relative resonant frequency can be calculated using the following expression:

$$\Delta f = f_0\left[\left(1 + \frac{\pi M w p}{4RT\rho h}\right)^{-\frac{1}{2}} - 1\right]$$
(18)

Here, the intrinsic resonant frequency was assumed to be the same as the maximum resonant frequency that was measured at the lowest pressure attained by the system during testing for each samples. To calculate the analytical results for a rectangular shape cantilever, the average value of the thickness of the samples and the average value of the intrinsic resonant

frequencies of the samples were used. The relative resonant frequencies were calculated from the experimental data for each of the samples of all three geometries and plotted in Figures 26 through 28. To make a comparison, the analytical model for a rectangular cantilever was attached to each of the plots for different shapes. Those plots are combined in the Figure 29 for better comparison. From these plots it can be seen that there are no significant differences among the three geometries, in terms of relative resonant frequencies. Proving the expectation to be wrong which was summarized in the schematic plots attached in Figure 21. This may be due to the fact that the relative resonant frequency is highly dependent on the intrinsic resonant frequency, as can be seen from the Equation (18). Although the damping effects on the triangular shape might be the smallest, its intrinsic resonant frequency was the highest. Thus, the change in the resonant frequency became comparable to that of the other shapes. On the other hand, the rectangular shape had the largest surface area for damping effect to take place, while it had the lowest intrinsic resonant frequency. Thus, the change in the resonant frequency due to damping became comparable to the other shapes.

Figures 30 through 32 show the relative resonant frequencies for each sample, with the deposited metal layers and without adding any metals on them. From these figures it can be seen that the resonant frequency shifts due to the addition of mass on them were the highest for the triangular shapes, as expected. The lowest level of resonant frequency shifts due to the mass addition were exhibited by the regular rectangular shape structures, while the modified shaped structure showed resonant frequency shifts intermediate to the other two shapes. These results are in good agreement with the results listed in the previous chapters.

SHAPE A
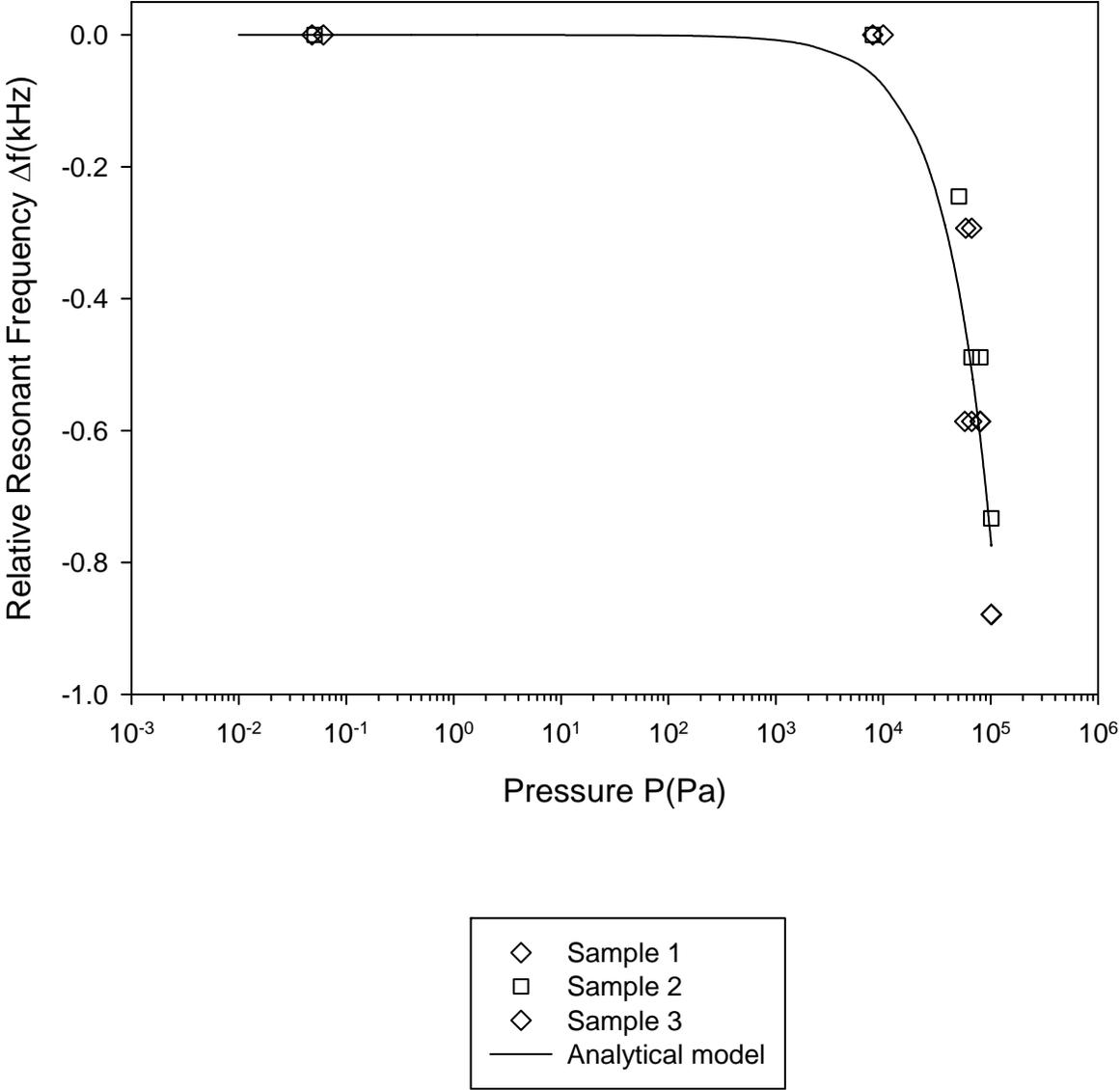
Figure 26: Relative resonant frequency as the function of pressure for shape A.

SHAPE F
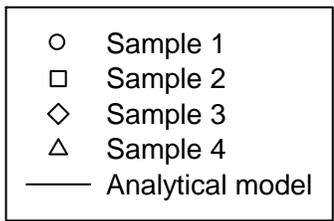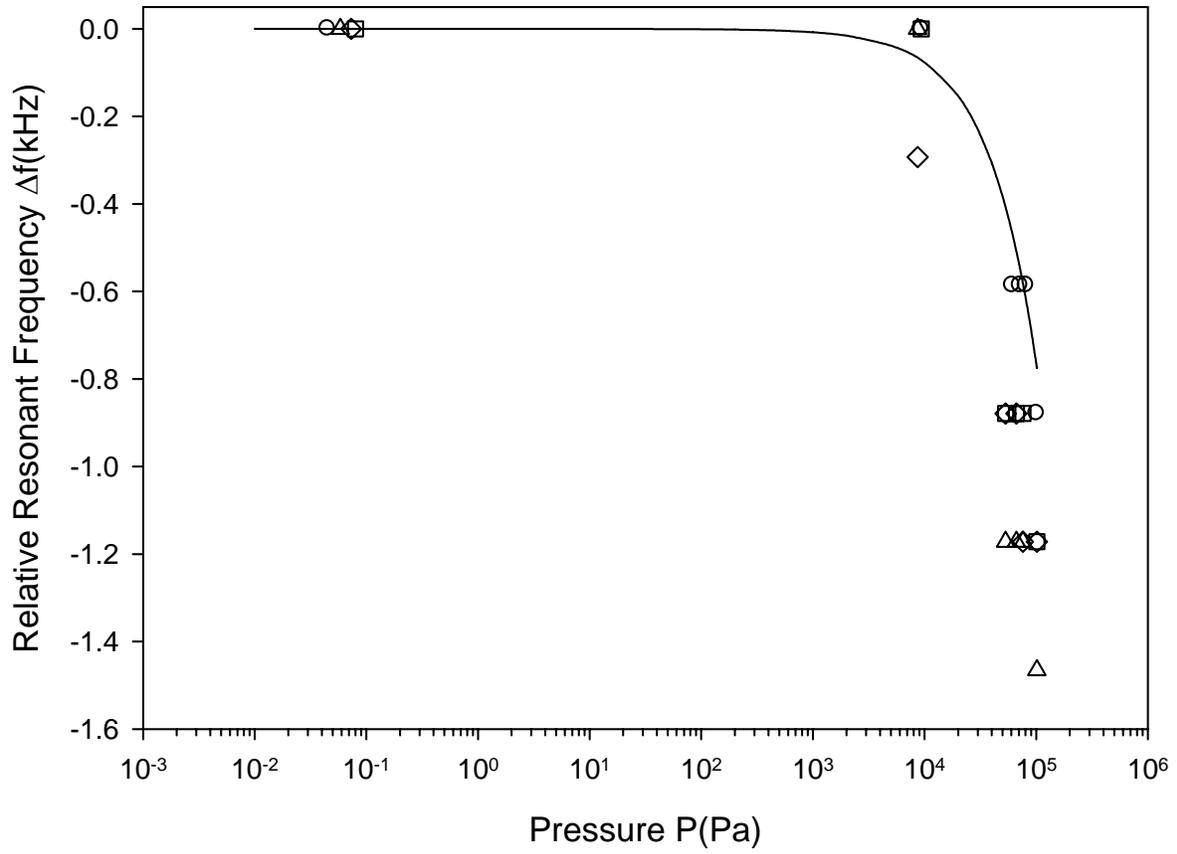
Figure 27: Relative resonant frequency as the function of pressure for shape F.

SHAPE I
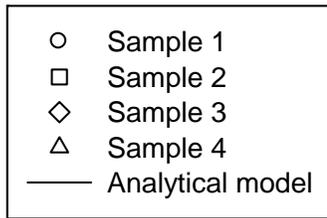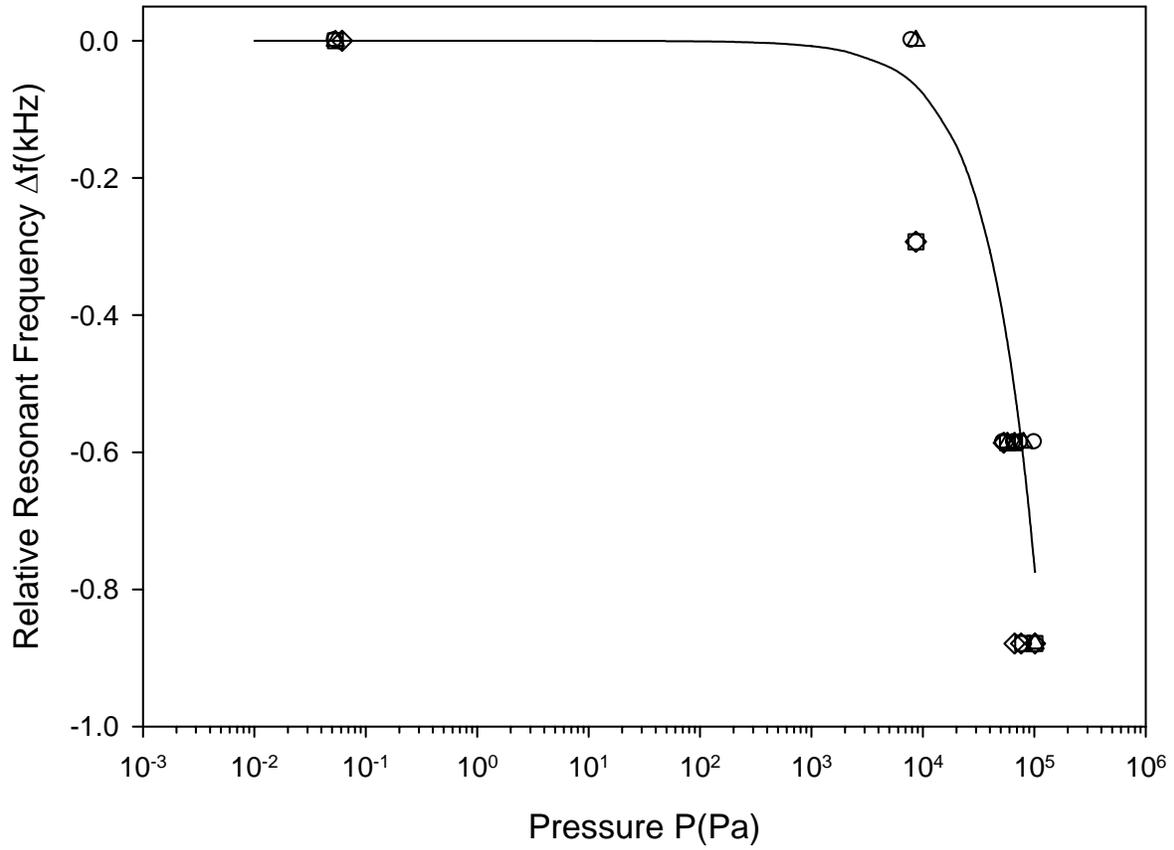
Figure 28: Relative resonant frequency as the function of pressure for shape I.

COMPARSION OF DIFFERENT SHAPES
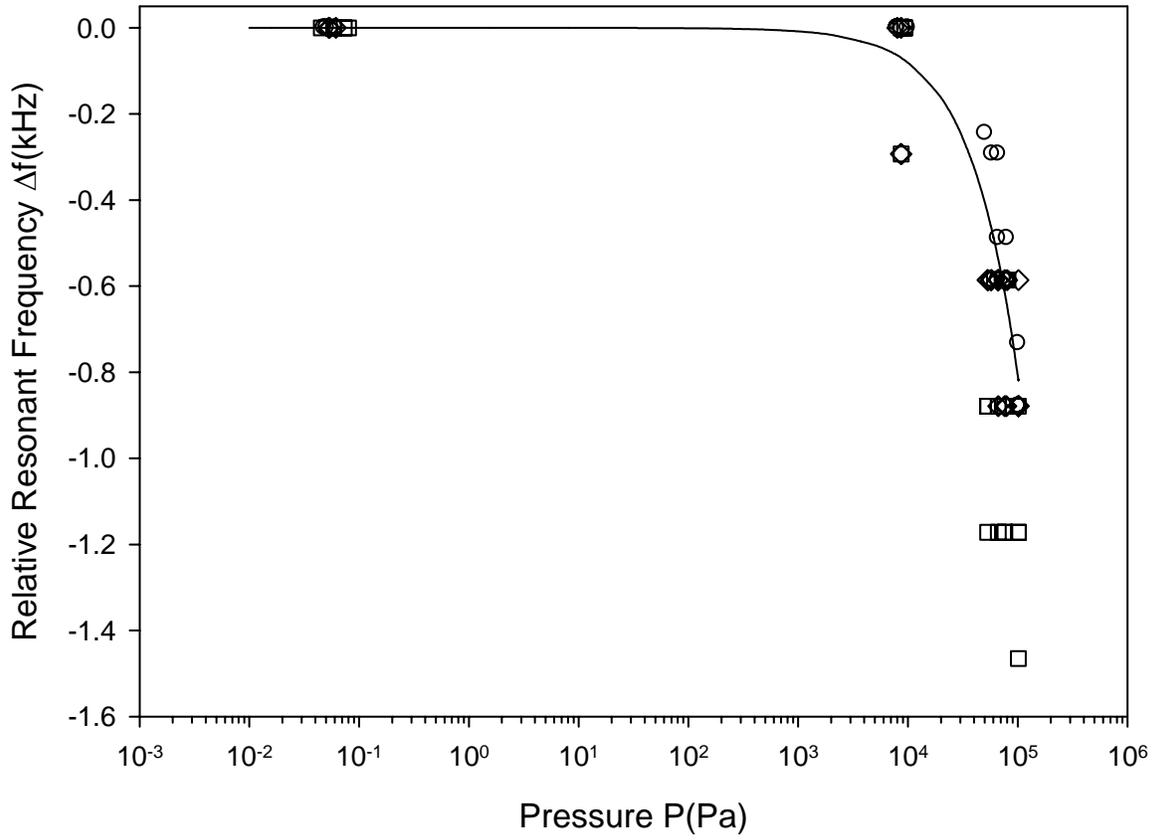
Figure 29: Comparison of relative resonant frequency vs. pressure plots for all three geometries.
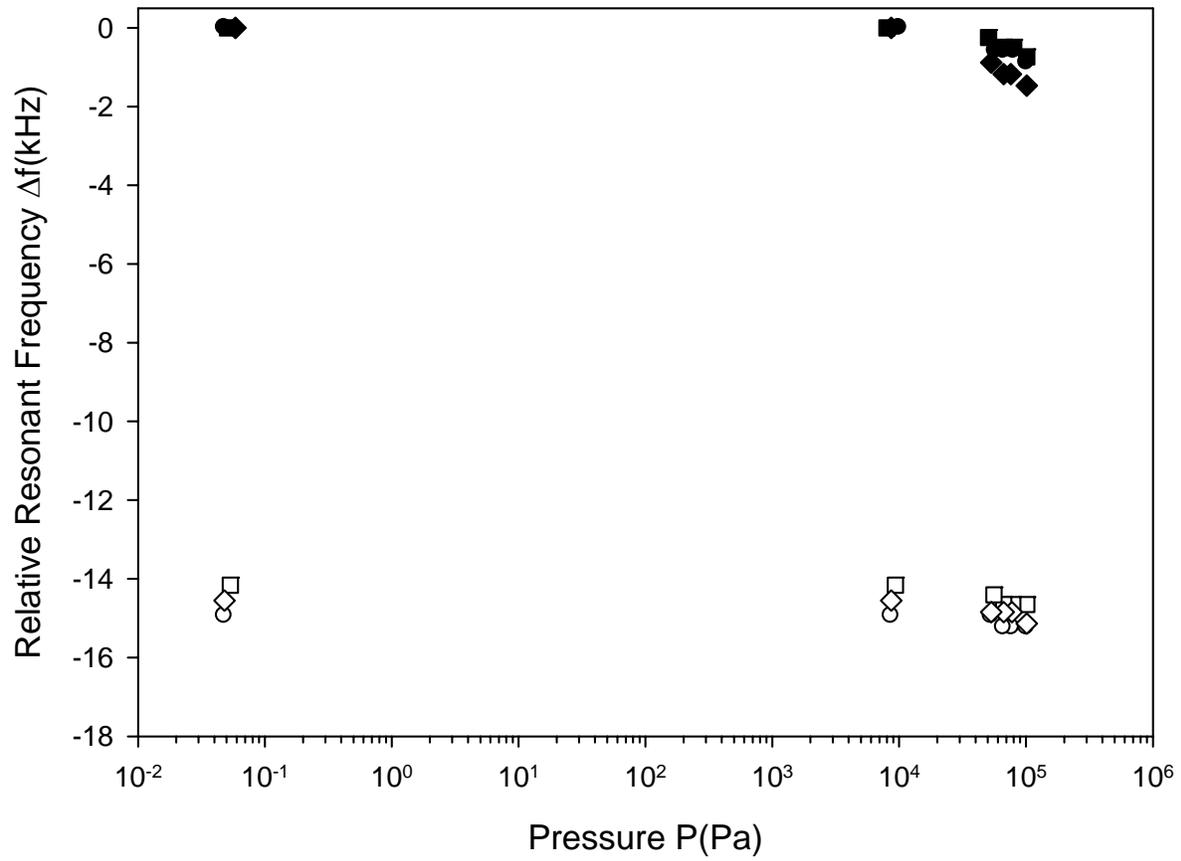
SHAPE A

Figure 30: Effect of mass addition on relative resonant frequency vs. pressure plot for shape A.

SHAPE F
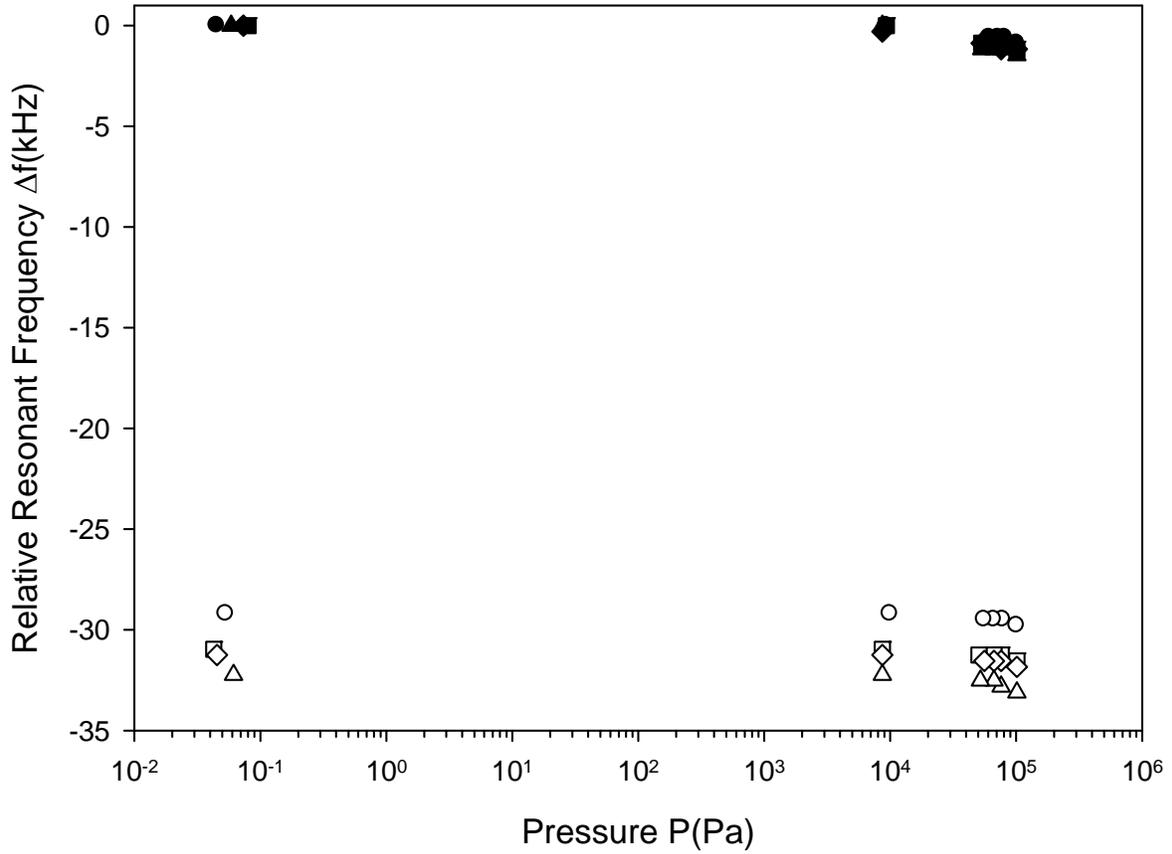
Figure 31: Effect of mass addition on relative resonant frequency vs. pressure plot for shape F.

SHAPE I
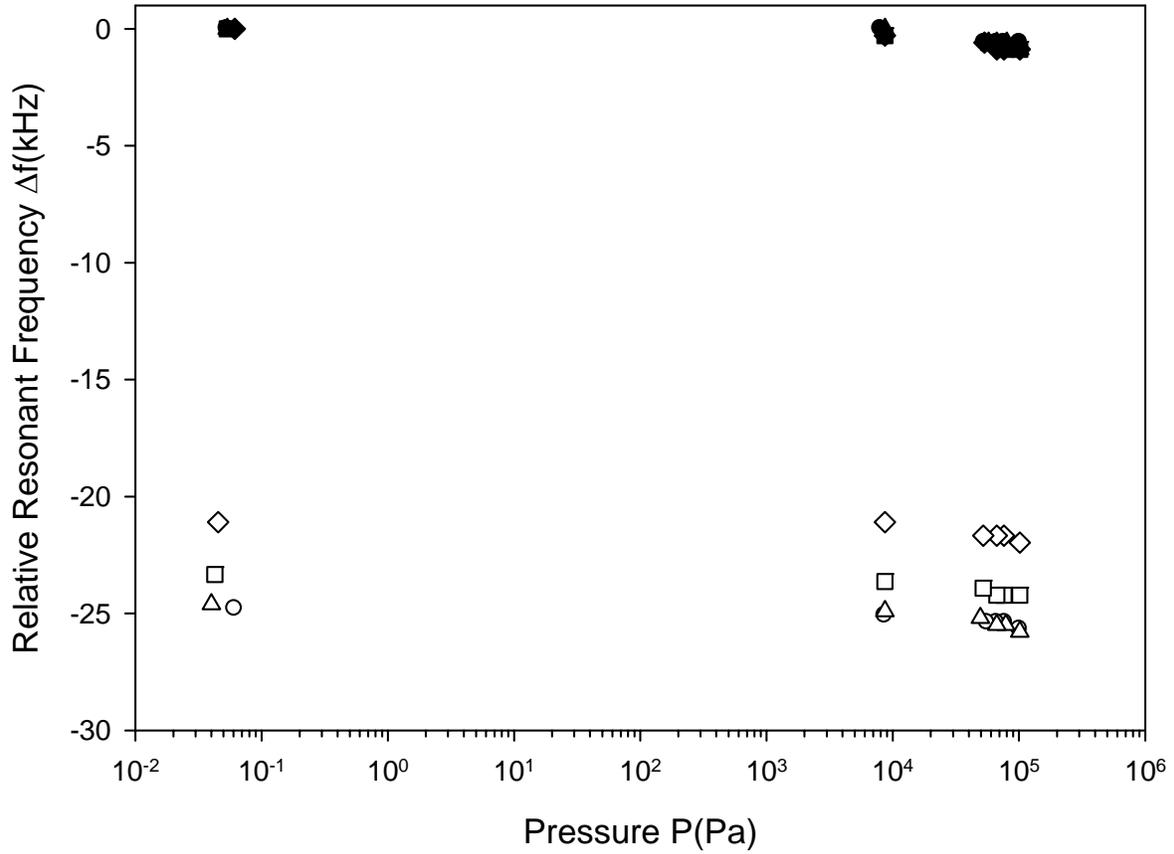
Figure 32: Effect of mass addition on relative resonant frequency vs. pressure plot for shape I.

CHAPTER 6

MICROFABRICATION PROCESS OF THE MEMS DEVICES

It was planned to etch silicon by using bulk micromachining techniques of wet etching to form the cantilever beam structures for the MEMS devices. Thus, the process of fabricating these devices start with (100) oriented silicon wafers with an average thickness of 500 μm. The process flow chart is attached below in Flow Chart 6.1. Single side polished p-type 500 μm thick 4 inch wafers were used for the fabrication of the MEMS devices. First, the wafers were cleaned by following a few steps. The first step was to use B cleaning process of the RCA cleaning procedure [39] for cleaning organic and ionic contaminations, by using a solution made of deionized water (DI-H_2O), ammonium hydroxide (NH_4OH) and hydrogen peroxide (H_2O_2) in the ratio of 5:1:1 and at a temperature of 55 to 60°C for 10 minutes. Although, it is recommended to use this cleaning solution at 70 to 80°C, it was found that at temperatures higher than 60°C, the solution tends to slightly attack the bare silicon surface. After the wafers were rinsed in DI-H_2O and dried with blowing N_2 gas on them, they were kept in an oven at 120°C for 20 minutes for dehydration bake in a nitrogen environment. Then, two minutes of oxygen plasma cleaning in the MATRIX system was performed; at 300 watts power, 5 torr pressure and 40% O_2 in N_2 gas.

Right after these cleaning and drying processes, silicon nitride layer was deposited in the Low Pressure Chemical Vapor Deposition (LPCVD) system. This nitride layer forms the base of the cantilever beam structure and acts as an etch stop for the bulk micromachining of silicon, as it has a negligible etch rate compared to the etch rate of silicon in the [100] direction [40-41]. To reduce the residual stress in the silicon nitride layer grown in the LPCVD system, a low stress silicon nitride deposition recipe [42] had been used. According to the literature [43], if the ratio of the gases used, dichlorosilane (SiH_2Cl_2) to ammonia (NH_3), is 5:1 and the film is grown at 850°C temperature, the deposited silicon rich silicon nitride (Si_xN_y) layer should have a residual stress lower than 100 MPa. This low stress recipe was used and the silicon nitride was deposited at approximately 350 mtorr furnace pressure for 90 minutes. This deposited nitride layers of approximately 300 to 400 nm thicknesses on the wafers, along the length of the furnace tube. After the deposition the same cleaning procedures were used, as discussed above. Then low stress polysilicon layer was deposited in the same LPCVD system, by thermal decomposition of silane (SiH_4) gas at 650°C and approximately 400 mtorr process pressure. In this process, on average, a 100nm thick polysilicon layer was deposited across the furnace length for an approximately 17 minutes run. After deposition, the polysilicon layer was doped with phosphorous by using phosphorous diffusant, which is a solution of phosphosilicate glass. The wafer was then spun coated with the diffusant at 3000 rpm for 30 seconds and initially baked at 150°C for two minutes on a hotplate. Then the phosphorous was driven into the polysilicon layer at 1000°C in a furnace, while N_2 gas was flown inside the furnace at a flow rate of 5 sccm. The wafers were kept at that temperature inside the furnace for ten minutes, which makes a doping concentration in the range of approximately 10^{19} to $10^{20}/cm^3$. This gives piezoresistive characteristics to the polysilicon layer. After performing this drive-in step, the phosphosilicate

70

glass layer was stripped-off from the wafer surface, by using 10:1 ratio solution of DI-H_2O and HF. Then the wafer was prepared for patterning the piezoresistive transduction element for the sensor devices.

At first, the wafer was cleaned with the B cleaning solution for ionic and organic contamination. Then it was rinsed, dried and dehydrated by the same methods mentioned earlier. The only step that was done differently at this point was no O_2 plasma cleaning procedure was performed, which is due to the fact that the oxidation of the polysilicon layer should be kept at a minimum level. Otherwise, the devices would show Schottky type contact characteristics, instead of ohmic contact between the polysilicon and the metal layers. After dehydration bake at 120°C for 20 minutes, the wafer was kept inside an evaporating environment of hexamethyl disilazane (HMDS) for 5 minutes, which acts as a primer for the photoresist. Then it was spun coated with the AZ5214E IR positive photoresist at 3000 rpm for 30 seconds, which forms approximately 1.2 μ thick layer of photoresist. After spin coating, the wafer was soft baked at 105°C for 1 minute on a hotplate. Then, the 1st mask for the piezoresistors was aligned with the wafer flat for (100) orientation in the KARLSUSS MA6 mask aligner. The photoresist was exposed in UV light for 6 seconds at approximately 6 mW/cm^2 light intensity level; thus, resulting in a total dose of 36 mJ/cm^2 (approximately). After the exposure, the photoresist was developed in AZ400K developer solution of 1:2 ratio with DI-H_2O for approximately 18 seconds. As on this mask, only small areas are defined for the piezoresistors, most of the photoresist from the wafer ended up in the developing solution. When the wafer was pulled out of the solution it formed a very thin and optically undetectable layer of the photoresist on the surface. This was evident from the fact that when the polysilicon was etched in the Advanced Silicon Etcher (ASE), it did not form well defined piezoresistors. To resolve this issue a fresh batch of solution was

made and the wafer was dipped into the solution just for a moment to dissolve that undetectable monolayer of photoresist. After that the photoresist was flood exposed for post-develop flood exposure in UV light for 5 seconds. This helped to retain the small geometries of the devices, and after that the wafer was hard baked at 120°C for 1 minute on a hot plate.

The piezoresistors were defined by etching the polysilicon layer in the Advanced Silicon Etcher (ASE) system from the Surface Technology Systems (STS). In this inductively coupled plasma (ICP) etching system, the etching process was performed using alternate etching and sidewall passivating cycle with a process pressure of 36 mtorr. The etch cycle was of 8 seconds duration using sulfur hexafluoride (SF_6) gas at a flow rate of 130 sccm and O_2 gas at a flow rate of 13 sccm. The power applied in the magnetic coil generator was 600 watts, while 10 watts of power was applied in the platen generator. The passivation cycle was of 4 seconds duration using octafluorocyclobutane (C_4F_8) gas at a flow rate of 85 sccm with 600 watts of power in the magnetic coil only. This etching process was closely monitored through a glass window at the top of the chamber. After the etching process for the polysilicon layer was done, the photoresist was stripped off in acetone. Then, it was washed in isopropyl alcohol (IPA) or alternatively known as isopropanol, and DI-$H_2$0 in consecutive steps. After that the wafer was dried with N_2 gas blowing on the surfaces of the wafer.

The next step was to pattern the wafer for depositing metal pads and connectors of the MEMS devices. At first, the wafer was cleaned, dried and dehydration baked, as it was done during patterning the polysilicon layer. After that, it was put in HMDS evaporating environment for 5 minutes, and spun coated with the AZ5214 photoresist, as before. Then it was soft baked at 105°C for 1 minute on hotplate, and exposed in UV light using the metal layer mask, which was aligned in the mask aligner. The exposure time and dose was the same as in the previous step.

After exposure it was developed in the same AZ400K developing solution of 1:2 ratio for approximately 18 seconds. Then the photoresist was flood exposed for post-develop flood exposure, as before.

Now the wafer was ready for Cr-Au-Cr deposition in the E-beam system. The Cr layers act as an adhesion layer for the Au layer to stick on the polysilicon and the silicon nitride layers at the bottom, and the passivation layer on the top, which could be silicon oxide, silicon nitride, diamond like carbon (DLC) or silicon carbide. Just before depositing metals, the wafer was ion cleaned inside the E-beam chamber using Ar gas in a vacuum environment. This ensures a cleaner surface for the metal film growth and oxide removal from the exposed polysilicon layer. Thus, it ensured good ohmic contact between the polysilicon layer and the metal pads, and the removal of any residual photoresist from the exposed substrate. During the E-beam run, the base pressure was kept at less than $3X10^{-6}$ torr. Cr layer was deposited at 9.78 kilovolts voltage and 0.029 amps current, while Au layer was deposited at 9.82 kilovolts voltage and 0.130 amps current. The deposited thicknesses of the metal layers were 20nm of Cr, 180nm of Au and another 20nm of Cr, making the thickness of the metal layers approximately twice the thickness of the polysilicon layer. This ensured good step coverage. After that, the wafer was put in an ultrasonic bath, while submerged in acetone to perform lift-off technique, and thus, defining the metal pads. Figure 33 through 35 show pictures of piezoresistors and metal pads defined at this stage.
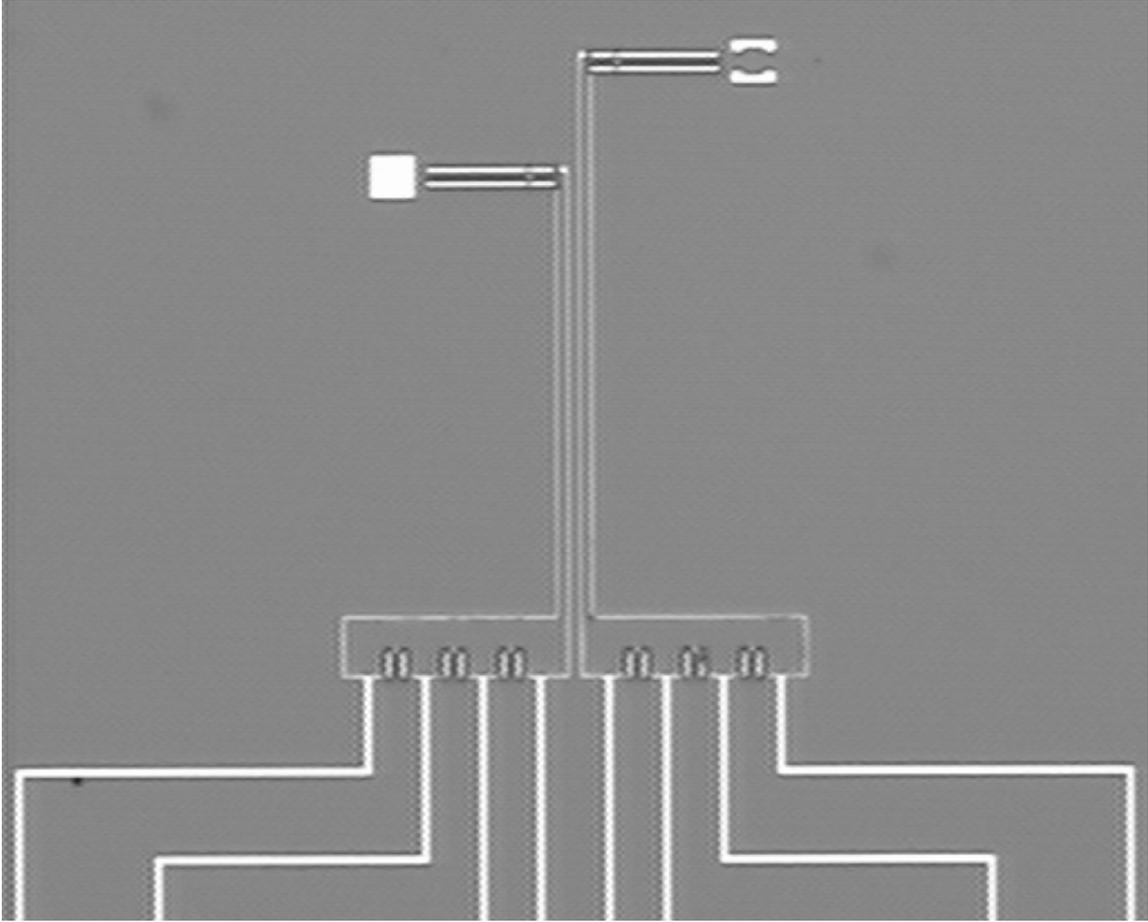
Figure 33: Picture of piezoresistance and metal connector arrangement in a rectangular shaped device.
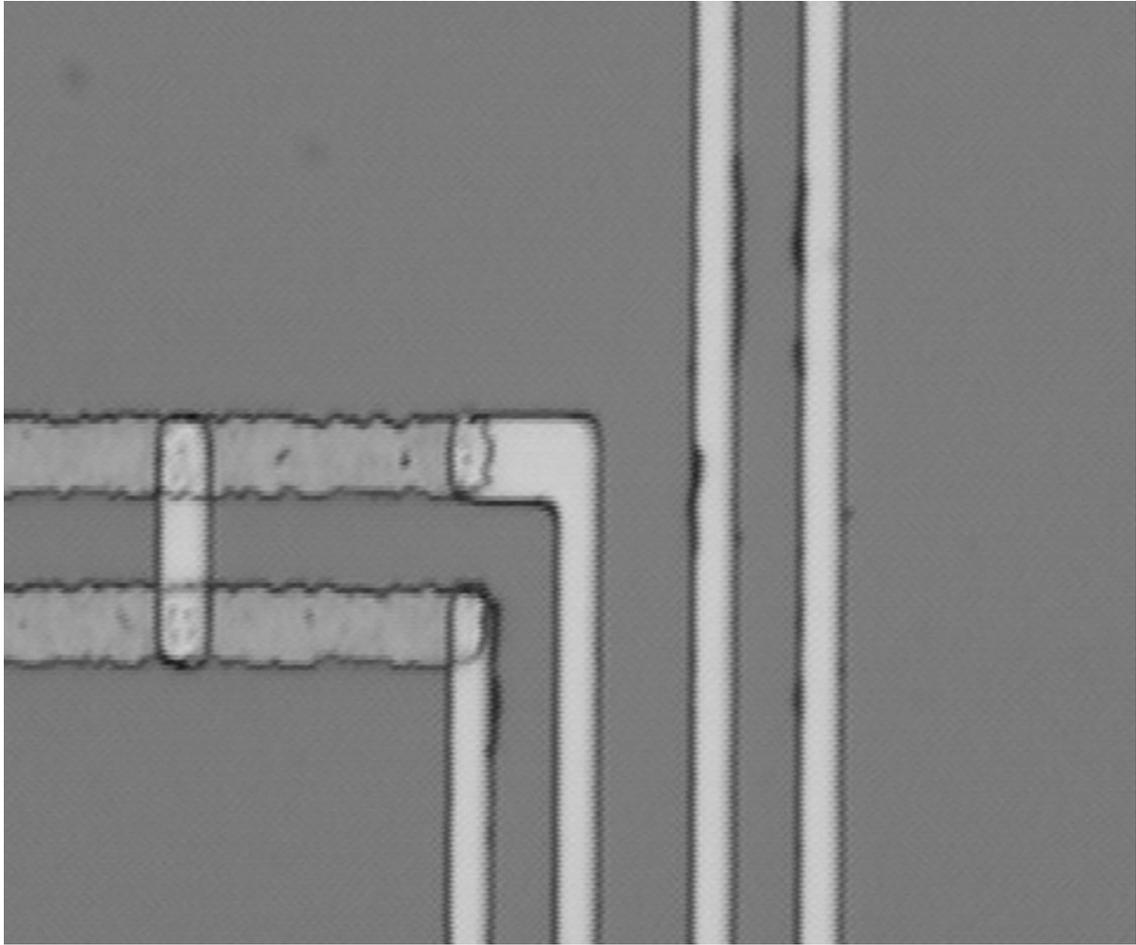
Figure 34: A close up picture of piezoresistive polysilicon pads and their metal connectors.
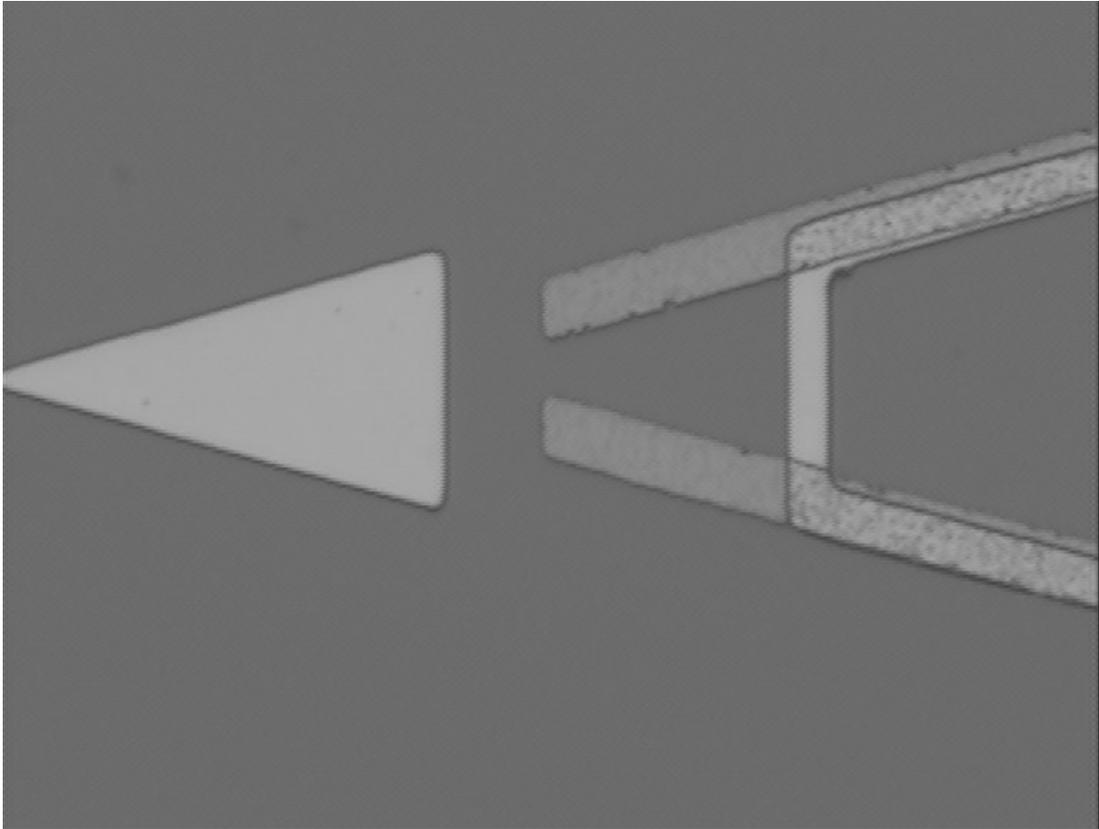
Figure 35: Picture of the sensing pad on a triangular shaped device.

The next stage was to put a passivation layer on the wafer. The passivation layer should protect the device layers underneath from bulk micromachining process, and electrically insulate them during the insitu measurements in liquid media for application. In addition, it has to be deposited at a lower temperature to avoid introducing stress inside the structures underneath, and it should be, preferably, done in the facilities available here in Auburn University. To achieve those goals, a few materials had been tested: sputtered silicon oxide in both neutral (Ar only) and oxygen plasma environments, reactively sputtered silicon nitride and sputtered silicon carbide. Also, one of the group members had deposited and showed application of DLC film for the passivation layer [44]. The problem with the DLC film is that it has to be deposited in Argonne National Laboratories, not in the facilities available on campus. Also, as the DLC film is etched in O_2 plasma, which oxidizes Cr, and subsequently the exposed metal layer delaminates from the device structure during bulk micromachining process.

Other films were investigated in campus facilities. At first, silicon oxide film was sputtered using a SiO_2 target at $5X10^{-6}$ torr base pressure with 25 sccm of Ar flow, 350 watts power and a sputter pressure of 5.3 mtorr. The resulting film could not protect the polysilicon layers underneath against the bulk micromachining process with KOH etch solution, as seen in Figure 36. Then, the oxide film was sputtered while using 5 sccm of O_2 with both 20 and 25 sccm of Ar gas flow rates, and $1X10^{-6}$ torr base pressure, 100 watts of power and sputter pressures of 5.1 and 5.3 mtorr respectively. The results were the same; they could not protect the piezoresistors either, as seen in Figure 37. Then sputtered silicon nitride film was investigated. It was deposited by reactively sputtering silicon in the presence of nitrogen in the plasma. This time Si target was used, with a base pressure of $1X10^{-6}$ torr, 100 watts of power, 7 sccm of N_2 gas with 18 sccm of Ar gas and a sputter pressure of 5.5 mtorr. The resulting passivation layer

77
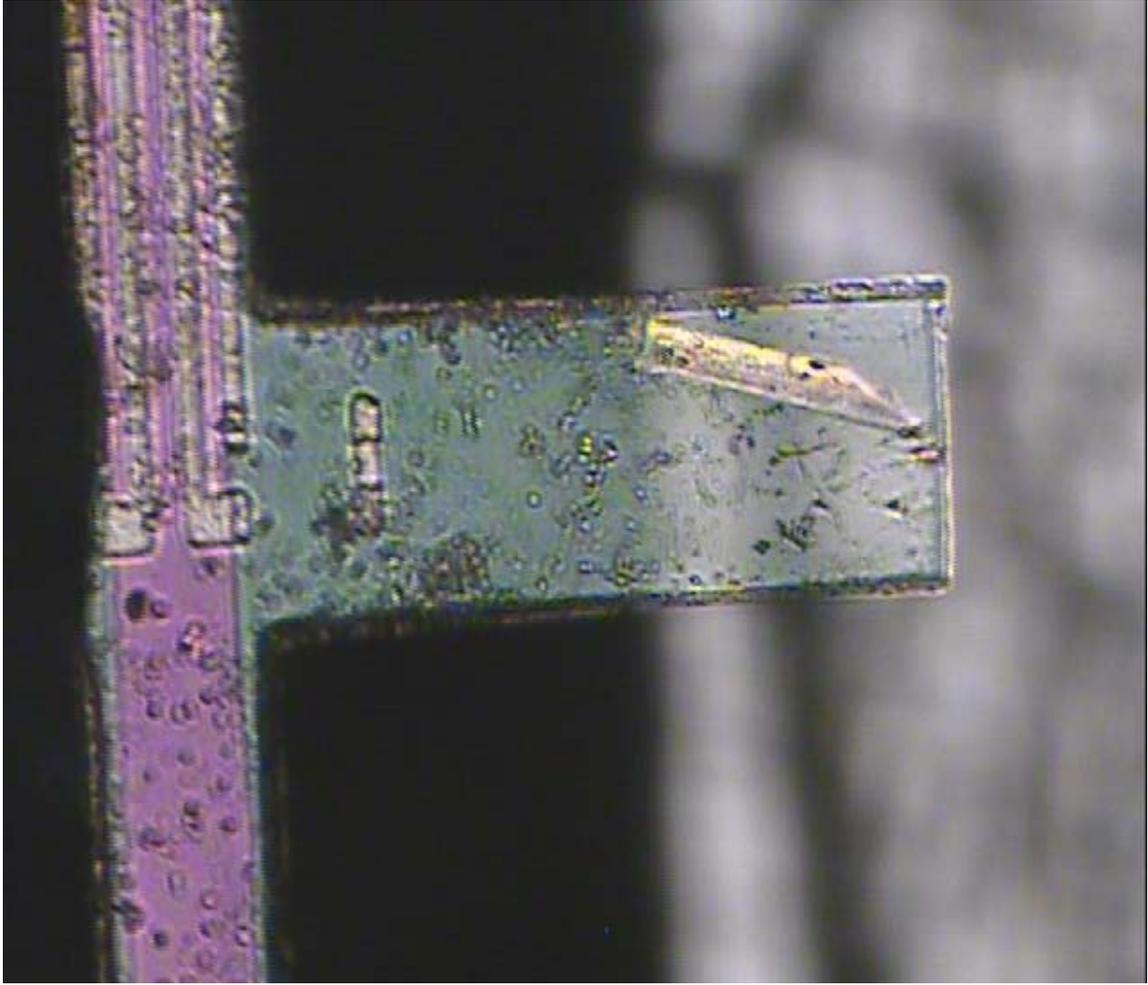
Figure 36: Picture of a cantilever beam structure with sputtered oxide as the passivation layer;

after exposing it to KOH solution.
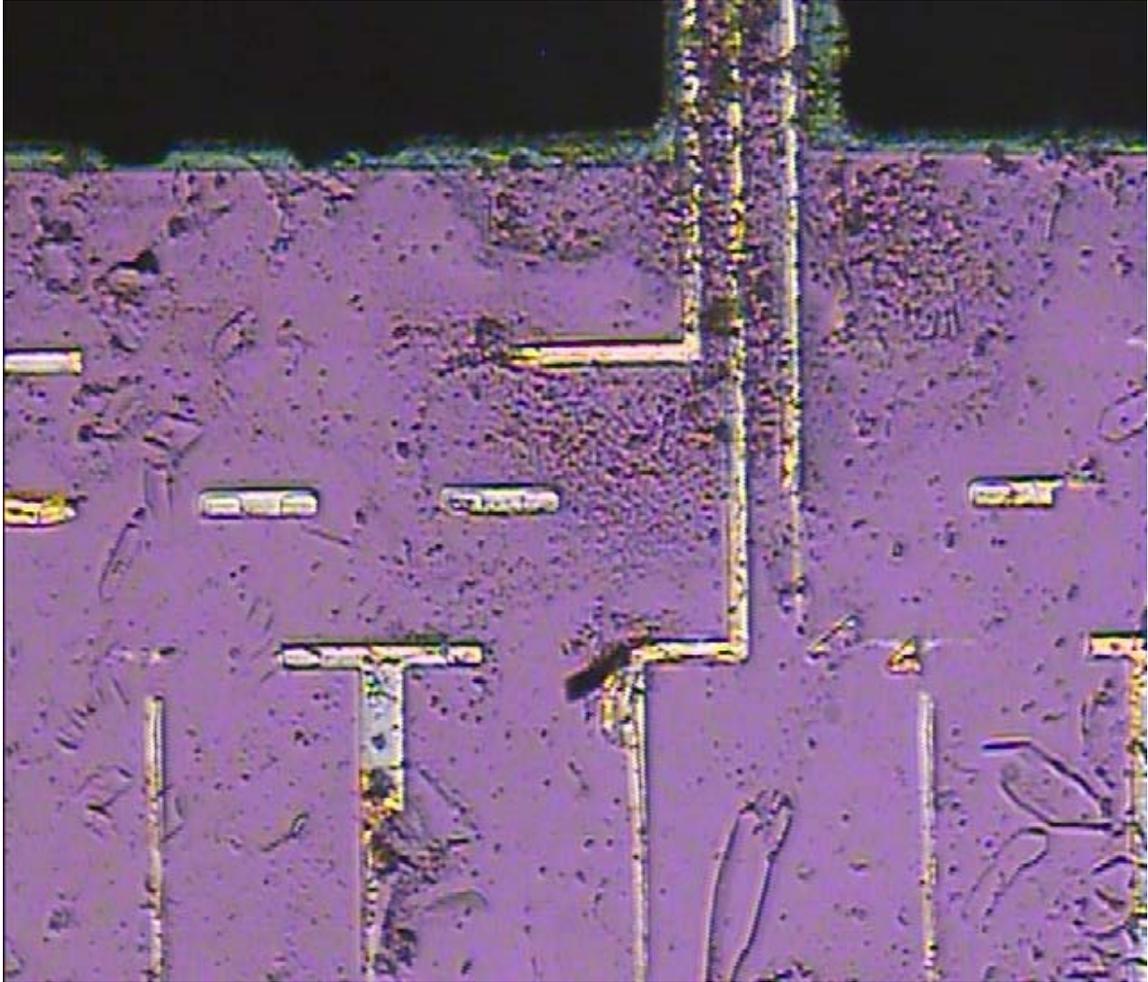
Figure 37: Picture of the piezoresistors on a device with sputtered oxide as the passivation layer; after exposing it to KOH solution.
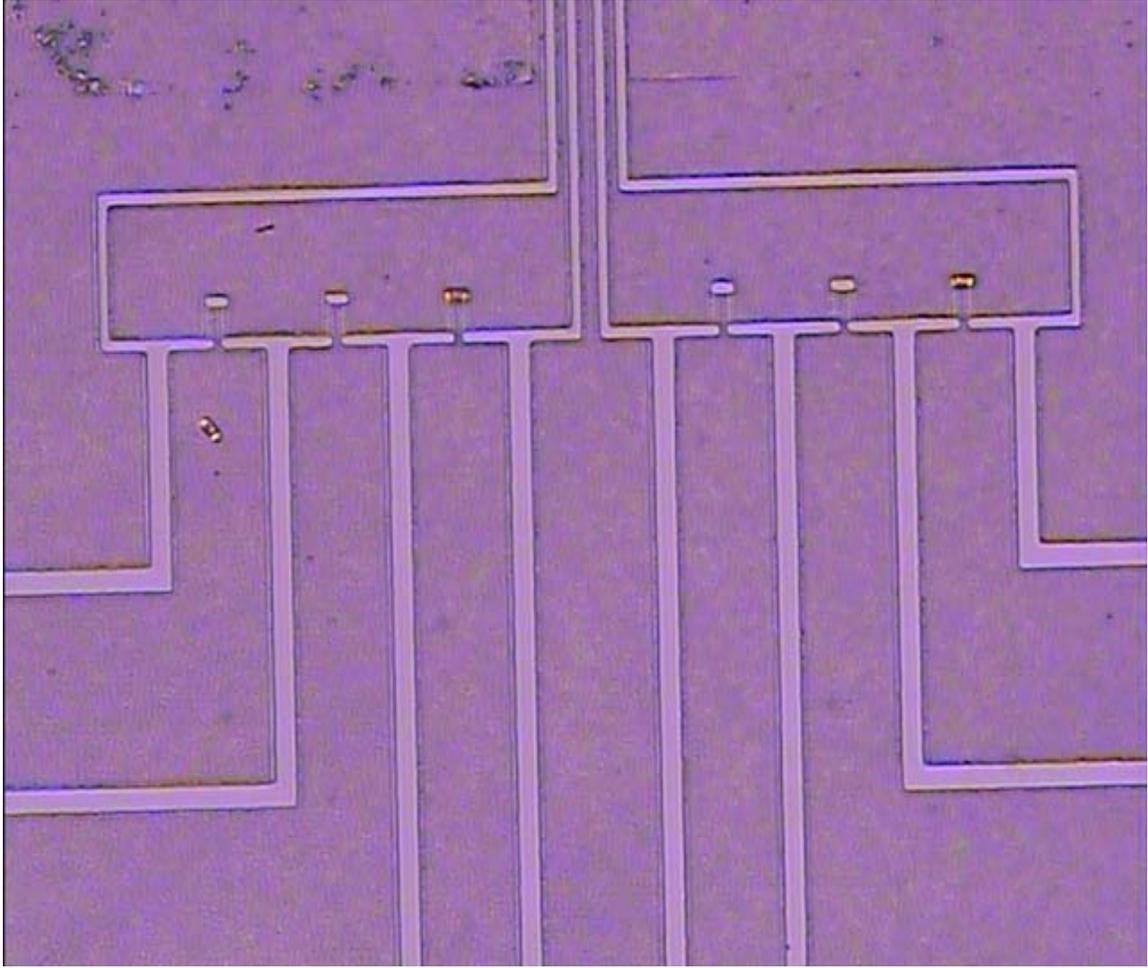
Figure 38: Picture of the piezoresistors on a device with reactively sputtered nitride as the passivation layer; after exposing it to KOH solution.

acted the same way as in cases of the oxide layers. Figure 36 through 38 show the pictures of the devices with these trial passivation layers, after exposing them to the bulk micromachining process of KOH etching. Although the reactively sputtered nitride layer performed better than the oxide layers, it failed to protect the polysilicon layer underneath.

Finally, this problem was solved with sputtered SiC layer, which held up quite well and protected the structures underneath against the KOH etching solution. The SiC layer is deposited at $5X10^{-7}$ torr pressure, 150 watts of power, 25 sccm Ar gas flow and 5.2 mtorr of sputter pressure. The resulting passivation layer survived 6 hours of KOH (30 wt/wt %) etch at 65°C to release the cantilever structure. Thus, the SiC layer, which is sputtered from a SiC target, was chosen as the passivation layer for the devices.

Before and after sputtering of the SiC film, the wafer had to go through usual cleaning, drying, and dehydration bake processes without O_2 plasma cleaning as before. After that, to define the actual cantilever beam structure and making openings for the metal pads for both electrical connections and sensing pads for testing, the SiC layer needed to be patterned and etched. In the beginning AZ5214 positive photoresist was used as the etching mask. The carbide and the nitride etching recipes in Deep Reactive Ion Etching (DRIE) system contain oxygen in them to remove the polymer by-product; the gas chemistry attacks the photoresist during these processes. As the carbide layer had to be thick enough for the step coverage of the underneath device layers, the photoresist did not survive all the way through for the etching process. When these samples were micromachined in KOH or TMAH, they did not survive the etching process, as evident from the SEM pictures in Figures 39 and 40. As the photoresist got etched away, thinning of the SiC layer occurred. When these devices went through the bulk micromachining process, the passivation layer failed to protect the polysilicon layers underneath.

The carbide layer was approximately 600 nm thick as sputtered, twice the total thickness of the polysilicon and the metal layers combined. Ensuring good enough step coverage for the layers underneath. As re-patterning was not feasible either, for the small features like 2.5 to 4 μm, alternative etching mask was investigated. As Al can be etched in potassium borates based developers such as AZ400K, it was investigated as the etching mask for etching both carbide and nitride films together in the Advanced Oxide Etcher (AOE) system. As the passivation layer mask was made for the positive photoresist, to use the same mask to define the Al layer as the etching mask, defined through lift-off technique, reverse patterning of the photoresist needed to be done. In case of reverse patterning, AZ5214E IR photoresist performs better than the regular AZ5214E one. Here, the IR stands for image reversal. At first, the wafer was spun coated with this photoresist following the same procedures as the regular one, and then soft baked at 90°C for 2 minutes. After that, it was exposed in UV light for 5 seconds, while using the 3rd mask in the mask aligner. Then, a reversal bake was performed at 110°C for 2 minutes, and then allowed to cool down. After it was cooled down, the wafer was flood exposed for 1 minute, and then developed in AZ400K developer using 1:4 ratio of DI-H$_2$O solution for about 15 seconds. Al was deposited on the wafer in the E-beam system with 2 minutes of ion cleaning performed right before the deposition. The Al deposition process was performed at a base pressure of less than 3X10^{-6} torr, with 9.75 kilovolts of voltage and 0.141 amps of current. After deposition the wafer was put in an ultrasonic bath, while submerged in acetone to define the etching mask through lift-off technique.
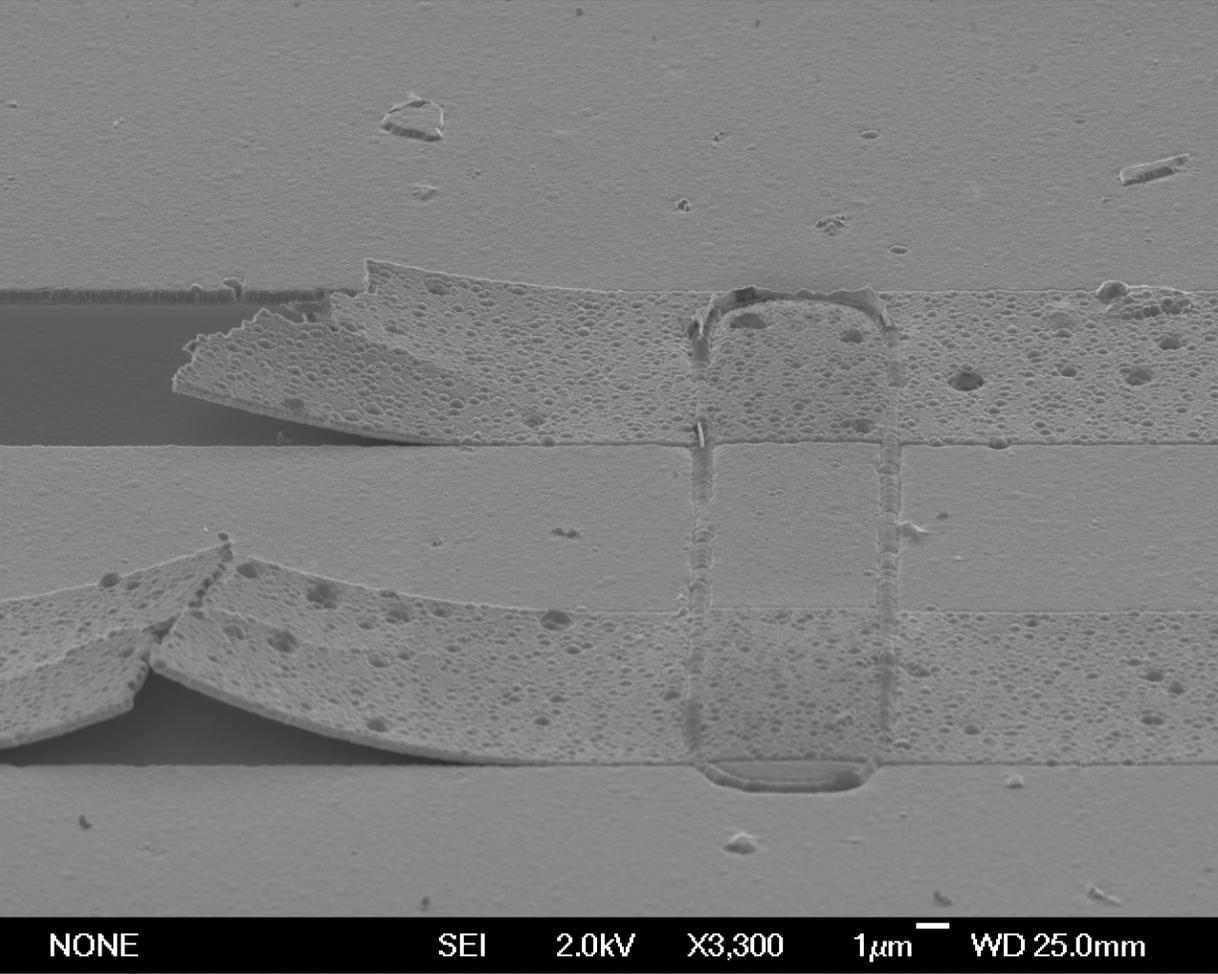
Figure 39: SEM image showing polysilicon layers were attacked during KOH etch, due to the

thinning of SiC layer when regular PR is used as the etch mask for the DRIE process.
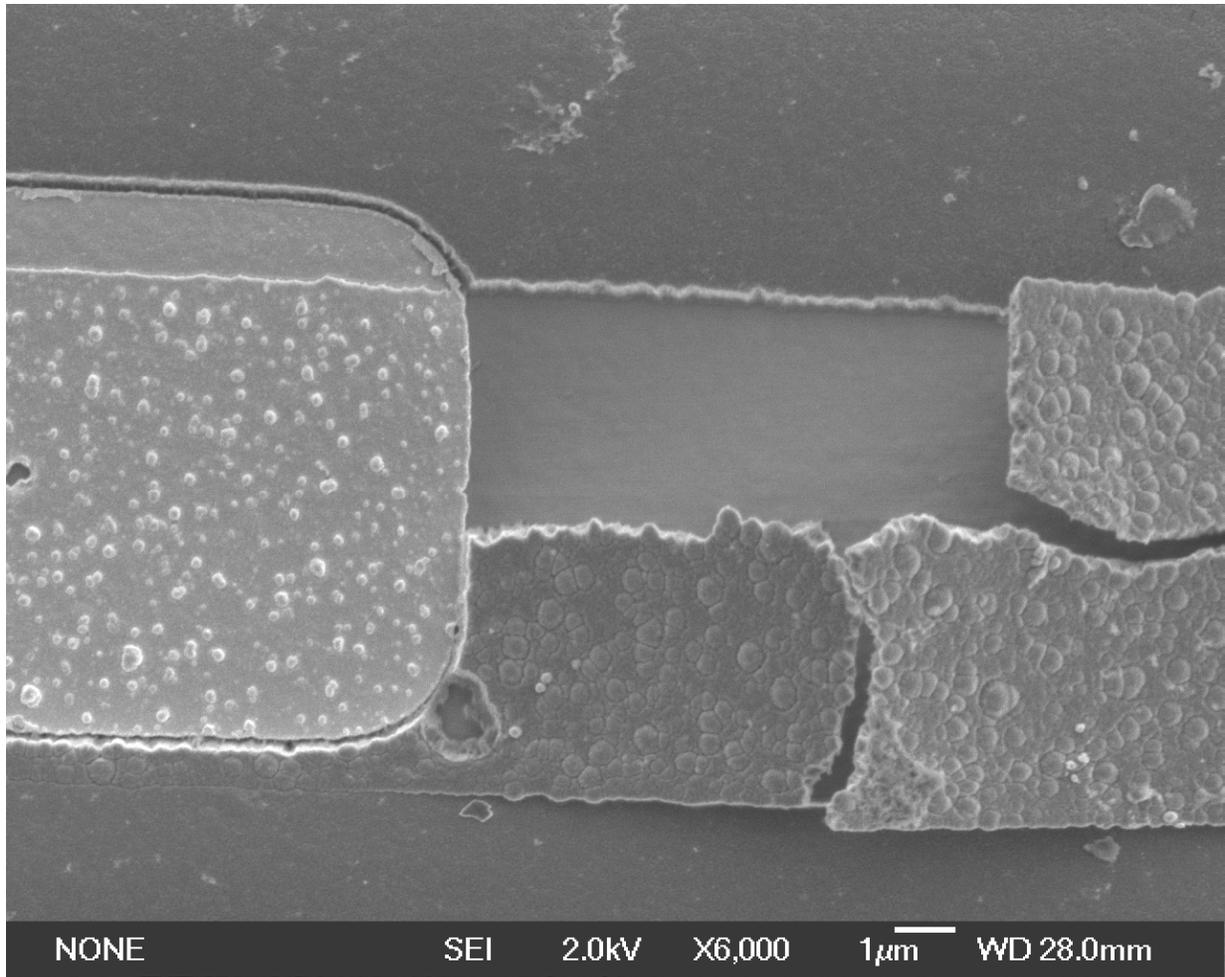
Figure 40: A close up SEM image, showing piezoresistor etched away during KOH etching due to the thinning of SiC layer when regular PR is used as the etch mask for the DRIE process.

The carbide and the nitride layers were etched in the AOE system from the STS, using 30 sccm of CF_4 and 3 sccm of O_2 gas. The base pressure for the process was 0.5 mtorr with 600 watts in the magnetic coil and 75 watts in the platen generator. It takes approximately 15 minutes to etch through the carbide and the bottom nitride layers. In the beginning, the etching was performed at cycles lasting from 1 minute to a few minutes at a time. After the etching was done, the resistances measured between the exposed metal pads showed a Schottky type contact while the resistances measured right after depositing metal pads, showed an ohmic contact. It was suspected that the local temperatures on the surface was reaching high enough to oxidize Cr, although the cooling water temperature was kept at 10°C. So, to investigate this hypothesis, etching was performed in 15 seconds long cycles. By using these short cycles, it was possible to conserve the ohmic contact during the etching process. Plots of resistance measurements for both longer and shorter 15 seconds etching cycles are attached in Figures 41 and 42, respectively. These measurements were performed by a Semiconductor Parameter Analyzer. After etching through the carbide and the nitride layers, the Al etching mask is removed in 2:1 ratio DI-H_2O solution of AZ400K developer.

At first, the bulk micromachining of Si was done in KOH etching solution, which always etched quite well and released the cantilever structures without much of a difficulty. However, after the etching process the resistance measurements always showed 3 orders of magnitude of larger resistances with no ohmic contact, regardless of the concentration and the temperature (30°C, 60°C, 65°C or 80°C) of the solution. Figure 43 shows the I-V characteristic curves for the devices after KOH etch. Therefore, the use of other etching solutions was investigated. The popular alternative method is to use tetramethylammonium hydroxide or TMAH solution. A recipe consisting of 8.33% of TMAH solution was tried to etch Si to release the cantilever
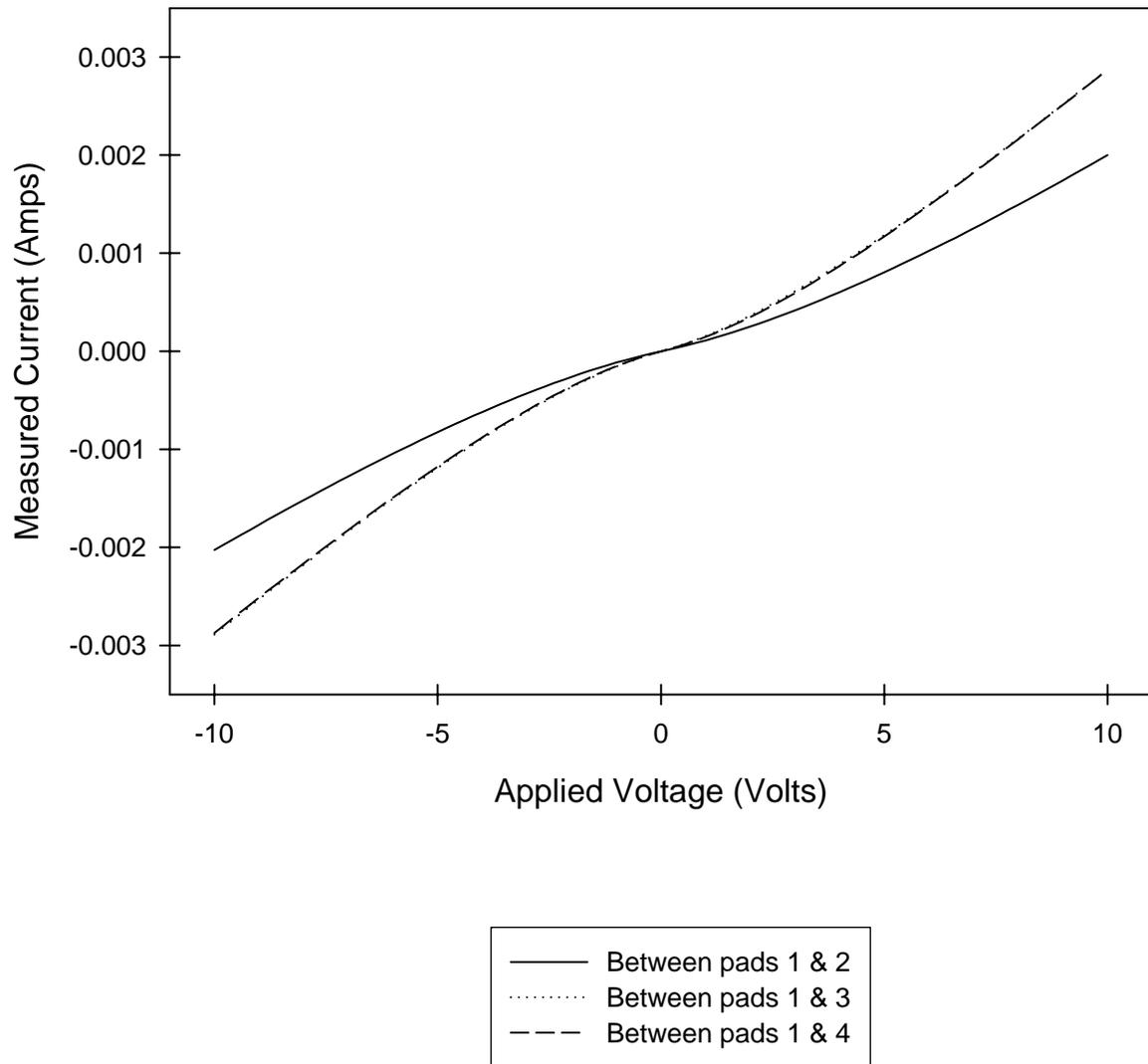
Figure 41: Resistance measurement after etching SiC & Si_xN_y in the AOE system, without specifying time for the etching cycles.
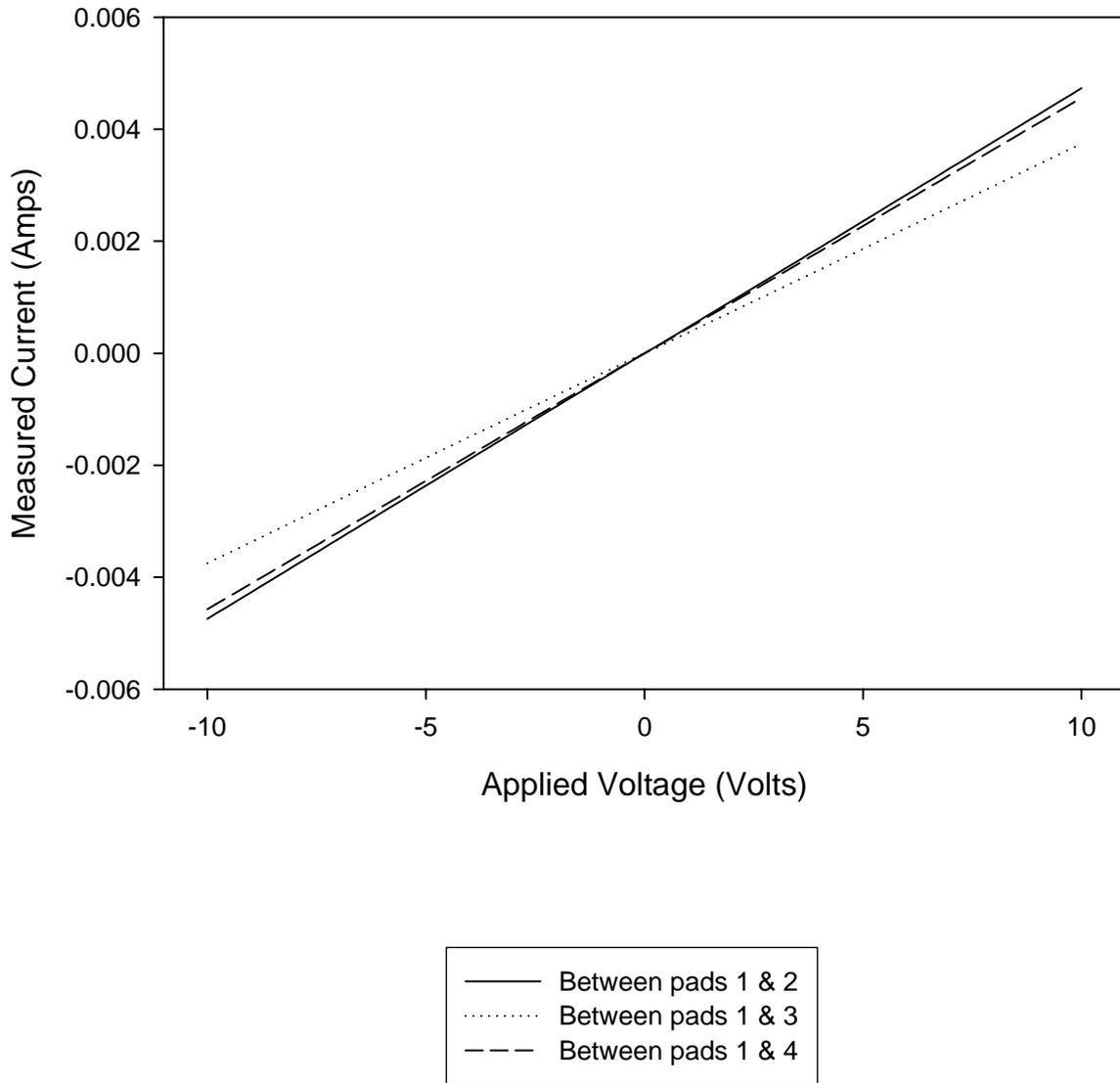
Figure 42: Resistance measurement after etching SiC & Si_xN_y in the AOE system, with specific

15 seconds etching cycles.

structures. In this recipe, to reduce the hillock structure formations on the etched Si surface, and to make the surface smoother, ammonium peroxydisulfate (APOD), an oxidizing agent, was added every 20 minutes at a concentration level of 0.1 wt/wt % of the total solution. This recipe also increased the resistances 3 orders of magnitude, as shown in the plots attached in Figure 44.

A few TMAH etch recipes have been investigated and published [45-48] over recent years for post CMOS compatible bulk micromachining techniques. In one of the techniques described by Zhang et al. [48], a 5 wt% of TMAH solution is mixed with 1.6 wt % of Si powder and 0.5% of APOD, and heated up to about 80°C for micromachining of Si. This solution enables etching of Si through a pH controlled method without attacking the piezoresistive polysilicon or the metal-poly junction integrated inside the device structures. The I-V characteristic curves from the devices that survived during the bulk micromachining process performed on them, using the pH controlled TMAH etch recipe, is attached in Figure 45. After the cantilevers were released, the devices were cleaned and dried in isopropanol. The complete process flow is listed in the Flow Chart 6.1 which is attached at the end of this chapter. Figure 46 and 47 shows SEM pictures of the fabricated devices. Here, from the SEM images, it can be seen that the cantilever beams were bent downwards. This may be due to the fact that the LPCVD system and its Mass Flow Controllers (MFCs) had not been calibrated. Thus, the gas ratio was not perfectly 5:1 ratio during the silicon nitride deposition process. Another plausible explanation can be the stress induced from the repeated thermal cycling the structures experienced from the rest of the processes after deposition. For the resonance mode application, as this should not effect the measurements, it was not of much concern for this project.
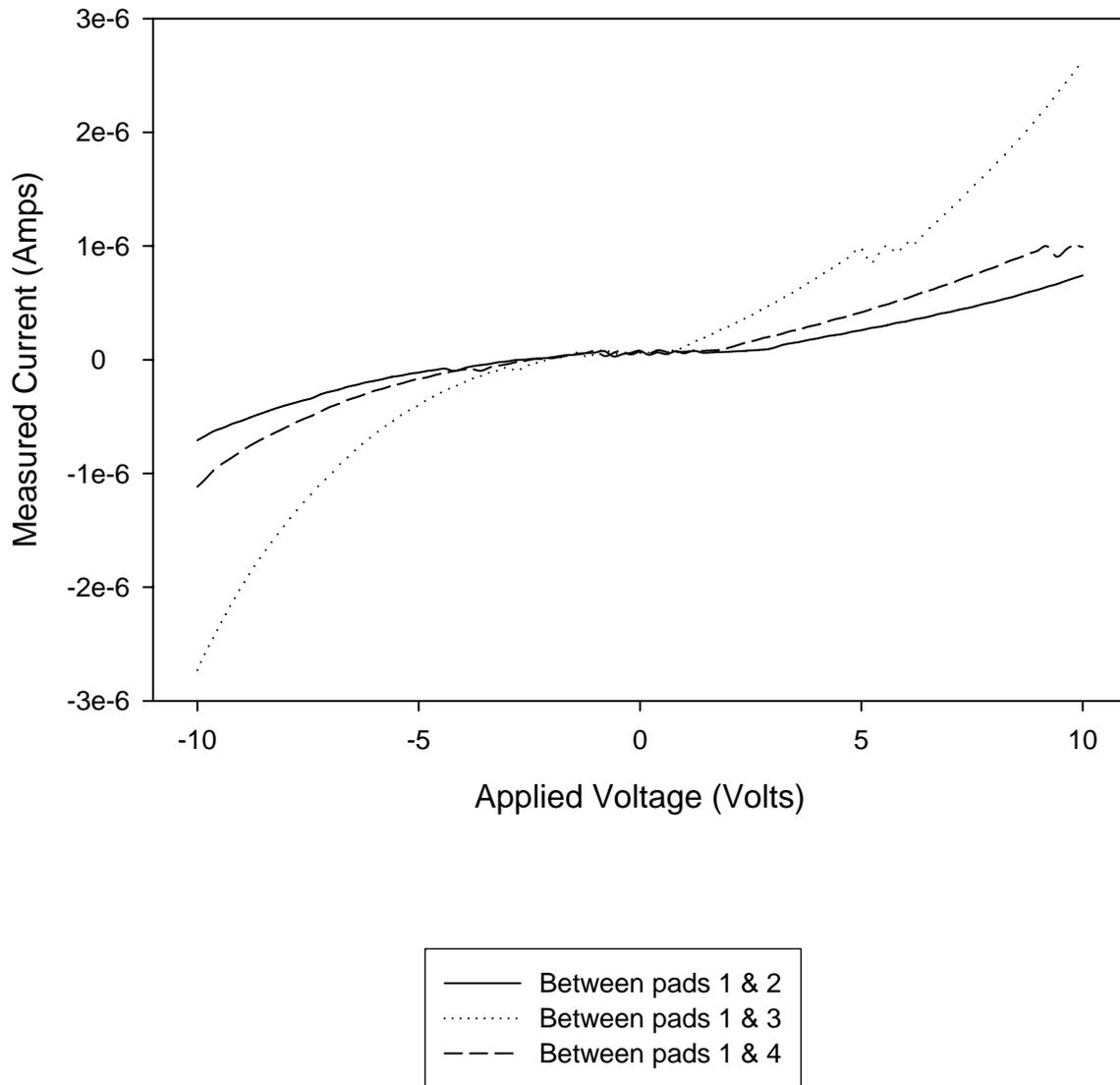
Figure 43: Resistance measurement after etching Si in KOH for bulk micromachining of the
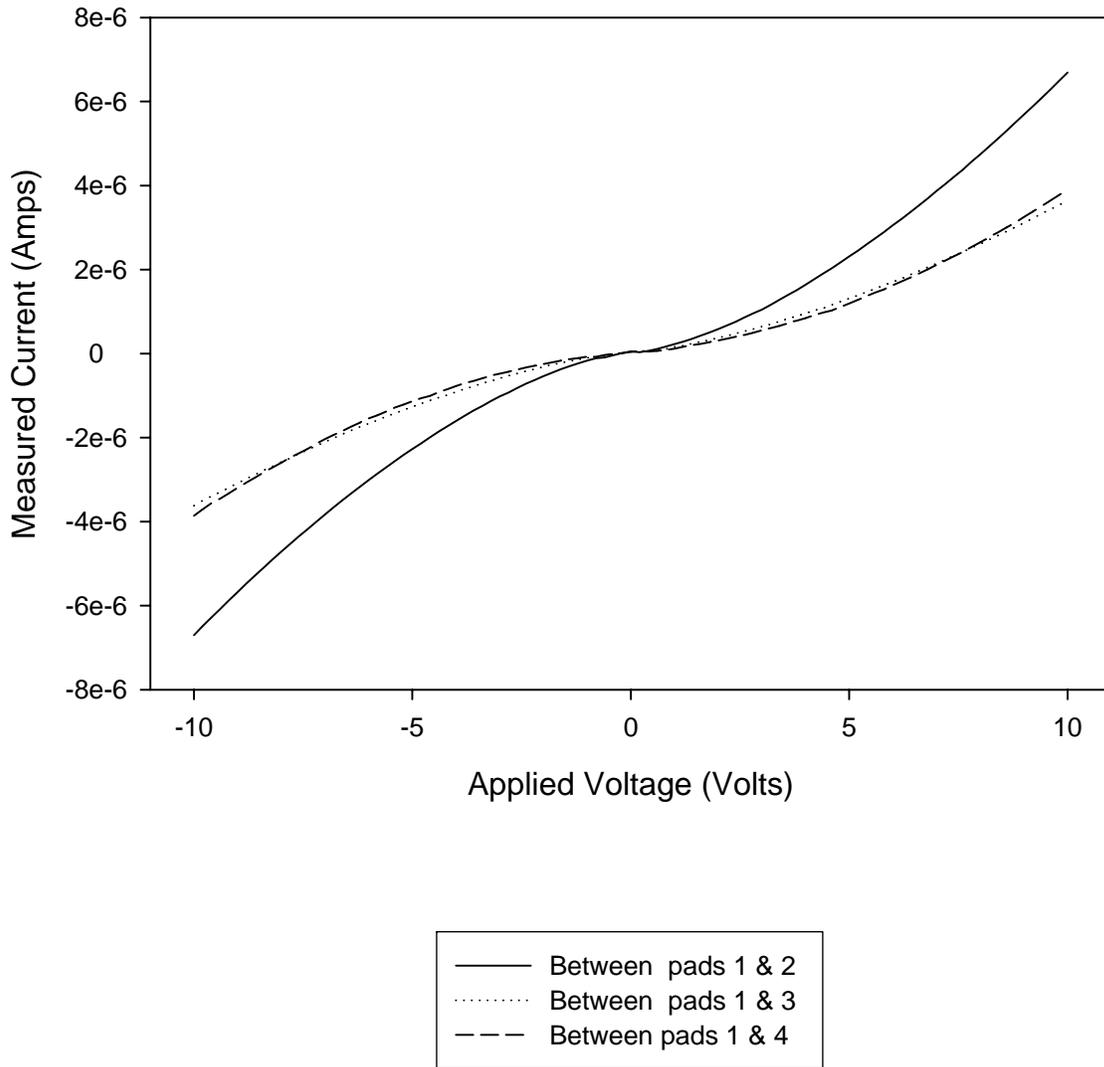
MEMS device.

Figure 44: Resistance measurement after etching Si in TMAH for bulk micromachining of the

MEMS device using conventional recipe.
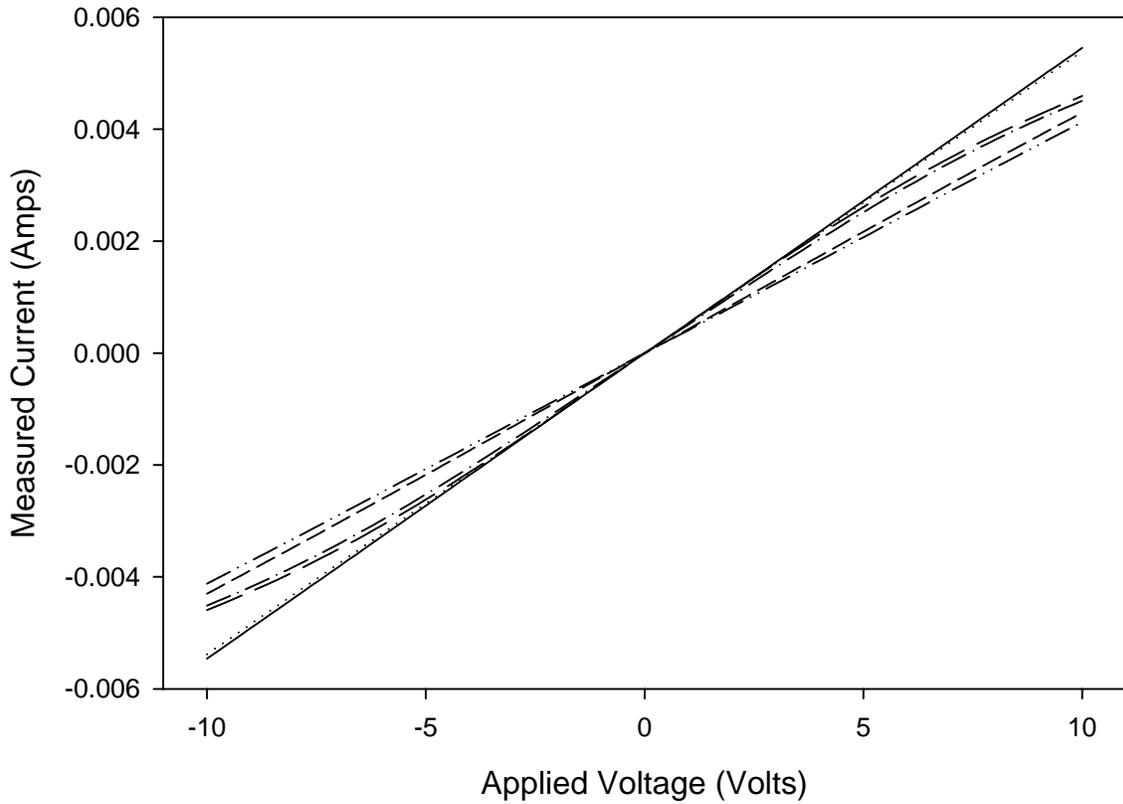
Figure 45: Resistance measurement after etching Si in TMAH for bulk micromachining of the

MEMS device using pH controlled recipe.
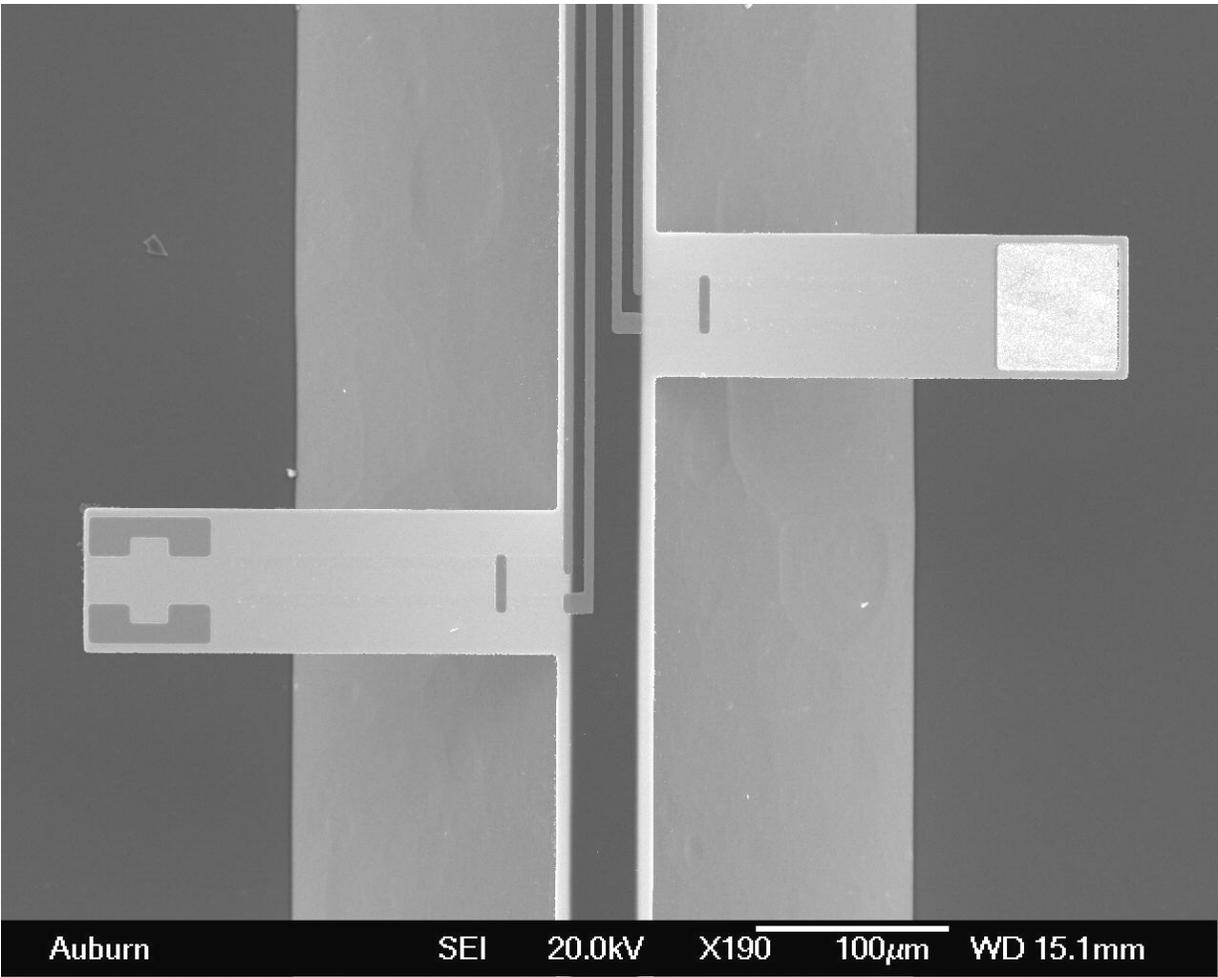
Figure 46: SEM images showing microcantilevers.
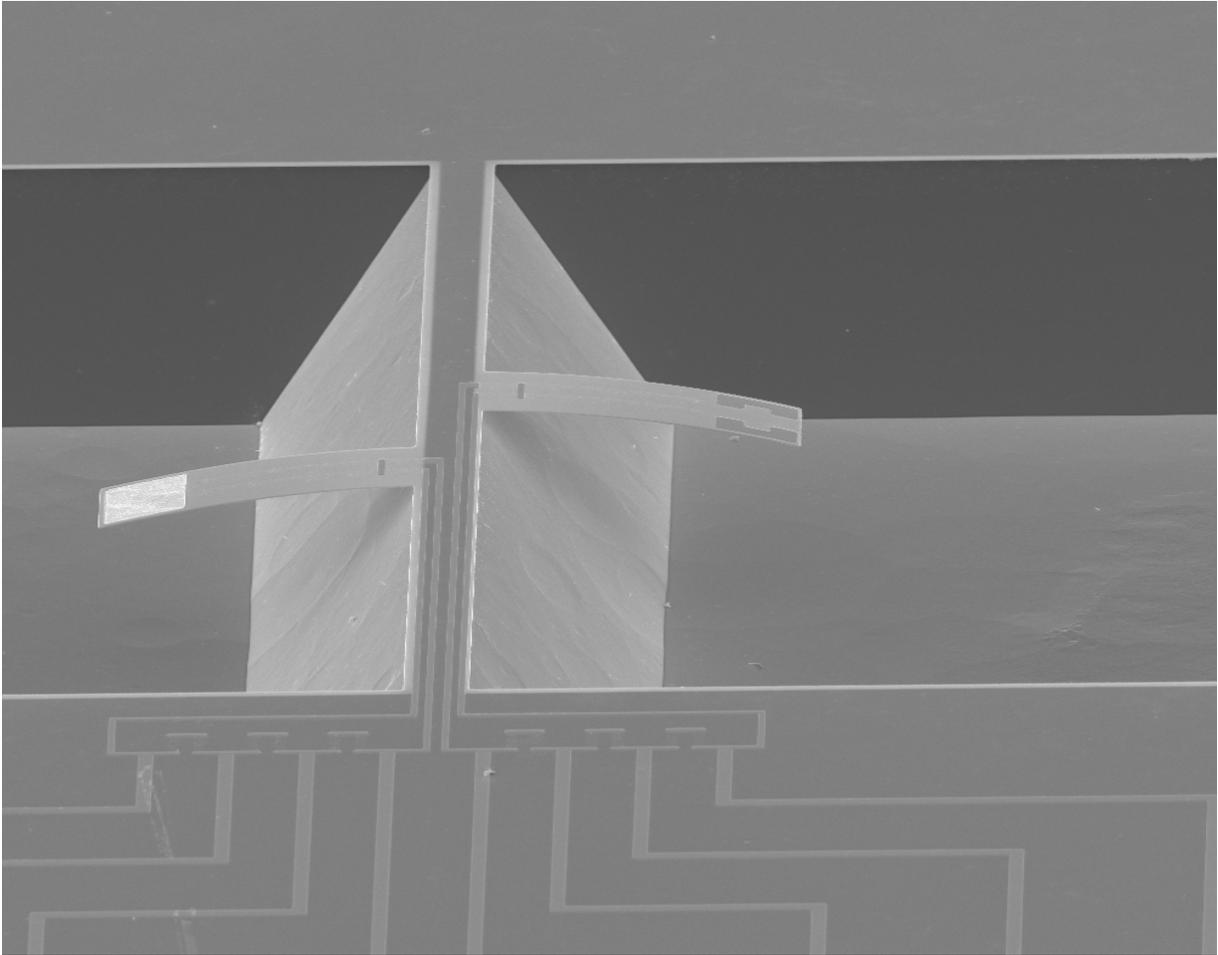
Figure 47: SEM images showing microcantilevers with the Wheatstone bridge structures.

Flow Chart 6.1: Microfabrication process flow chart for the microcantilever MEMS devices
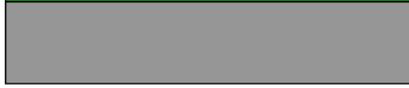
Step1: Take bare single side polished (100) oriented Si wafer.

Step 2: Deposit Si_xN_y on it in the LPCVD system, using DCS ($SiCl_2H_2$) & NH_3 gases at 850^OC.
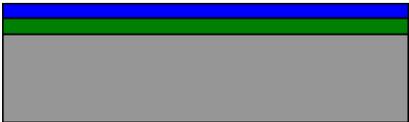
Step 3: Deposit poly-Si at 650^OC in LPCVD, using Silane (SiH_4) gas.

Step 4: Spin coat with phosphorous diffusant (phosphosilicate glass), prebake @ 150^OC and then drive in @ 1000^OC.

Step 5: Deglaze the phosphosilicate glass in 10:1 = DI-H_2O: HF solution.

Step 6: Put in HMDS environment, spin coat with +ve photoresist (AZ5214) and soft-bake @ 105^OC.

Step 7: Expose in UV light and develop in potassium borates based developer (AZ400K), and hard-bake @ 120^OC.
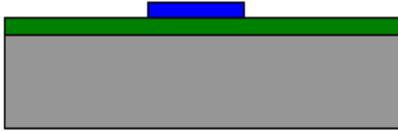
Step 8: DRI Etch of poly-silicon in ASE system, using SF_6 & O_2 gas.
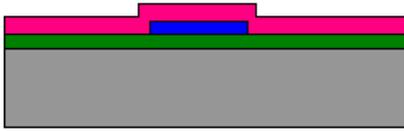
Step 9: Put in HMDS environment, spin coat with +ve photoresist (AZ5214) and soft-bake @ 105^OC.
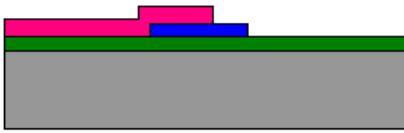
Step 10: Expose in UV light and develop in AZ400K developer.
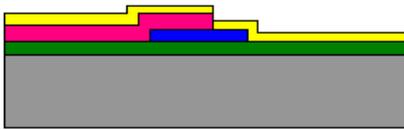
Step 11: Ion clean and deposit Cr-Au-Cr layers in the E-beam system.
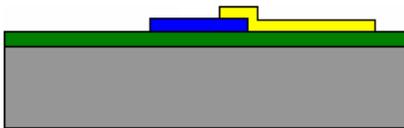
Step 12: Put the wafer in ultrasonic bath, while submerged in acetone to define metal pads by the lift-off technique.
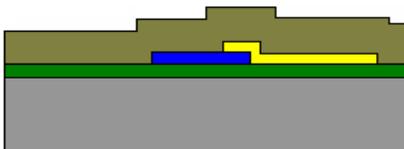
Step 13: Sputter SiC in the Sputtering system.
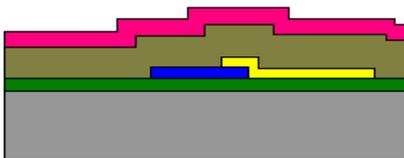
Step 14: Put in HMDS environment, spin coat with +ve photoresist (AZ5214 IR) and soft-bake @ 90^OC.
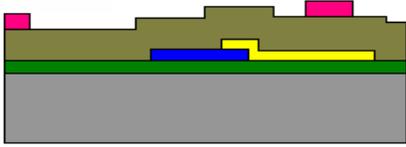
Step 15: Expose in UV light, reverse bake @ 105^OC, flood expose in UV light & develop in AZ400K developer for reverse patterning.
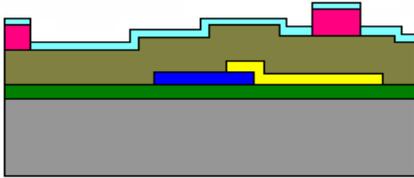
Step 16: Deposit Al in the E-beam system.
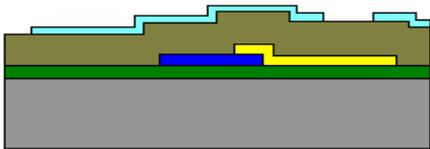
Step 17: Put the wafer in ultrasonic bath, while submerged in acetone to define etching mask by lift-off technique.
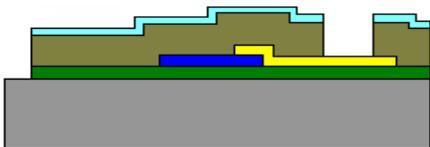
Step 18: DRI Etch of SiC & Si_xN_y in the AOE system, using CF_4 & O_2.
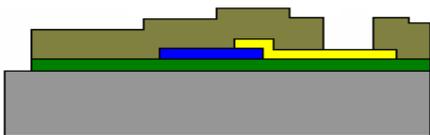
Step 19: Strip-off Al etch mask with potassium Borates based developer AZ400K.
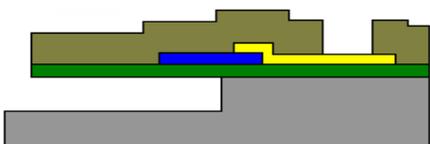
Step 20: Etch Si in TMAH solution, using a pH controlled recipe, and dry them in IPA to release the cantilever beam structure.

CHAPTER 7

PIEZORESISTIVE MEASUREMENT OF THE MEMS DEVICES

At first the microcantilever beams on the MEMS devices were characterized by optically measuring the resonant frequency of the beams. To accomplish that task the photo detector of the JEOL SPM 5200 system was used. The laser of the AFM system was shone on the tip of the cantilever beam, and the reflected signal was processed using the photodetector of the system. The signal output from the system was then fed to the Tektronix TDS 3014B Digital Oscilloscope. The device was mounted on a modified sample holder for the AFM system, which had a spring loaded clamp to hold the sample on top of the piezoelectric ceramics bought from the Fuji Ceramics Corporation. The sample holder was made out of aluminum. The actuator is of thickness mode with a resonant frequency of 1.2 MHz. The actuator was actuated by a sinusoidal signal from a function generator Agilent 33220A through the wideband amplifier Model 7600 from Krohn-Hite Corporation. The schematic diagram of the test setup is shown in Figure 48.

Since the structure was vibrated with a signal from the function generator, the output signal showed a response at all times, at the same frequency as the input frequency of the function generator. This output signal was traced while manually scanning the input signal through a range of frequencies. At the resonant frequency of the microcantilever beam structure
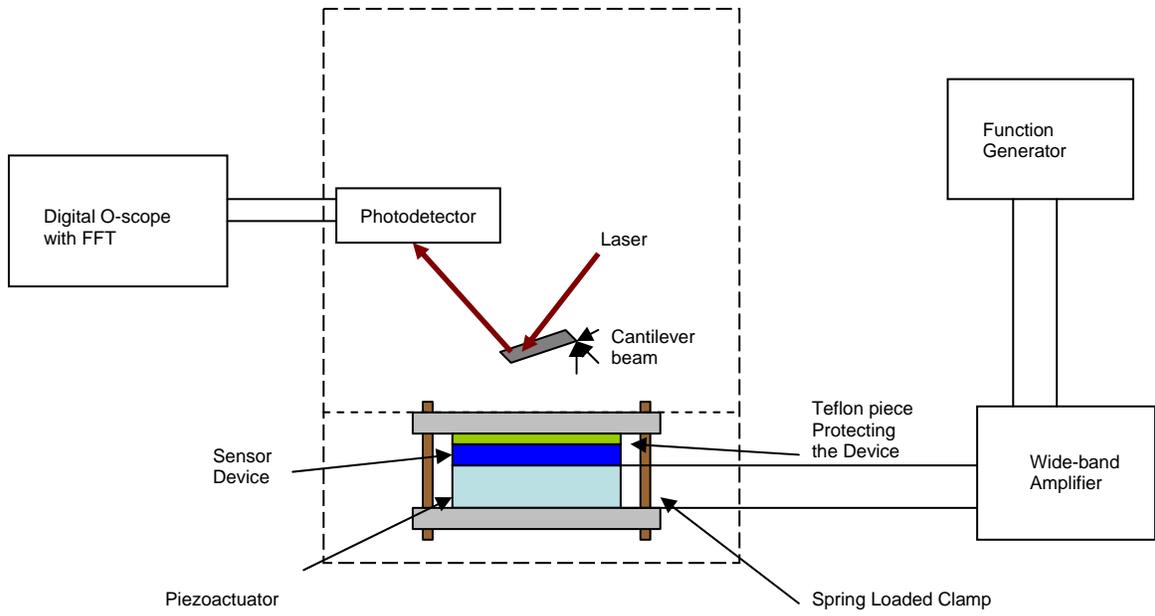
Figure 48: Schematic diagram showing test setup for optical measurement of the resonant

frequency of the microcantilever MEMS device.

OPTICAL FREQUENCY MEASUREMENT
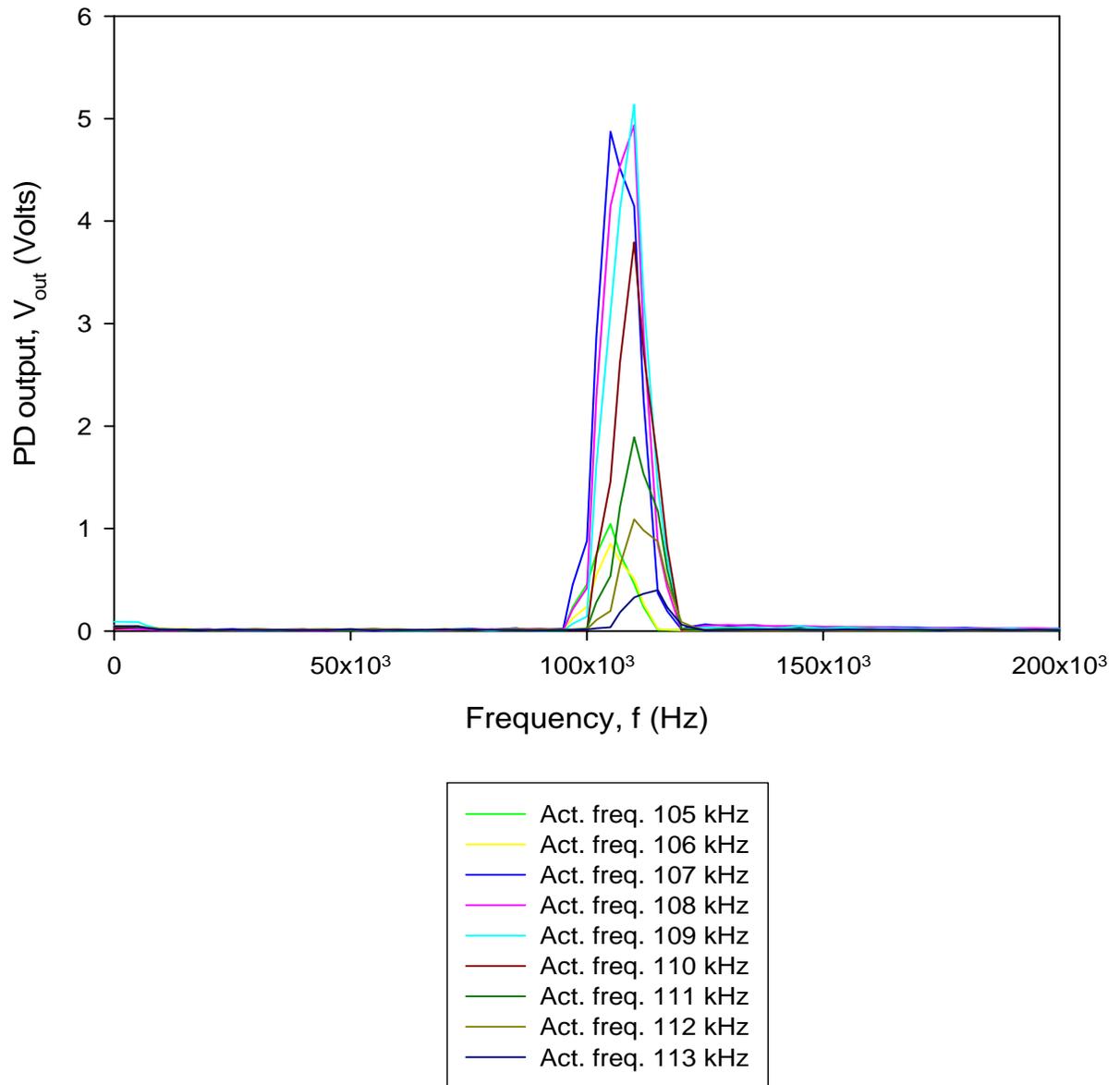
Figure 49: Resonant Frequency characterization of a 150μ length microcantilever MEMS device using the AFM photodetector.

OPTICAL FREQUENCY MEASUREMENT
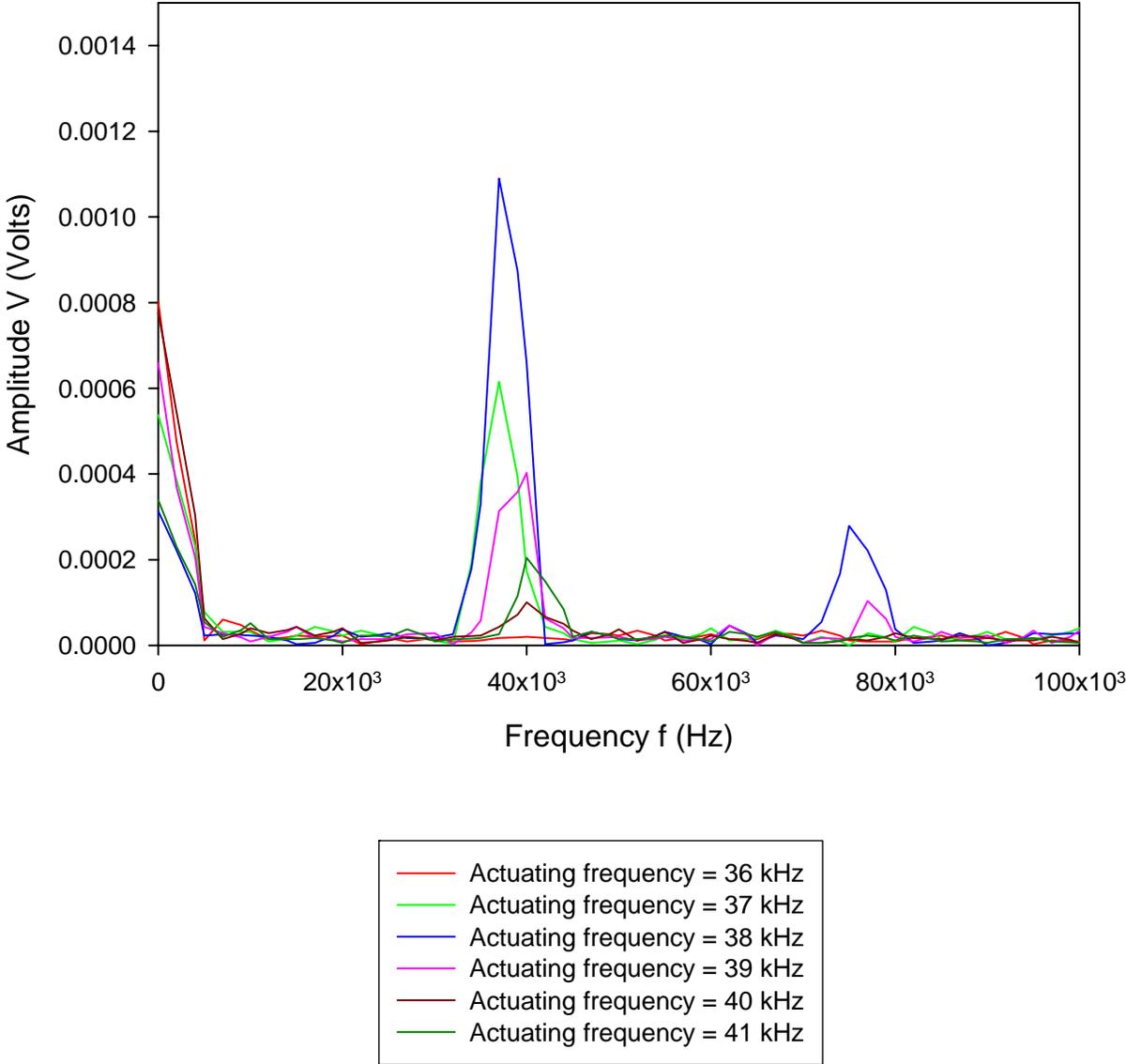
Figure 50: Resonant Frequency characterization of a 250µ length microcantilever MEMS device using the AFM photodetector.

the output signal showed much higher response than the other frequencies that the input signal was operated at. This can be seen in the frequency spectrum plots in Figures 49 and 50, which are the responses obtained for 150 μm and 250 μm length rectangular shaped microcantilever beams. From these plots, it can be seen that the output response rose sharply around 109 kHz for the 150 μm length device, and 38 kHz for the 250 μm length device. It was observed that the output signals dropped significantly from those responses when the input signals were moved away from those specific frequencies. Thus, the resonant frequency of the 150 μm length device is close to 109 kHz, and the resonant frequency of the 250 μm length device is close to 38 kHz. Since the resolution of the FFT function of the digital oscilloscope is not that great, these values should be considered as approximations only.

Once the device had been characterized by the optical measurements, the resonant frequency was measured by the piezoresistive Wheatstone bridge. The piezoactuator that was used requires a quite high AC voltage to operate, in the range of 80 to 100 Volts. Since this actuator was sitting right underneath the MEMS device and the output signal is supposed to be very small, in the range of microvolts, phase-lock loop was required for the measurement. Figure 51 shows the schematic diagram of the test setup for the frequency measurement through the piezoresistive Wheatstone bridge. At first, SR844 – 200 MHz RF Lock-in Amplifier from the Stanford Research Systems was used for the piezoresistive measurement of the devices. A phase locked system, such as the Lock-in amplifier, synchronizes the input or the reference signal with the output signal that it generates, by comparing their amplitudes at corresponding phases. In this case, the input signal for the SR844 was the output signal from the Wheatstone bridge. The Lock-in amplifier matches the phase of that output with the signal that feeds the wideband amplifier to actuate the piezoactuator. The outputs from the Lock-in amplifier were
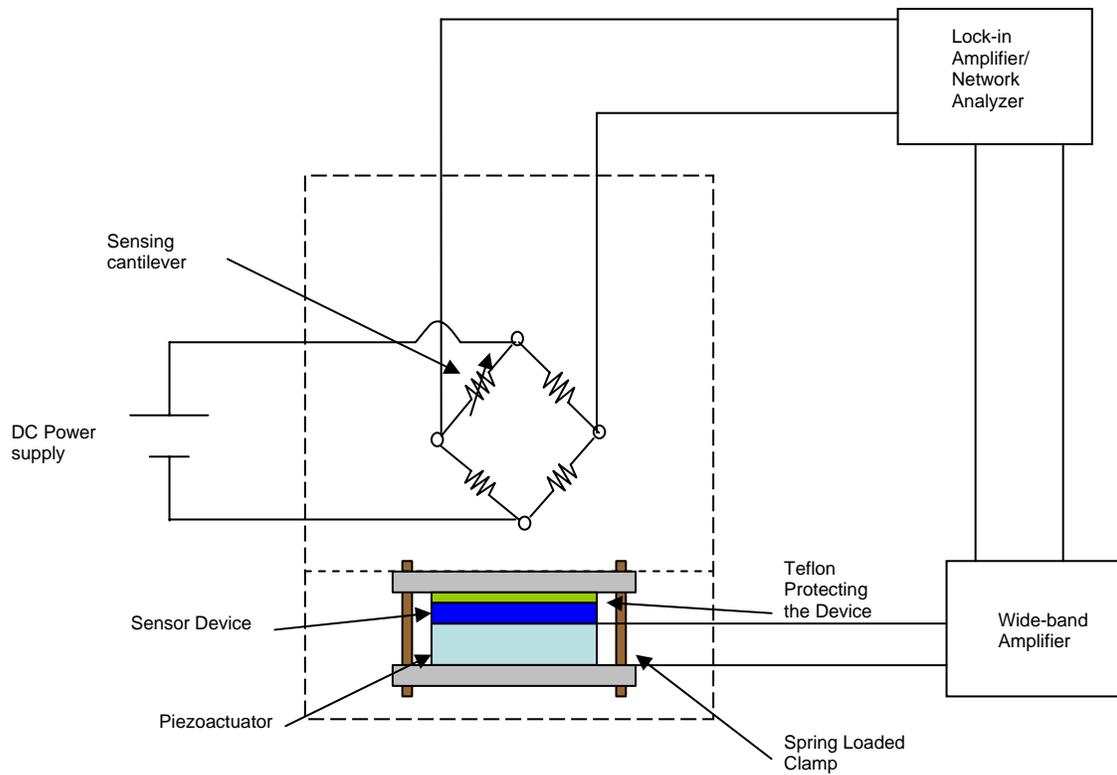
Figure 51: Schematic diagram showing test setup for piezoresistive measurement of the resonant

frequency of the microcantilever MEMS device.

monitored by manually scanning near the range of the resonant frequency obtained by the optical measurements. For the device of 150 μm length microcantilever, it was possible to get a large output signal from the Lock-in amplifier, at 104 kHz. When the input signal was varied from the specific frequency or the phase the output signal dropped significantly.   In case of manual control, the frequency of the input signal could be varied for the SR844 at a step size of about 1 kHz.   But, when the frequency scan was performed automatically and recorded, the resulting frequency spectrum response showed as depicted in Figure 52. From these plots it was seen that the response from the device looked like noise only. But, when the response from the device with an applied DC voltage across the Whetstone bridge was normalized against the response from the device without any voltage applied across the bridge, there was an amplitude difference in the range of 5 to 7 μvolts, approximately. This difference in response does fall in the range of output voltage change expected from the piezoresistors made out of highly doped poly Si.

After that the test setup was modified by replacing the Lock-in amplifier with a Network Analyzer HP 8751A. The frequency spectrum obtained from this setup for the 250 μm length microcantilever device is attached in Figure 53. This response showed its 1st peak at 43.2 kHz. This was very close to the response that was measured by the photodetector. Thus, the MEMS device based on the piezoresistive sensing element worked for the frequency measurements.

FREQUENCY SPECTRUM FROM THE LOCK-IN AMPLIFIER
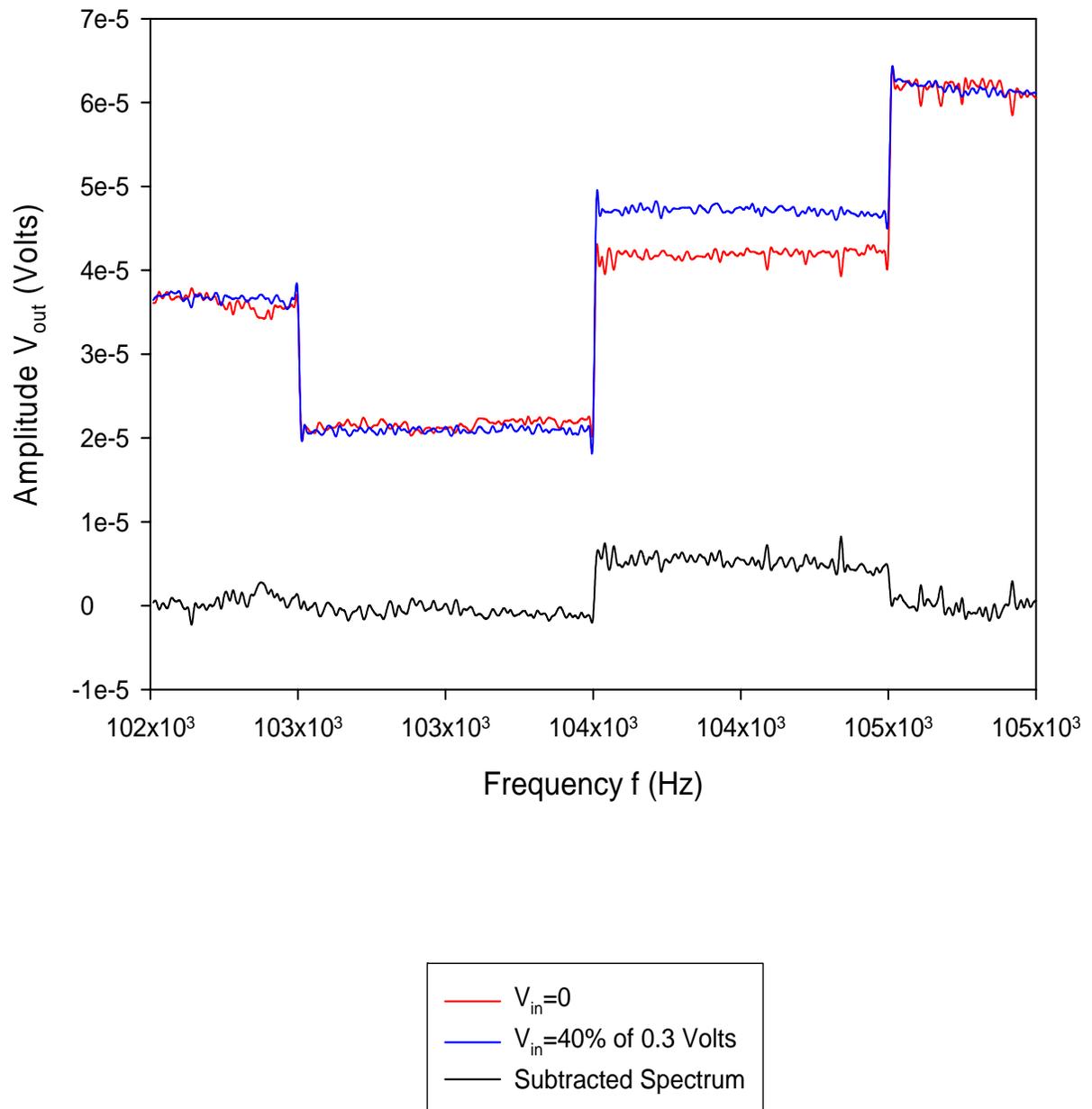
Figure 52: Resonant Frequency Measurement of a 150μ length microcantilever MEMS device using the Lock-in amplifier.

FREQUENCY SPECTRUM FROM THE NETWORK ANALYZER
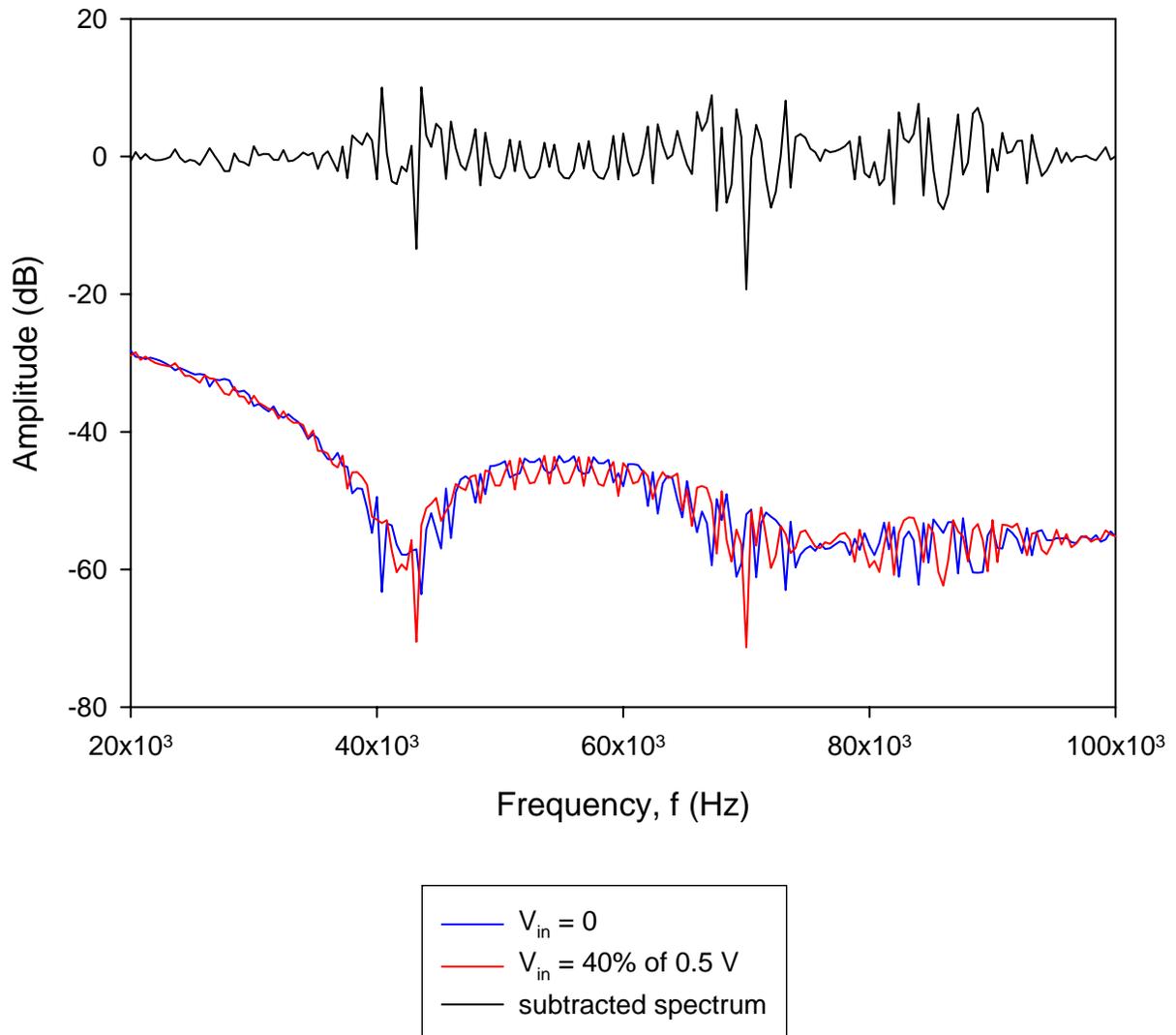
Figure 53: Resonant Frequency Measurement of a 250µ length microcantilever MEMS device using the Network Analyzer.

CHAPTER 8

DISCUSSION AND CONCLUSIONS

In this project geometrical aspects of the microcantilever beam structures were investigated to develop a better performing microcantilever based MEMS device for biosensor application. Different shapes of cantilever beam structures were studied by finite element analysis in ANSYS. From this initial study it was found that the resonant frequency of the cantilever beam structures depends on two parameters. One of them is the area of cross section that is clamped on the fixed end of the cantilever beam. Larger clamped area, in other words the base of the cantilever beam structure, increases the stiffness of the structure. This phenomenon increases the resonant frequency and the corresponding shift in resonant frequency of the structure. The other one is the effective mass acting on the structure, in other words the mass of the structure that is being supported by the beam structure at the clamped end. These phenomena are obvious from the Equation (5). Since the shift in resonant frequency is proportional to the intrinsic resonant frequency of the cantilever beam structure, as seen from the Equation (6), the performance of the cantilever beam in terms of mass sensitivity depends on them.

Now, from this discussion, it was clear that the triangular shaped cantilever structure should offer the best performance in terms of mass sensitivity. The disadvantage associated with the simple triangular shape structure is that they do not offer large enough area at the free end of

the structure, where it has the highest sensitivity in terms of frequency shift, for the sensing pad that is required to capture the target species for biosensor applications. On the other hand, the triangular shape offers more uniform bending stress near the clamped end, which translates into larger signal from the functional or transduction material of the sensor devices.

To combine both of these phenomena, some modified geometries were investigated by FEA simulations done in ANSYS. This geometry offers the advantages of the triangular shape at the clamped end of the structure, while combining a rectangular shape pad area at the free end to overcome the disadvantages associated with the triangular shape. As the FEA results showed promising performance by the modified geometry, in terms of mass sensitivity, it was further studied by fabricating AFM tip cantilever structure for optical measurement. The tips were made of three geometries: the regular rectangular shape, the triangular shape, and the modified geometry. These three geometries namely shape A, F and I were studied by measuring their resonant frequency by the AFM system, and their corresponding shift in resonant frequency due to mass addition. Their performances, in terms of mass sensitivity were characterized and compared with each other.

It was observed that the mass sensitivity of the triangular shape F cantilever structure is almost an order of magnitude higher than the regular rectangular shape A; this was predicted as well by the FEA results. Although the modified shape I did not perform as well as the shape F, it still showed an improvement of more than three times the mass sensitivity of the shape A. These results agreed quite well with the FEA predictions. Since, the triangular shape F does not offer much space for fabricating sensing pad to capture the target species that needs to be detected, the shape I offers a compromise for better performance in term of both of these phenomena. To further investigate its performance, the damping effect on this shape was studied and compared

107

with the rectangular and the triangular shape cantilever structures. The AFM tips were tested at different levels of air pressure, and their corresponding resonant frequencies were measured. The relative resonant frequencies were plotted and compared with each other in chapter 5. Theoretically, since the triangular shape has a smaller area at the free end, it should show a lesser damping effect on its performance than the regular rectangular shape. Based on the same logic, the modified geometry should show an intermediate damping effect between those two geometries, as depicted in the schematic Figure 22.

In reality these geometries did not show any discernable differences in their performances, in terms of relative resonant frequencies as observed from the plots in Figure 29. This was due to the fact that the relative resonant frequencies are highly dependent on the intrinsic frequencies of the structures. Since the intrinsic resonant frequency of the triangular shape is much higher than the rectangular shape, the relative resonant frequency becomes comparable to the rectangular shape as a function of pressure. The modified geometry, also, followed the same trend as the other geometries. The shift in relative resonant frequencies as a function of pressure, due to mass addition can be seen in Figures 30 through 32. Although these plots showed the same trend as the basic structures, they showed a shift in plots as predicted from the previous results listed in chapter 4.

Microcantilever based MEMS devices were fabricated with piezoresistive sensing elements. These devices were characterized by measuring their resonant frequencies optically, and verified by the electronic measurement through the piezoresistors. Since the devices needed to be actuated by using a piezoactuator that needed a very high voltage AC signal, it offered a tremendous challenge to discern the actual output signal from the devices, which is expected to be of a very small scale of microvolts regime. From Figure 52, it can be seen that the scanned

frequency response from the Lock-in amplifier looked like noise that was picked up by the connectors attached to the device for the measurement. But when this response spectrum was normalized against the scanned spectrum, without applying any voltage across the Wheatstone bridge, there was an amplitude difference of approximately 5 to 7 microvolts in the response from the device. This amplitude difference was right in the range of the expected value for that particular device, which was approximately 15 microvolts. After replacing the Lock-in amplifier with a Network analyzer, a better looking response curve was observed. This response frequency spectrum from the Network analyzer is shown in Figure 53. This response also showed a noise level picked up by the output signal. This might be due to the fact that there was a noise level of charge carriers present in the device connected to the Network analyzer, and as the structure vibrated, it showed peaks at different modes of natural frequency of vibration. Once the output signal was normalized against the output without applying any voltage across the Wheatstone bridge, a clear peak appeared at the expected range of resonant frequency from the optical measurement.

Based on these results MEMS devices were designed and fabricated of the modified geometry, along with the triangular and regular rectangular shaped microcantilevers. Figure 54 and 55 show the SEM images of the MEMS device based on the triangular and the modified geometry, consecutively. Due to the problems faced during the fabrication processes lately, the devices did not work properly. Thus, the frequency response data for those devices are not added here. In the future, these devices need to be fabricated, characterized, and then tested for real time biological species detection.
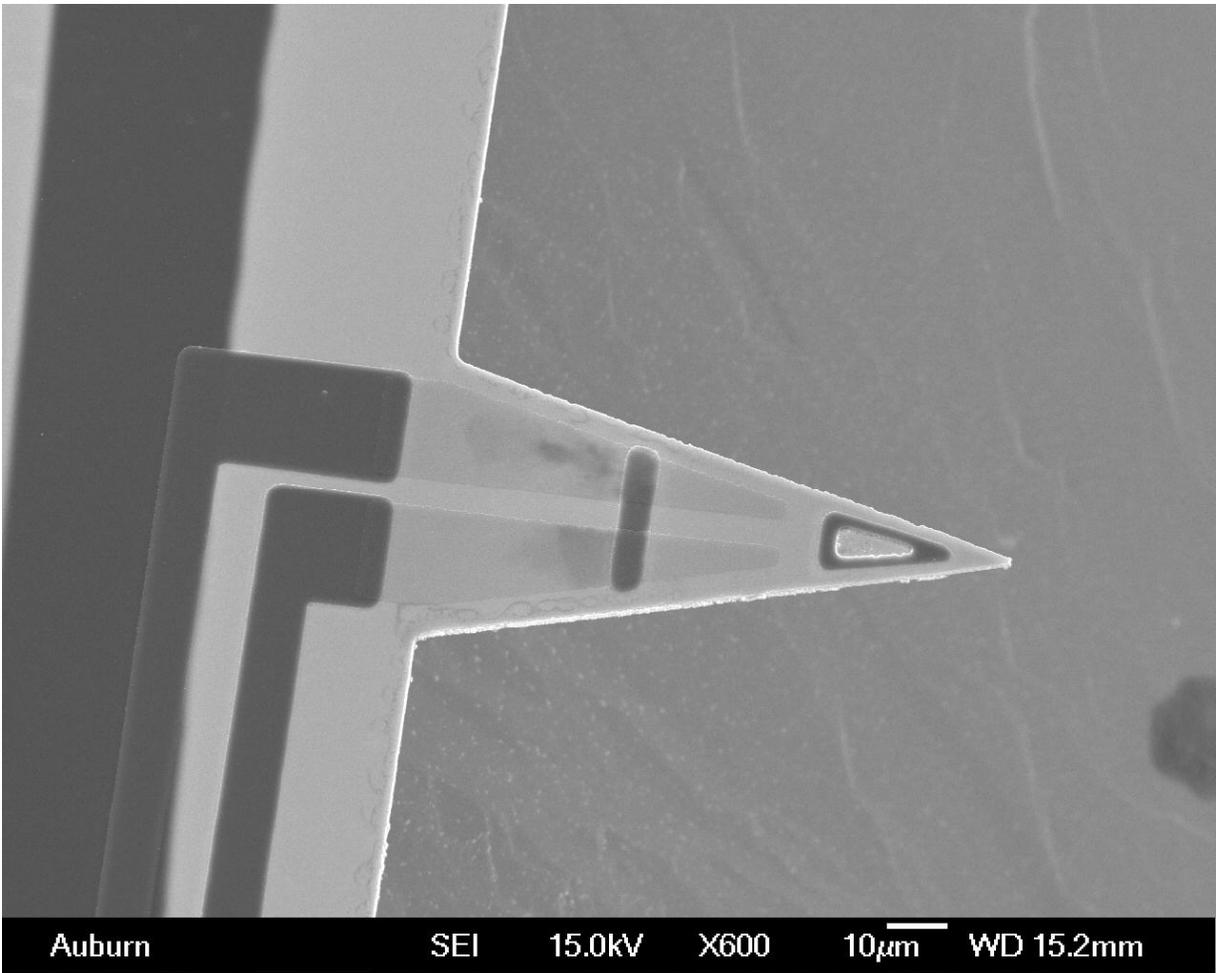
Figure 54: SEM image showing microcantilever MEMS device of triangular geometry.
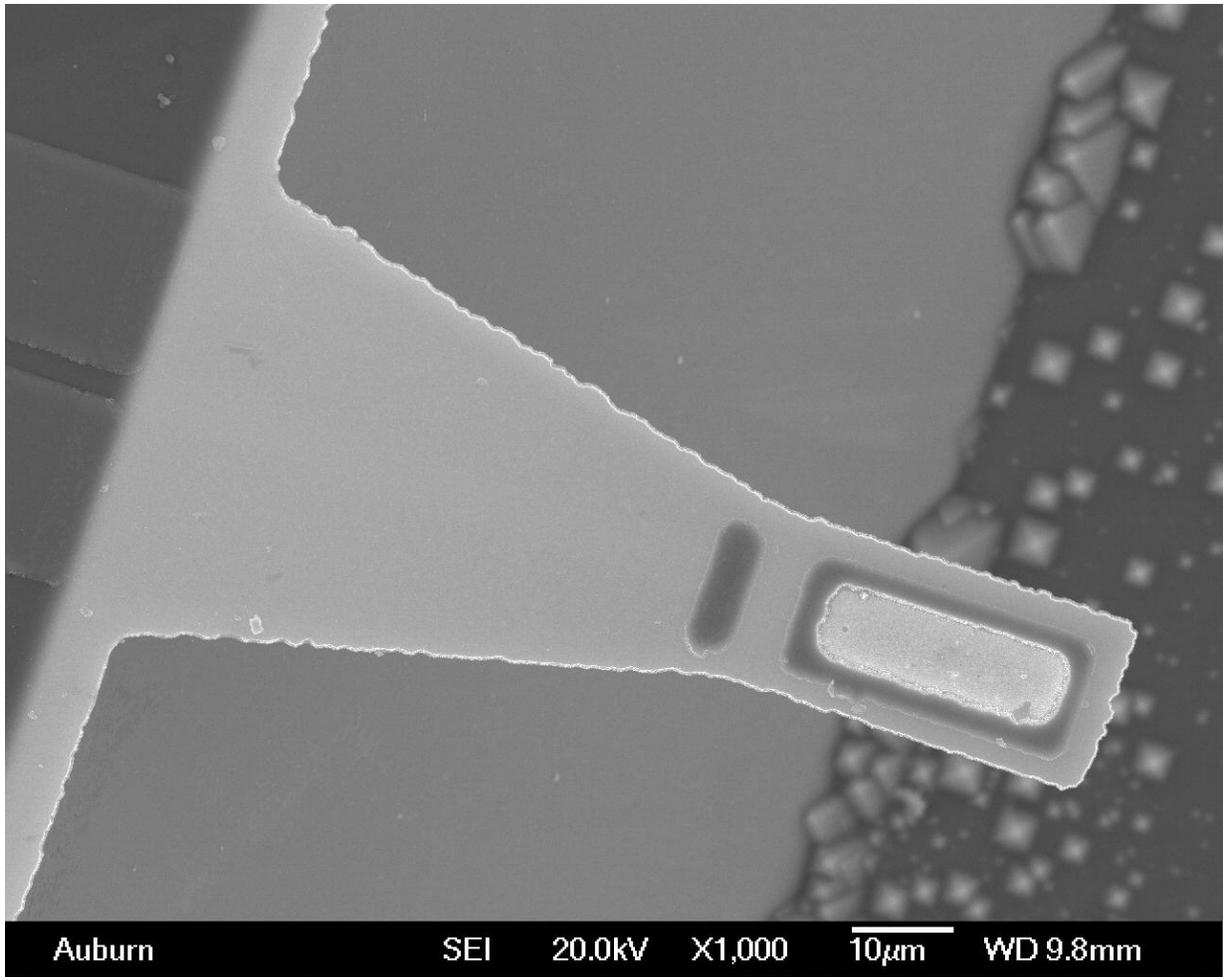
Figure 55: SEM image showing microcantilever MEMS device of the modified geometry.

References:

1.   Alvarez, M, Calle, A., Tamayo, J., Lechuga, L.M., Abad, A., Montoya, A.; Development of nanomechanical biosensors for detection of the pesticide DDT; Biosensors & Bioelectronics, Vol. 18, 2003.

2.   Baselt, D.R., Fruhberger, B., Klaassen, E., Cemalovic, S., Britton, C.L., Jr., Patel, S.V., Mlsna, T.E., McCorkle, D, Warmack, B.; Design and performance of a microcantilever-based hydrogen sensor; Sensors & Actuators B, Vol. 88, 2003.

3.   Gunter, R.L., Delinger, W.D., Porter, T.L., Stewart, R., Reed, J.; Hydration level monitoring using embedded piezoresistive microcantilever sensors; Medical Engineering & Physics, Vol. 27, 2005.

4.   Ji, H.-F.,Thundat, T; In-situ detection detection of calcium ions with chemically modified microcantilevers; Biosensors & Bioelectronics, Vol. 17, 2002.

5.   Pinnaduwage, L.A., Thundat, T., Hawk, J.E., Hedden, D.L., Britt, P.F., Houser, E.J., Stepnowski, S., McGill, R.A., Bubb, D.; Detection of 2,4-dinitrotoluene using microcantilever sensors; Sensors & Actuators B, Vol. 99, 2004.

6.   Porter, T.L., Eastman, M.P., Macomber, C., Delinger, W.G., Zhine, R.; An embedded polymer piezoresistive microcantilever sensor; Ultramicroscopy, Vol. 97, 2003.

7.   Zhou, J., Li, P., Zhang, S., Huang, Y., Yang, P., Bao, M., Ruan, G.; Self-excited piezoelectric microcantilever for gas detection; Microelectronics Engineering, Vol. 69, 2003.

8.   Tamayo, J., Humphris, A.D.L., Malloy, A.M., Miles, M.J.; Chemical sensors and biosensors in liquid environment based on microcantilevers with amplified quality factor; Ultramicroscopy, Vol. 86, 2001.

9.   Rodolphe, M., Jensenius, H., Thaysen, J., Christensen, C.B., Boisen, A.; Adsorption kinetics and mechanical properties of thiol-modified DNA-oligos on gold investigated by microcantilever sensors; Ultramicroscopy, Vol. 91, 2002.

10.   Baselt, D.R., Lee, G.U., Colton, R.J.; Biosensor based on force microscope technology; Journal of Vacuum Science & Technology B, Vol. 14, 1996.

11.   Raiteri, R., Grattarola, M., Butt, H.-J., Skaladal, P.; Micromechanical cantilever-based biosensors; Sensors & Actuators B, Vol. 79, 2001.

12.   Ilic, B. Czaplewski, D., Zalalutdinov, M., Craighead, H.G., Neuzil, P., Campagnolo, C., Batt, C.; Single cell detection with micromechanical oscillators; Journal of Vacuum Science & Technology B, Vol. 19, 2001.

13.   Gunter, R.L., Delinger, W.G., Manygoats, K., Kooser, A., Porter, T.L.; Viral detection using an embedded piezoresistive microcantilever sensor; Sensors & Actuators A, Vol. 107, 2003.

14.   Kooser, A., Manygoats, K.,Eastman, M.P., Porter, T.L; Investigation of the antigen antibody reaction between anti-bovine serum albumin (a-BSA) and bovine serum albumin (BSA) using piezoresistive microcantilever based sensors; Biosensors & Bioelectronics, Vol. 19, 2003.

15.   Yan, X., Ji, H.-F., Lvoy, Y.; Modification of microcantilevers using layer –by-layer nanoassembly film for glucose measurement; Chemical Physics Letters, Vol. 396, 2004.

16.   Ilic, B., Yang, Y., Craighead, H.G.; Virus detection using nanoelectromechanical devices; Applied Physics Letter, Vol. 85, 20004.

17.   Alvarez, M., Tamayo, J.; Optical sequential readout of microcantilever arrays for biological detection; Sensors & Actuators B, Vol. 106, 2005.

18. Datskos, P.G., Sauers, I., Detection of 2-mercaptoethanol using gold-coated micromachined cantilevers, Sensors and Actuators B, Vol. 61, 1999.

19. Oden, P.I., Gravimetric sensing of metallic deposits using an end-loaded microfabricated beam structure, Sensors and Actuators B, vol. 53, 1998.

20. Stern, R., Levy, M., Acoustic wave sensors, Academic Press, 1997.

21. Ilic, B, Craighead, H.G., Krylov, S., Senaratne, W., Ober, C., Neuzil, P., Attogram detection using nanoelectromechanical oscillators, Journal of Applied Physics, vol. 75, 2004.

22. Timoshenko, Stephen; Vibration problems in engineering; 2nd edition; D. Van Nostrand Co., Inc.; New York; July, 1937.

23. Blevins, R.D., Formulas for natural frequency and mode shape, Krieger Publishing Co., Malabar, Fl, 2001.

24. Yahiaoui, R., Bosseboeuf, A., Cantilever microbeams: modeling of the dynamical behaviour and material characterization, 5th International conference on Thermal and Mechanical Simulation and Experiments in Micro-electronics and Micro-Systems, Europe, 2004

25. Lochon, F., Dufour, I., Rebiere, D.; An alternative solution to improve sensitivity of resonant microcantilever chemical sensors: comparison between using high-order modes and reducing dimensions; Sensors and Actuators B; 2005.

26. Sone, H., Fujinuma, Y., Hieida, T., Chiyoma, T., Okano, H., Hosaka, S.; Picogram mass sensor using microcantilever; SICE Annual Conference in Sapporo; August 4-6, 2004; Japan.

27. Elwenspoek, M., Wiegerink, R.; Mechanical microsensors; Springer; Germany; 2001.

28. Harley, J.A., Kenny, T.W.; 1/F noise considerations for the design and process optimization of piezoresistive cantilevers; Journal of Microelectromechanical Systems, Vol. 9, No. 2; 2000.

29.   Nyquist, H.; Thermal agitation of electric charge in conductors; Physical Review, Vol. 32; 1928.

30.   DeSilva, Clarence W., Vibration: fundamentals and practice, CRC Press LLC, Boca Raton, Florida, 2000.

31.   ANSYS Release 8.0 Documentation.

32.   Kiesewetter, L., Zhang, J.-M., Houdeau, D., Steckenborn, A.; Determination of Young's moduli of micromechanical thin films using the resonant method; Sensors and Actuators A; 1992.

33.   Sader, J.E.; Frequency response of cantilever beams immersed in viscous fluids with applications to the atomic force microscope; Journal of Applied Physics, Vol. 84, 1998.

34.   Sandberg, R., Molhave, K., Boisen, A., Svendsen, W.; Effect of gold coating on the Q-factor of a resonant cantilever; Journal of Micromechanics & Microengineering, Vol. 15, 2005.

35.   Southworth, D.R., Craighead, H.G., Parpia, J.M.; Pressure dependent resonant frequency of micromechanical drumhead resonators; Applied Physics Letters, Vol. 94, 2009.

36.   Ikehara, T., Lu, J., Konno, M., Maeda, R., Mihara, T.; A high quality-factor silicon cantilever for a low detection-limit resonant mass sensor operated in air; Journal of Micromechanics & Microengineering, Vol. 17, 2007.

37.   Bianco, S., Cocuzza, M., Ferrero, S., Giuri, E., Piacenza, G., Pirri, C.F., Bich, D., Merialdo, A., Schina, P., Correale, R.; Silicon resonant microcantilevers for absolute pressure measurement; Journal of Vacuum Science & Technology B, Vol. 24, No. 4, 2006.

38.   Sandberg, R., Svendsen, W., Molhave, K., Boisen, A.; Temperature and pressure dependence of resonant in multi-layer microcantilevers; Journal of Micromechanics & Microengineering, Vol. 15, 2005

39.   Baginsky, T.; Microelectronics fabrication and design lab manual; Auburn University; 2002.

40.   Williams, K.R., Gupta, K., Wasilik, M.; Etch rates for micromachining processing-Part II; Journal of Microelectromechanical Systems; Vol. 12, No. 6; 2003.

41.   Kovacs, G.T.A., Maluf, N.I., Petersen, K.E.; Bulk micromachining of silicon; Proceedings of the IEE, Vol. 86, No. 8, 1998.

42.   Miller, Eric; Low stress silicon nitride process development, Washington Technology Center; 2001.

43.   Madou, M.; Fundamentals of microfabrication; CRC Press LLC; 1997.

44.   Mehta, N.J. Study of hydrogenated diamond like carbon films and investigating its use in MEMS devices, MS Thesis, Auburn University, 2005.

45.   Tabata, Osamu; pH controlled TMAH etchants for silicon micromachining; The 8th International Conference on Solid-State Sensors and Actuators, and Eurosensors IX; 1995.

46.   Tea, N.H., Milanovic, V., Zincke, C.A., Suehle, J.S., Gaitan, M., Zaghloul, M.E., Geist, J.; Hybrid postprocessing etching for CMOS-compatible MEMS; Journal of Microelectromechanical Systems, Vol. 6, No. 4; 1997.

47.   Kovacs, G.T.A., Maluf, N.I., Petersen, K.E.; Bulk micromachining of silicon; Proceedings of the IEEE, Vol. 86, No. 8, 1998.

48.   Zhang, J., Hon, W.C., Leung, L.L.W., Chen, K.J.; CMOS-compatible micromachining techniques for fabricating high-performance edge-suspended RF/microwave passive components on silicon substrates; Journal of Micromechanics and Microengineering, Vol. 15, 2005.

Appendix A

**Table A1: Simulation results for different geometrical shapes performed using ANSYS software**

| Shape ID	Shape Geometry	Shape Parameters	Frequency (Hz)	Frequency Shift (Hz)
1		$w = 10\mu$	192,997	125
2		$w = 20\mu$	194,124	53
3		$w = 30\mu$	194,858	46
4		$w_1 = 30\mu$ $w_2 = 10\mu$ $l_1 = 30\mu$	160,877	46
5		$w_1 = 20\mu$ $w_2 = 30\mu$	171,886	41
6		$w_1 = 20\mu$ $w_2 = 30\mu$ $w_3 = 10\mu$ $w_4 = 16\mu$ $l_1 = 30\mu$	118,461	31
7		$w_1 = 20\mu$ $w_2 = 30\mu$ $l_1 = 30\mu$ $l_2 = 20\mu$	162,002	36
8		$w_1 = 20\mu$ $w_2 = 30\mu$ $l_1 = 20\mu$ $l_2 = 30\mu$	161,451	34
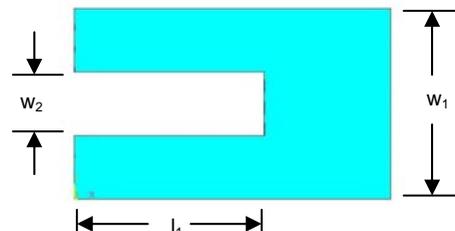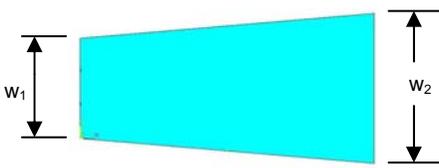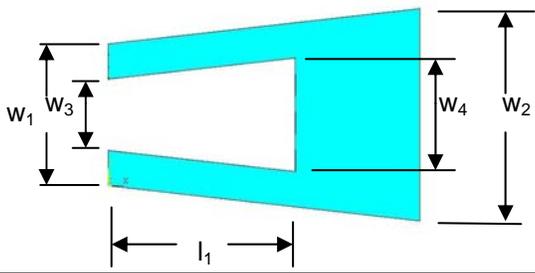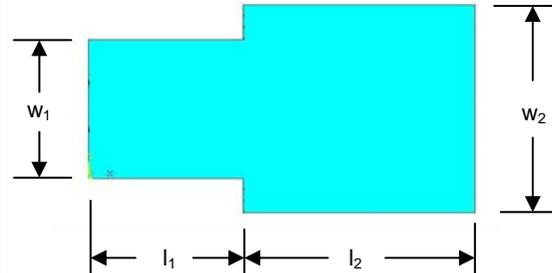
Shape ID	Shape Geometry	Shape Parameters	Frequency (Hz)	Frequency Shift (Hz)
9	Same as above	$w_1 = 10\mu$ $w_2 = 20\mu$ $l_1 = 30\mu$ $l_2 = 20\mu$	141,017	52
10		$w_1 = 10\mu$ $w_2 = 20\mu$ $l_1 = 20\mu$ $l_2 = 30\mu$	140,365	55
11		$w = 26.795\mu$ $\theta = 30^O$	390,010	462
12		$w = 41.421\mu$ $\theta = 45^O$	385,752	296
13		$w = 57.735\mu$ $\theta = 60^O$	379,027	211
14		$w = 100\mu$ $\theta = 90^O$	358,080	118
15		$w_1 = 26.795\mu$ $w_2 = 10\mu$ $\theta = 30^O$	361,458	436
16		$w_1 = 41.421\mu$ $w_2 = 10\mu$ $\theta = 45^O$	289,124	236
17		$w_1 = 41.421\mu$ $w_2 = 12\mu$ $\theta = 45^O$	314,751	252
18		$w_1 = 57.735\mu$ $w_2 = 10\mu$ $\theta = 60^O$	294,402	179
19		$w_1 = 57.735\mu$ $w_2 = 10\mu$ $\theta = 60^O$	320,591	185
20		$w_1 = 100\mu$ $w_2 = 10\mu$ $\theta = 90^O$	213,480	117
21		$w_1 = 100\mu$ $w_2 = 15\mu$ $\theta = 90^O$	251,421	93
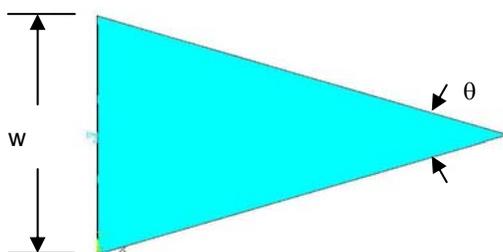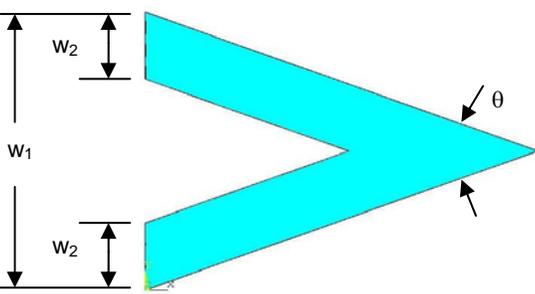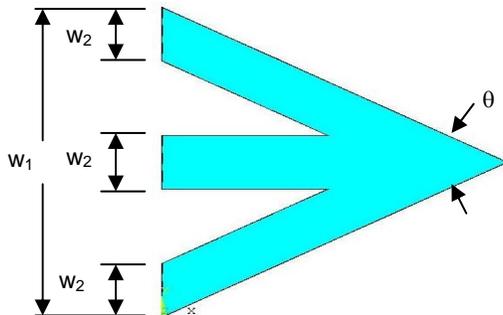
Shape ID	Shape Geometry	Shape Parameters	Frequency (Hz)	Frequency Shift (Hz)
22		$w_1 = 26.795\mu$ $w_2 = 10\mu$ $w_3 = 20\mu$ $\theta = 30^O$ $l_1 = 20\mu$	186,860	69
23		$w_1 = 41.421\mu$ $w_2 = 12\mu$ $w_3 = 20\mu$ $\theta = 45^O$ $l_1 = 20\mu$	200,140	78
24		$w_1 = 57.735\mu$ $w_2 = 12\mu$ $w_3 = 23.094\mu$ $\theta = 60^O$ $l_1 = 20\mu$	221,182	60
25		$w_1 = 100\mu$ $w_2 = 10\mu$ $w_3 = 30\mu$ $\theta = 90^O$ $l_1 = 15\mu$ $l_2 = 50\mu$	161,737	56
26		$w_1 = 100\mu$ $w_2 = 10\mu$ $w_3 = 30\mu$ $\theta = 90^O$ $l_1 = 20\mu$ $l_2 = 55\mu$	134,920	44

Shape ID	Shape Geometry	Shape Parameters	Frequency (Hz)	Frequency Shift (Hz)
27		$w_1 = 26.795\mu$ $w_2 = 20\mu$ $\theta = 30^O$	198,939	70
28		$w_1 = 41.421\mu$ $w_2 = 20\mu$ $\theta = 45^O$	240,018	79
29		$w_1 = 57.735\mu$ $w_2 = 23.094\mu$ $\theta = 60^O$	256,579	70
30		$w_1 = 100\mu$ $w_2 = 30\mu$ $\theta = 90^O$	272,354	51